Cryogenic Single and Array Coils for Magnetic Resonance Systems

Johansen, Daniel Højrup

Publication date:
2019

Document Version
Publisher's PDF, also known as Version of record

Cryogenic Single and Array Coils for Magnetic Resonance Systems

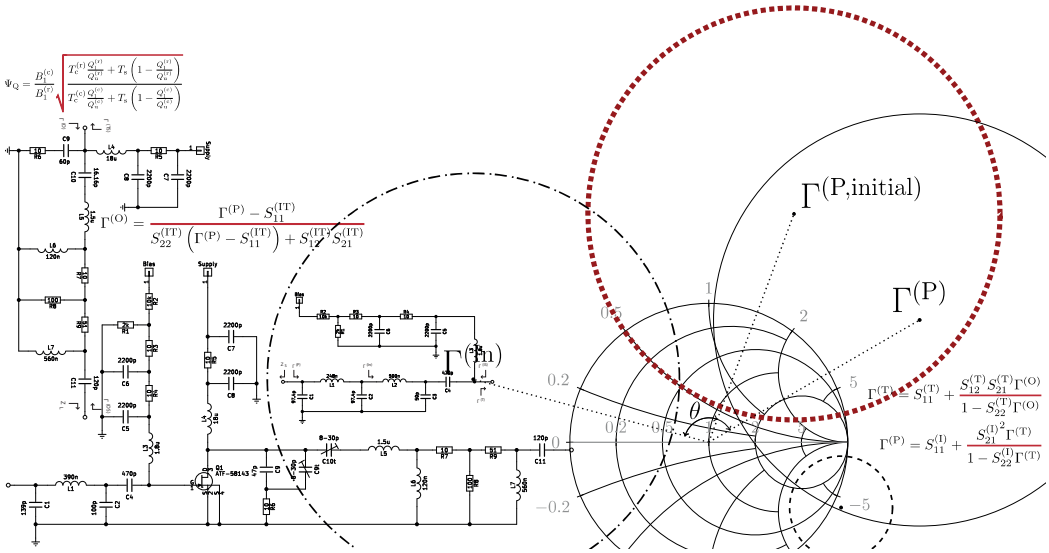

Daniel Højrup Johansen

PhD thesis

January 2019

DTU Electrical Engineering
Department of Electrical Engineering

The work presented in this thesis was carried out at the Department of Electrical Engineering in partial fulfillment of the requirements for the PhD degree at the Technical University of Denmark.

This work was supported in part by the Danish National Research Foundation under grant DNRF124.

Supervisors:

Vitaliy Zhurbenko, Associate Professor, PhD.
Department of Electrical Engineering, Technical University of Denmark.

Christoffer Laustsen, Associate Professor, PhD.
Department of Clinical Medicine, Aarhus University.

Jan Henrik Ardenkjær-Larsen, Professor, Center Leader, PhD.
Department of Health Technology, Technical University of Denmark.

Til Bedstemor
Du vil altid være i mit hjerte.

"Der er noget i luften
jeg véd ikke hvad,
som forår, skønt skoven
har mistet hvert blad,
der er noget i luften
som rosernes duften,
som fuglenes fryd,
skønt rosen er falmet, og fuglen
er draget mod syd."

Vilhelm Gregersen, 1911

Resumé

Kryogeniske Enkelt og Array Spoler til Magnetisk Resonans Systemer

Den samlede pris for kræft behandling i USA og EU overstiger årligt 100 milliarder Euro. Ved at benytte en kombination af magnetisk resonans billeddannelse (MRI) og opløselig dynamisk nuklear polarisation (dDNP) kan den årlige besparelse på medicin overstige mere end én milliard Euro. For at gøre teknikken brugbar i klinisk sammenhæng er et essentielt aspekt design og implementering af radiofrekvens (RF) modtager hardware, som er optimeret for maksimal signal-støj forhold (SNR). Denne afhandling undersøger tre primære emner indenfor hardware til MRI systemer som anvender dDNP af ^{13}C ved 3 T: Forforstærkere, volumen spoler og array spoler.

Forforstærkere til MRI arrays kræver en høj indgangsreflektionskoefficient, for at gøre det muligt at afkoble tilstødende spoler, samtidig med at opnå et lavt støjtal. I denne afhandling præsenteres en designprocedure, som muliggøre implementeringen af ideelle forforstærkere til MRI arrays ved at bruge tilbagekoblingen, som er naturligt tilstede i transistoren. Dette forårsager, at indgangsimpedansen af forforstærkeren afhænger af impedansen af udgangstilpasningskredsløbet, mens støjtallet forbliver konstant grundet, at transistoren har en høj forstærkning. En procedure til at designe kryogeniske forforstærkere bliver også præsenteret. Det vises teoretisk, at en negativ indgangsimpedans forforstærker kan bruges til at opnå ideel afkobling af spoler. I praksis opnås der en afkobling på 50 dB, hvilket gøres ved at benytte en kryogenisk forforstærker, der er kølet med flydende nitrogen til 77 K. Forforstærkeren udviser et støjtal på 0.05 dB med en indgangsimpedans på $-8 + j533\ \Omega$.

Kryogeniske volumen spoler er, generelt, ikke gode kandidater til humant brug grundet en høj belastning fra patienten, hvilket ikke kan nedsættes ved at køle spolen. Dette er ikke nødvendigvis tilfældet for volumen spoler, som benyttes til smådyr. Derfor undersøges følsomhedsforbedringen af en kryogenisk birdcage spole til smådyrsbrug også i dette arbejde. Den konstruerede birdcage spole har en rørdiameter på 50 mm med en længde på 100 mm og er kølet til 77 K ved at benytte flydende nitrogen. En dedikeret lavpris kryostat udvikles ligeledes. De målte ubelastede og belastede Q-faktorer af den kryogeniske birdcage spole er henholdsvis 627 og 616. Ved at benytte konventionelle formler for at udregne den potentielle SNR opnås 2.5 gange

forbedring ved sammenligning af en stuetemperatur og kryogenisk birdcage spole. Den konventionelle analyse tager dog ikke højde for påvirkningen af stuetemperatur RF frontenden. En udvidet analyse præsenteres derfor, som tager højde for temperaturen af både spolen og RF frontenden forbundet med spolen (hybridkobler, sende/modtage omskifter, forforstærker). Ved at tage højde for påvirkningen af stuetemperatur RF frontenden falder den forventede SNR forbedring til 2. Det er derfor vigtigt, når der benyttes en kryogenisk spole, også at benytte en kryogenisk RF frontende.

Styringen af de dedikerede sende/modtage omskifter og Q-ødelæggende kredsløb, brugt til både volumen og array spolerne, varetages af en PIN diode driver, som også beskrives i denne afhandling. PIN diode driveren skifter fra sende- til modtagetilstand på 0.4 μs og fra modtage- til sendetilstand på under 2 μs. Desuden reguleres strømmen til PIN dioden i modtagertilstanden så strømmen er uafhængig af forskellige PIN dioders knæspænding. I sendetilstanden påtrykkes en negativ spænding på -5 V.

For at opnå et større synsfelt og muliggøre accelereret/parallel billeddannelse benyttes et array af overflade spoler. I denne afhandling designes og implementeres en 32 kanals hjernespole til klinisk brug med fokus på at benytte parallel billeddannelse for at sænke skanningstiden. Ydelsen af hjernespolen måles i en MRI skanner og sammenlignes med en birdcage spole. Dette viser en forringelse af SNR på omkring 48 % i midten af et hovedfantom. Problemet er at forforstærkernes støj kobler mellem tilstødende spoler, når der benyttes ikke-overlappende elementer og konventionelle 50 Ω forforstærkere. Ved at ændre forforstærkerens optimale støj impedans til en kompleks impedans i stedet for de gængse 50 Ω, kan støjen i arrayet sænkes med omtrent 50 %. Hvis disse nye forforstærkere derfor benyttes i stedet, falder forringelsen til 19 %. Dette er dog kun i midten af fantomet, og tættere på overfladen udviser hjernespolen en signifikant bedre SNR. Derudover gør hjernespolen det muligt at benytte parallel billeddannelse, hvilket ikke er muligt med en birdcage spole. Specielt for array spoler gælder det, at forforstærkerens støjtal er en dårlig måleenhed. Dette skyldes, at den samlede støj i et array i større grad afhænger af forforstærkernes tilsvarende spændings- og strømstøj, og deres korrelation. Kort sagt muliggøre denne afhandling implementeringen af ideelle forforstærkere til både enkelt og array spoler ved både stue og kryogenisk temperatur.

Abstract

Cryogenic Single and Array Coils for Magnetic Resonance Systems

The annual cost of cancer treatment in the United States of America and the European Union exceed 100 billion euro. Using a combination of magnetic resonance imaging (MRI) and dissolution dynamic nuclear polarization (dDNP) the potential worldwide savings are in the billions of euro annually. To make the techniques clinically viable an essential aspect is the design and implementation of radio frequency (RF) receive hardware optimized for maximal signal-to-noise ratio (SNR). This work investigates three primary topics within receiver hardware for MRI systems utilizing dDNP of ^{13}C at 3 T: Preamplifiers, volume coils, and array coils.

Preamplifiers for MRI arrays require a high input reflection coefficient, to enable decoupling of neighbouring coils, while exhibiting low noise figure. In this thesis a design procedure is presented enabling the implementation of ideal preamplifiers for MRI arrays by using the inherent feedback of the transistor. This causes the input impedance of the preamplifier to depend on the output matching circuit while the noise figure remains constant due to the high gain of the transistor. A procedure for designing cryogenic preamplifiers is presented. It is shown theoretically that a negative input impedance amplifier can be used for ideal coil decoupling. In practice, 50 dB decoupling was achieved using a cryogenic preamplifier design cooled with liquid nitrogen to 77 K with a 0.05 dB noise figure having an input impedance of $-8 + j533\ \Omega$.

Cryogenic volume coils are generally not viable candidates for human imaging due to high sample loading, which cannot be mitigated by cooling the coil. This is not necessarily the case for volume coils for small animals. Hence, sensitivity improvement of a birdcage coil for small animal imaging using cryogenic cooling is investigated. The implemented birdcage coil has a bore size of 50 mm with a length of 100 mm and is cooled to 77 K using liquid nitrogen. A dedicated, low cost, cryostat was also developed. The measured unloaded and loaded Q-factors of the cryogenic birdcage are 627 and 616, respectively. Using conventional formulas for estimating the SNR gain between the room temperature and the cryogenic birdcage coil results in an estimated SNR gain of approximately 2.5 times. However, the conventional analysis does not

take into account the room temperature RF front end. An extended analysis is thus presented that takes into account the temperatures of the coil and the RF front end connected to the coil (hybrid coupler, transmit/receive switch, preamplifier). Thus, taking into account the influence of the room temperature RF front end, the expected SNR gain is 2 times. If instead a cryogenic RF front end is used the expected SNR gain is 2.4 times. Hence, it is vital when using cryogenic coils to also use a cryogenic RF front end.

Controlling the dedicated transmit/receive switch and Q-spoiling circuits used for both the volume and array coils is achieved by a custom PIN diode driver, which is also detailed in this work. The PIN diode driver switches from the transmit to receive state in approximately 0.4 μs and from receive to transmit in under 2 μs. Further, the PIN diode driver supplies a constant current, regardless of characteristics of the PIN diode(s), in the receive state. While in the transmit state a negative voltage of -5 V is applied.

To enable larger field-of-views and accelerated/parallel imaging an array of loop coils is employed. In this thesis, a 32 channel human brain coil is designed and implemented for clinical imaging focussing on the application of parallel imaging to decrease acquisition time of images. The performance is measured in the scanner versus a birdcage coil and shows an approximate SNR decrease in the center of a head phantom by approximately 48 %. The problem is noise coupling when using non-overlapped neighbouring elements and conventional 50 Ω noise figure optimized preamplifiers. By noise matching to a complex impedance, rather than the conventional 50 Ω, the noise coupled between non-overlapped coils can be decreased by approximately 50 %. Hence, using the newly proposed preamplifier design yields an SNR impairment of 19 %. This is, however, in the center of the phantom and closer to the surface a significant SNR increase is present. Further, the array coil enables parallel imaging, which is impossible with the birdcage coil. Especially for arrays, the SNR impairment caused by the preamplifiers due to noise coupling is not dominated by the noise figure, but rather the corresponding noise and current voltages and their correlation. Looking into the future, this work enables optimal preamplifiers for single and array coils for both room temperature and cryogenic operation.

Preface

The thesis in front of you was written as the conclusion of a PhD project undertaken at the Technical University of Denmark in the period from February 2016 to January 2019. Besides working at the Department of Electrical Engineering, I was also fortunate to spend four months at RAPID Biomedical in Germany developing the 32 channel brain coil, presented in a later chapter. Having worked with cellular and Internet-of-Things devices previously, it has been a revelation to engage this PhD study within a composite field of electrical engineering and healthcare technology. It has allowed me to, once again, see beyond a veil of greed, and rediscover the beauty of electronics made with wealth in mind - not just profit.

I can't help but wonder that, not in a hundred billion galaxies will you find another human being and of the billions of humans walking the crust of this planet, by some fluke of reality, we found each other - the closest of friends, dearest of family, brightest of colleagues, and kindest of souls. For this, I am eternally humble and grateful.

The path was at times smooth and comfortable, at times rough and steep. Now, as I stand at yet another crossroad, overlooking the well-trodden valleys and pinnacles of what has been, I ask myself "was is worth it?" Alas, as I scout the rugged unknown terrain of what is to come, a tremble ripples down my spine and beckons "where is the next summit?"

Daniel Højrup Johansen

List of Publications

During the course of the PhD study, a number of articles has been authored and co-authored. Three published journal articles (Paper A, B, and C) and four published conference papers (Paper D, E, F, and G) are first authored. Also, a fifth conference article has been accepted for publication (Paper H). The following papers are included as part of the thesis:

Journal papers:

Paper A: D. H. Johansen, J. D. Sanchez-Heredia, V. Zhurbenko, and J. H. Ardenkjær-Larsen, "Association and Dissociation of Optimal Noise and Input Impedance for Low-Noise Amplifiers," in *IEEE Transactions on Microwave Theory and Techniques*, vol. 66, no. 12, pp. 5290-5299, Dec. 2018.

Paper B: D. H. Johansen, J. D. Sanchez-Heredia, J. R. Petersen, T. K. Johansen, V. Zhurbenko, and J. H. Ardenkjær-Larsen, "Cryogenic Preamplifiers for Magnetic Resonance Imaging," in *IEEE Transactions on Biomedical Circuits and Systems*, vol. 12, no. 1, pp. 202-210, Feb. 2018.

Paper C: D. H. Johansen, M. M. Albannay, J. R. Petersen, V. Zhurbenko, and J. H. Ardenkjær-Larsen, "PIN Diode Driver for NMR and MRI," in *Journal of Magnetic Resonance*, vol. 300, pp. 114-119, Mar. 2019.

Conference papers:

Paper D: D. H. Johansen, J. D. Sanchez-Heredia, V. Zhurbenko, and J. H. Ardenkjær-Larsen, "Towards new vistas in preamplifier design for MRI," in *European Microwave Conference (EuMC) / European Microwave Integrated Circuits Conference (EuMIC)*, pp. 1159-1162 / 419-422, 2017.

Paper E: D. H. Johansen, J. D. Sanches-Heredia, V. Zhurbenko, and J. H. Ardenkjær-Larsen, "Practical Aspects of Preamplifier Designs for ^{13}C Imaging," in *Proceedings of the International Society of Magnetic Resonance in Medicine (ISMRM)*, no. 4299, 2017.

Paper F: D. H. Johansen, J. D. Sanches-Heredia, V. Zhurbenko, and J. H. Ardenkjær-Larsen, "Ideal Coil Decoupling in Receive Arrays using Negative Resistance Preamplifiers," in *Proceedings of the International Society of Magnetic Resonance in Medicine (ISMRM)*, no. 1711, 2018.

Paper G: D. H. Johansen, J. D. Sanches-Heredia, V. Zhurbenko, and J. H. Ardenkjær-Larsen, "Accurate Noise Figure Measurements for Highly Mismatched Preamplifiers," in *Proceedings of the International Society of Magnetic Resonance in Medicine (ISMRM)*, no. 1692, 2018.

Paper H: D. H. Johansen, J. D. Sanches-Heredia, V. Zhurbenko, and J. H. Ardenkjær-Larsen, "On the SNR of Cryogenic Receive Coils when using Room Temperature Preamplifiers," accepted for *Proceedings of the International Society of Magnetic Resonance in Medicine (ISMRM)*, 2019.

Other published and accepted contributions, which have been co-authored during the PhD study, but are otherwise not included as part of the thesis, are listed below:

Paper T: J. D. Sánchez-Heredia, D. H. Johansen, R. B. Hansen, E. S. S. Hansen, C. Laustsen, V. Zhurbenko, and J. H. Ardenkjær-Larsen, "Improved Decoupling for Low Frequency MRI Arrays using Non-conventional Preamplifier Impedance," in *IEEE Transactions on Biomedical Engineering* (early access).

Paper U: J. D. Sánchez-Heredia, D. H. Johansen, R. B. Hansen, E. S. S. Hansen, C. Laustsen, V. Zhurbenko, and J. H. Ardenkjær-Larsen, "Improved Decoupling for ^{13}C Coil Arrays Using Non-Conventional Matching and Preamplifier Impedance," in *Proceedings of the International Society of Magnetic Resonance in Medicine (ISMRM)*, no. 2711, 2017.

Paper V: J. D. Sánchez-Heredia, D. H. Johansen, R. A. Baron, M. Schneider, G. Spörl, J. Wosik, V. Zhurbenko, and J. H. Ardenkjær-Larsen, "3-Fold SNR Enhancement of Small Animal ^{13}C MRI using a Cryogenically Cooled (88 K) RF Coil," in *Proceedings of the International Society of Magnetic Resonance in Medicine (ISMRM)*, no. 1744, 2018.

Paper W: M. M. Albannay, D. H. Johansen, J. M. Vinther, V. Zhurbenko, and J. H. Ardenkjær-Larsen, "Low cost, compact, two-channel NMR spectrometer for CP-DNP," in *EUROMAR*, 2017.

Paper X: J. D. Sánchez-Heredia, R. B. Hansen, R. Baron, E. S. S. Hansen, D. H. Johansen, V. Zhurbenko, C. Laustsen, L. G. Hanson and J. H. Ardenkjær-Larsen, "Calibrated Coil Combination for Fixed-Geometry, Low-Frequency Coils with Application to Hyperpolarized 13C Measurements," accepted for the *Proceedings of the International Society of Magnetic Resonance in Medicine (ISMRM)*, 2019.

Paper Y: J. D. Sánchez-Heredia, R. Baron, E. S. S. Hansen, D. H. Johansen, V. Zhurbenko, C. Laustsen, and J. H. Ardenkjær-Larsen, "A Robust Cryogenic RF Coil (88K) for In-vivo Hyperpolarized 13C MRI of Rats," accepted for the *Proceedings of the International Society of Magnetic Resonance in Medicine (ISMRM)*, 2019.

Paper Z: R. Baron, J. D. Sánchez-Heredia, D. H. Johansen, V. Zhurbenko, and J. H. Ardenkjær-Larsen, "High-Q, tunable High Temperature Superconducting receiver coil for 13C applications," accepted for the *Proceedings of the International Society of Magnetic Resonance in Medicine (ISMRM)*, 2019.

Contents

Part I

Preliminaries

1 Introduction

Imagine sitting in a hospital. You have talked with various doctors, had your blood drawn, and been through countless weird, noisy, strange machines. Sitting in yet another waiting room, the smell is the same in all hospitals - a feint clinical odour of hand rubbing alcohol. Suddenly the doctor pushes the double swinging doors open. Eye contact is elusive, her face looks sturdy, almost stoic. Diagnosis: *Cancer*. The thoughts race relentlessly through your head: What about my family? The house? The dog? Me? The doctor is talking, but the words are a blur. Fragments are only caught. Something about 12 weeks of radiation therapy and chemotherapy. What about my hair? And then, another MRI scan, what ever that is? The machine with the hearing protection and some faint **clicks** and **clacks** where I fell asleep? If the tumor has not decreased in size, another round of chemotherapy. Wait for 12 weeks again... Rinse and repeat...

It is estimated that, worldwide, 8.2 million died from cancer in 2012 [1] and it is identified as the second highest cost of any medical condition in the United States (US). In the US, the cost of cancer treatment is estimated to rise beyond $173 billion in 2020 [2]. In the European Union (EU) the total cost of cancer treatment in 2014 was assessed at € 83.1 billion [3]. The cumulative 1 year cost of cancer drug treatment varies greatly from around $60,000 [4] to potentially over $500,000 [5] with an average cost of approximately $90,000. This is just for the drugs and thus excludes other expenses such as radiation therapy and general hospital costs. Siegel et al. [6] estimates approximately 1.6 million new cases of cancer in 2017. Assuming that 10 % of new cancer cases need drug therapy, this amounts to an approximate total of $14.4 billion. The example given in the beginning of this introduction is a common procedure when cancer has been diagnosed [7]. It is an iterative approach to find the correct medicine which the cancer responds to. The problem is three fold. One aspect is the stress it puts on the patient and their loved ones. The second aspect is the fact that the cancer may spread during the process of determining the correct medicine. The third aspect is the monetary cost of choosing an incorrect drug having to reiterate. This work focuses on the combination of conventional anatomic magnetic resonance imaging (MRI) and magnetic resonance (MR) spectroscopic imaging using a hyperpolarized ^{13}C contrast agent. The method is called hyperpolarized magnetic resonance (HMR) and promises a signal-to-noise ratio (SNR) increase by more than 10,000 [8]. ^{13}C contrast agents are showing exceptional prospects in determining the efficacy of

cancer treatment and is a step towards personalized medicine [9, 10]. Hence, instead of waiting 12 weeks to evaluate the physical size of the tumor the effect of the drugs can be seen almost instantaneously on the metabolism inside the tumor. Thus, efficacy of the treatment is evaluated in minutes rather than days [11]. If the method of HMR can cut the drug cost of cancer treatment by just 10 % it amounts to a saving of $1.44 billion per year - just in the US. Hence, the method of HRM has a worldwide savings potential in the billions of euro.

HMR using ^{13}C labelled contrast agents show remarkable applicability in other areas than cancer as well. The basic concept of HMR is that the ^{13}C contrast agent is an integral part of the Krebs cycle and thus the metabolism of the contrast agent can be traced through the Krebs cycle using MR [10]. HMR is, besides cancer, also excellent for cardiology [12–14] and neurology [9, 15, 16]. In cardiology, animal models have shown the potential of investigating hypertension and cardiac diseases. In neurology, the ^{13}C contrast agents are showing great potential in investigating the blood-brain-barrier to look at neurodegenerative disease, traumatic brain injury, and stroke [9]. Hence, HMR can be used for basically any disease or injury which metabolizes the specific contrast agent.

1.1 The MR and dDNP Techniques in Brief

A brief, general, description of the technique of magnetic resonance is sufficient for the purpose of this work. MR is a phenomenon that affects magnetic nuclei, hence nuclei with an uneven atomic weight. When magnetic nuclei are placed in a strong static magnetic field (B_0) they start to precess at a frequency called the Larmor frequency. If another time varying magnetic field (B_1) is applied perpendicular to the B_0 field at the Larmor frequency the precessing nuclei are excited away from equilibrium. When the B_1 field is switched off, the nuclei precess back towards equilibrium, which can be measured by Faraday induction giving rise to a free induction decay (FID). The Larmor frequency is described by the product between the gyromagnetic ratio of the observed nuclei and the B_0 field. Unless otherwise noted, the nuclei used in this work is ^{13}C with $B_0 = 3$ T resulting in a Larmor frequency of 32.1 MHz. For imaging, another set of magnetic fields called gradients are utilized. The gradient fields perturb the B_0 field such that the Larmor frequency and phase of the nuclei slightly change. This makes it possible to perform spatial localization by the use of the k-space. [17, 18]

Now, the concept of HMR principally requires quantum mechanics to understand. The technique behind HMR is called dissolution dynamic nuclear polarization (dDNP).

Several excellent resources are available detailing the principles of dDNP [8, 9, 19, 20] and only a brief introduction is given here. The basic concept of HMR is that some appropriate substance is cooled to cryogenic temperatures, polarized by irradiating the sample with microwaves, and dissolved, usually by an injection of hot water. The solution is then transferred to a quality assurance (QA) module and subsequently to the patient in the MRI machine. There are many contrast agents available in the general case of DNP for NMR [21, 22]. The sample requirements are three-fold. 1) It is imperative that a free electron is present. The free electron is usually added by an organic free radical which can easily be filtered after polarization. Trityl is the prevalent substance used in a clinical setting. 2) When the sample is in solid state it must be amorphous. If the sample is not amorphous high concentration areas of radical arises which impairs the polarization process. To prevent crystallization e.g. glycerol or glycol is added. 3) The agent must be biomedically safe. Both in terms of toxicity but also metabolization. Pyruvate metabolizes primarily into lactate and is currently viewed as a very safe contrast agent. When the sample is placed in a strong static magnetic field the electron spin is easily magnetized as compared to the proton spin due to the high gyromagnetic ratio of the electron. By irradiating the sample with microwaves, at the Larmor frequency of the electrons, the electron polarization in part is transferred to the protons. The polarization transfer happens on an hour-timescale. When the sample has been polarized it is dissolved such that it can be injected. To dissolve the sample, hot water is simply injected into the frozen sample. During polarization the sample is cooled to approximately 1-2 K. During dissolution the sample is raised above the cryogenics and the hot water is injected. However, the sample is still in the high magnetic field in order to maintain the polarization. After the dissolution the sample is filtered and transferred to the QA module and subsequently injected into the patient.

1.2 Scope and Objectives

HMR is a multidisciplinary field within chemistry, biology, physics, medicine, and electrical engineering. This work engages primarily the electrical engineering aspects. The fundamental question addressed, as a basis of a curiosity driven research approach, is:

What is the ultimate limit of detection in hyperpolarization?

The end-game is the design and implementation of cryogenic receive coils for ^{13}C HMR. Cryogenic single coils promise SNR increases of up to 15 times [23]. Hence, the

base line SNR gain in conjunction with hyperpolarization is potentially raised from 10,000 to 150,000 times. This is an astounding, potential, baseline SNR increase. However, there is many problems in coil design, both theoretical and practical, that needs to be solved in order to deliver on the promise of 150,000 times baseline increase in SNR using hyperpolarization and cryogenic array coils.

To reach the ultimate limit of detection, from a hardware point of view, the primary focus is placed on receive coil design. Within the topic of receive coils three distinct research objectives are defined:

O1: Investigate the optimality principles of preamplifiers for single and array coils.
The understanding of preamplifiers are vital for cryogenic coils because their transistor(s) generate noise. Furthermore, in array coils, the preamplifier is essential for decoupling of the elements ensuring good parallel imaging performance. Hence, optimality principles of designing preamplifiers for both single and array coils in terms of both decoupling and noise is paramount.

O2: Assess the feasibility of using cryogenic volume coils for HMR.
By far the largest focus of cryogenic coils are on small surface coils. The concept of cryogenic volume coils have thus far not received much attention. Hence, this objective aims at determining the feasibility of using cryogenic volume coils.

O3: Design and implementation of array coils for clinical HMR.
Translation of HMR into clinical practise is essential and requires the design and implementation of array coils designed to be compliant with clinical requirements.

The following section reviews the current state-of-the-art in relation to the three research objectives.

1.3 State-of-the-Art

Within the topic of preamplifier design for MRI, only a few papers have investigated the design of highly mismatched preamplifiers for array coils [24–28] and within cryogenic preamplifiers for MRI even fewer papers has been published [29, 30]. In brief, if the contributions of this thesis is excluded, the design methods for array preamplifiers involve using a high impedance field effect transistor (FET) and determining an acceptable trade-off between the noise performance and the input impedance by designing the input matching circuit of the transistor. Concerning cryogenic preamplifiers

the available literature is mostly for NMR spectrometers [31–34]. Hence, investigating the optimality principles of preamplifiers for single and array coils, for both room temperature and cryogenic operation, is essential in understanding the ultimate limit of detection. In depth literature studies of preamplifier design methodologies and cryogenic preamplifiers are found in Papers A and B, respectively.

In terms of cryogenic receive coils for MRI, the prevalent topologies are variations of the loop coil. This is because when the size of the loop coil is decreased a higher SNR entails due to higher B_1 field of the coil and lower noise due to the coil being coupled to less of the sample. Hence, as the size of a loop coil decreases the sample loading also decrease resulting in a coil noise dominated system where the majority of the noise comes from the coil. To decrease the noise of the coil it is then cooled. Some papers focus on cryogenic copper coils [35–37], however, the high temperature superconductor (HTS) technology yields higher SNR [38–41]. Ginefri et al. [42] presents a detailed review concerning HTS coils for MRI and Ma et al. [43] presents a review of low main field strength superconducting coils. Using HTS the conventional loop is still relevant [30, 44–46]. However, because of the very high inherent Q-factor of the coil, variations of the loop coil can yield better SNR. The increased SNR is because the matching circuit when using a conventional loop may significantly impair the SNR. Variations of the loop coil are e.g. single sided spiral with interdigitated capacitive elements [42, 47] (resembling the layout of a surface acoustic wave, SAW, filter) or a double-sided single-turn transmission line resonator [42, 48] (resembling the split-ring-resonator unit cell used for metamaterials). In [23] a cryogenic coil system is presented exhibiting an SNR increase of 15 times than that of a room temperature coil. The concept of the Josephson junction can also be applied to implement a superconducting quantum interference device (SQUID), which theoretically provides better SNR when comparing against conventional coil designs using either copper or HTS [49]. SQUIDs are, however, mostly used for low frequency applications [50]. The major challenge for cryogenic coils is to extend the FOV beyond that of a single surface coil. One approach is to implement cryogenic volume coils, which has been done for NMR spectrometers for many years. Another approach is to use arrays of surface coils, where very few papers exist describing cryogenic arrays [48, 51].

Since Roemer et al. [52] described the concepts of array coils for MRI they have become a standard tool for clinical usage. Hence, concerning room temperature array coils, a cornucopia of papers exist. The basis is that the ultimate SNR is rapidly approached using approximately 12 elements [53–56]. As the element count increases further the ability of the array to perform parallel imaging and thus decrease imaging time is increased while the ultimate SNR remains constant. Hence, increasing the

element count is vital to decrease imaging time, while maintaining proper sample loading and noise coupling between elements [57–59]. Keil and Wald [60] presents what is likely the most comprehensive design guide for MRI arrays available and also includes a thorough review of array coils for MRI. The element count of modern arrays are typically in the range from 8 to 64 channels [61–65], which are based on traditional overlapping of nearest neighbour elements and preamplifier decoupling. For parallel imaging, a range of different topologies are published such as butterfly coils [66, 67], circular symmetric [68], double spirals [69], orthogonal loops [70], and non-overlapped elements [71, 72]. All these topologies aim to increase the performance of parallel imaging while maintaining the SNR at a proper level. Most of the published array coils are for ^{1}H imaging. While companies, such as RAPID Biomedical, design custom coils, there are few published array coils for ^{13}C imaging. Especially for whole brain ^{13}C imaging a void in literature is apparent where the maximum published channel count of an array is at 32 channels and is made by Massachusetts General Hospital for the University of California, San Francisco (UCSF) and utilizes the conventional overlapping of nearest neighbours combined with preamplifier decoupling [73, 74].

Having defined the state-of-the-art, the following section details the contributions of the thesis both in terms of the chapters of the thesis and included papers.

1.4 Contributions and Organization

The thesis is compiled as a collection of articles with traditional chapters supplementing the included papers. The chapters are organized in the former part of the thesis (Preliminaries), which complements the published and submitted papers included in the latter part of the thesis (Papers). The chapters aims to describe both fundamental aspects and further developments of the papers included in the latter part of the thesis. To quantify the contributions of the thesis, five topics are identified: Preamplifiers, single coils, array coils, auxiliary devices, and cryogenics. An overview of the contributions of the papers and chapters is found in Table 1.1.

The topic concerning preamplifiers cover primarily O1 in which focus is on the theory, design, and implementation of ideal/perfect preamplifiers. This topic is also the most investigated in which Paper A, B, D, E, F, G and H, and Chapter 2 is focussed. The topic of single coils, pertaining to O2, is investigated primarily in Paper H and Chapter 3 with peripheral focus by Papers A, B, and C. Array coils, especially in the context of preamplifiers, are investigated by Papers A, D, E, and F, and Chapter 4. Auxiliary devices covers aspects such as transmit/receive (T/R) switches, hybrid couplers, power supplies, and positive-intrinsic-negative (PIN) diode

Table 1.1: Contributions of the thesis.

		Preamplifier	**Single coils**	**Array coils**	**Auxiliary devices**	**Cryogenics**
Journals	Paper A	●	○	●		
	Paper B	●	○		○	●
	Paper C		○	○	●	
Conferences	Paper D	●		●		
	Paper E	●		●		
	Paper F	●		●		
	Paper G	●				
	Paper H	●	●		○	●
Thesis	Chapter 2	●				●
	Chapter 3		●		○	●
	Chapter 4	○		●		○

drivers. The primary investigation is by Paper C. However, periphery focus is also present in Paper B and Chapter 3. Finally, concerning cryogenics, Paper B and H, and Chapter 3 has a key focus, with Chapter 4 touching upon the topic. The organization of the thesis is described below, including a brief summery of the following chapters and papers.

Chapter 2: This chapter is aimed at describing some further developments of the preamplifiers, which are not included in the papers. Hence, this chapter is related to O1. Included in this chapter is the specification of the requirements for the preamplifiers needed in MRI and a review of fundamental theory such as gain, noise, and input impedance. The design of three preamplifiers, optimized for either single coil, array coil, or cryogenic operation is presented.

Chapter 3: The investigation of a novel cryogenic birdcage and a so-called paranoide coil is of primary focus in this chapter and thus pertains to O2. A review and extension of the theory of relative and comparative SNR is included. Also, design of a room temperature and cryogenic birdcage coil, including cryostat, T/R switch, and hybrid coupler is described. Finally, a novel volume coil, called a paranoide, is presented.

Chapter 4: A 32 channel array coil for ^{13}C brain imaging is presented in this chapter. It is designed to comply with clinical standards and should thus be possible to implement in the clinic. Hence, this chapter is primarily linked with O3. The chapter includes the design and characterization of the 32 channel brain coil and an analysis of the coupling of the noise generated by the preamplifiers in an array. Thus, another

design approach for preamplifiers for arrays is investigated (O1) showing a potential SNR increase of approximately 40 % in comparison with conventional preamplifiers.

Chapter 5: The final chapter discusses aspects of cryogenic coils for MRI and an outlook on possible further developments is presented.

Paper A: A novel preamplifier design approach is presented in this paper. The presented design approach enables the design of optimal noise figure preamplifiers while the input reflection coefficient is unity (or slightly higher for optimal preamplifier decoupling). This paper is thus highly linked with O1.

Paper B: A cryogenic preamplifier is designed and implemented, including a review of semiconductor physics for low-frequency electronics. Also, auxiliary devices are explained which is required for optimal cryogenic performance. This paper is aimed at O1.

Paper C: This paper describes a PIN diode driver for MRI and NMR systems. This PIN diode driver is used for controlling the T/R switch of the cryogenic birdcage in Chapter 3.

Paper D: If the optimal noise match of a preamplifier is not 50 Ω, matching the coil to another impedance yields a constant noise figure, while the preamplifier decoupling is optimized. This paper thus pertains to O1.

Paper E: The first iteration of preamplifiers for array coils which shows a low noise figure with an inductive input impedance. This paper was the basis from which Papers A, D, and F where developed.

Paper F: This paper describes the optimal impedance of the preamplifier required for optimal decoupling and shows that it can be implemented in practise by using the design procedure presented in Paper A.

Paper G: Characterizing the preamplifiers can be particularly tedious because of their low noise figure and high mismatch. This paper discusses the consequences of highly mismatched and low noise figure preamplifiers in terms of measurement uncertainties when using a standard 50 Ω measurement system.

Paper H: If it is assumed that the SNR impairment of the preamplifier is constant when comparing a room temperature and cryogenic coil the resulting comparative SNR is overestimated. This paper derives the correction factor required for accurate comparative SNR predictions when the coil and RF front end is at different temperatures.

Preamplifiers 2

The use of preamplifiers* are paramount in any application involving reception of small signals and HMR is no exception. However, as will be investigated in this chapter, the requirements for an HMR preamplifier diverges substantially from a conventional RF LNA for wireless communication systems.

In the early 19th century a flurry of research in especially physics and mathematics resulted in a deeper understanding of the concepts of noise. First with Einstein's paper in Brownian noise [75], later with the birth of modern stochastic processes [76–78]. A pivotal work by Harald Friis in 1944 described the noise of cascaded devices as, [79]

$$F = F^{(1)} + \frac{F^{(2)} - 1}{G_{\mathrm{Av}}^{(1)}} + \frac{F^{(3)} - 1}{G_{\mathrm{Av}}^{(1)} G_{\mathrm{Av}}^{(2)}}, \tag{2.1}$$

where $F^{\dagger}$ is the noise figure and G_{Av} is the available gain. Superscripted integers indicate the stages in the system. Hence, the noise figure degradation caused by the second and third stage in an RF system is mitigated by the gain of the first stage. Equation (2.1) cemented the need for high gain and low noise preamplifiers to mitigate the high noise of e.g. the mixers of the time. In the latter half of the 19th century a myriad of preamplifiers design techniques and implementations have been published. As stated earlier, the requirements for MRI preamplifiers diverge from conventional wireless communication preamplifiers. From a gain perspective it has been found in practise that a gain ranging from 18 dB to 29 dB does not impair the resulting SNR of the system, see Paper E.

The major issue with preamplifiers for MRI arrays is that a high input reflection coefficient is required to enable preamplifier decoupling [52]. Preamplifier decoupling is the concept of introducing a high impedance at the coil terminals, hence decreasing the current which is able to flow in the coil. Given inductive coupling between the elements in an array, the high impedance at the coil terminals causes the elements in the array to be decoupled, see Paper D. The requirements for the preamplifier's input impedance is in a range from a short to an ideal inductor, where the size of the inductor implicitly determines the possible preamplifier decoupling because of the

*The MR community seems to be converging towards the wording preamplifier rather than low noise amplifier (LNA).

†In this work F, as opposed to NF, is used. Sometimes NF is used to signify that the unit is dB, rather than decimal. Here, the unit is in decimals unless otherwise noted.

Q-factor of this inductor. Also, as is investigated in Paper F, an ideal preamplifier decoupling arises when a negative input resistance is utilized. This negative input resistance compensates for the loss in the matching and Q-spoiling network.

The required noise parameters of the preamplifier depend on whether the intended use is single or array coils. For single coils the optimal noise match should be equal to the system impedance (which is assumed in this work to be 50 Ω). On the other hand, if the preamplifiers are used for array coils the optimal noise match should not necessarily be 50 Ω because it depends on the amount of noise coupled to other elements (investigated in Section 4.3).

In this chapter, three preamplifier designs are presented. The first design, described in Section 2.2, develops a preamplifier with an optimal noise impedance of 50 Ω with a negative input resistance. Hence, the first design is used as a reference preamplifier for both the single coils described in Chapter 3 and for the 32 channel brain coil in Chapter 4. The second design, found in Section 2.3, describes a preamplifier specifically for array coils where the optimal noise match is different from 50 Ω. Thus, the second design is sub-optimal for single coils, but as will become apparent later, trading off some single coil performance can significantly increase array coil SNR. The third and final design is a cryogenic preamplifier and is described in Section 2.4. However, before the different preamplifier designs are presented some theoretical aspects are introduced.

2.1 Theoretical Foundations

Because the requirements for MRI preamplifiers diverge from the norm, a brief discussion of the repercussions on the gain metrics traditionally used for preamplifier design is described next. Following the section on gain metrics is a description of the RF (Γ_{opt}, R_{n}, F_{min}) and circuit level (V_{n}, I_{n}, Y_{c}) noise parameters. The final topic of this section is the concept of obtaining a highly mismatched input impedance while preserving noise performance. Unless otherwise noted, or explicitly derived, the formulas used in this section are found in either [80] or [81].

2.1.1 Gain

In conventional microwave amplifier design, the transducer, operating, and available power gains are central metrics. Let us investigate these three power gain definitions when the input reflection coefficient of the preamplifier approaches unity. The

operating power gain is defined as

$$G_{\mathrm{o}} = \frac{P_{\mathrm{L}}}{P_{\mathrm{IN}}} = \frac{1}{1-|\Gamma_{\mathrm{IN}}|^2}|S_{21}|^2\frac{1-|\Gamma_{\mathrm{L}}|^2}{|1-S_{22}\Gamma_{\mathrm{L}}|^2}, \tag{2.2}$$

where P_{L} is the power delivered to the load and P_{IN} is the power absorbed by the network. $|S_{21}|$ is the insertion gain, S_{11} is input S-parameter, Γ_{L} is the reflection coefficient of the load, and Γ_{IN} is the input reflection coefficient of the two-port. When the input reflection coefficient approaches unity the power absorbed by the preamplifier approached zero. Hence, the operating power gain tends towards infinity and is thus a poor metric in the case of dissociation preamplifiers. The available power gain is defined as

$$G_{\mathrm{a}} = \frac{P_{\mathrm{AVN}}}{P_{\mathrm{AVS}}} = \frac{1-|\Gamma_{\mathrm{S}}|^2}{|1-S_{11}\Gamma_{\mathrm{S}}|^2}|S_{21}|^2\frac{1}{1-|\Gamma_{\mathrm{O}}|^2}, \tag{2.3}$$

where P_{AVN} and P_{AVS} is the available power from the two-port and the source, respectively. Γ_{S} is the reflection coefficient of the source and Γ_{O} is the reflection coefficient looking into the output of the two-port. Assuming that the preamplifier is matched to 50 Ω on the output and that the source impedance is likewise 50 Ω yields $G_{\mathrm{a}} = |S_{21}|^2$. The transducer gain is defined as

$$G_{\mathrm{t}} = \frac{P_{\mathrm{L}}}{P_{\mathrm{AVS}}} = \frac{1-|\Gamma_{\mathrm{S}}|^2}{|1-S_{11}\Gamma_{\mathrm{S}}|^2}|S_{21}|^2\frac{1-|\Gamma_{\mathrm{L}}|^2}{|1-\Gamma_{\mathrm{O}}\Gamma_{\mathrm{L}}|^2}. \tag{2.4}$$

As was the case with the available power gain, the transducer power gain also equals $|S_{21}|^2$ under the same assumptions. Hence,

$$G_{\mathrm{a}} = G_{\mathrm{t}} = |S_{21}|^2, \tag{2.5}$$

where $|S_{21}|$ is used as the metric for the gain of the preamplifier moving forward.

2.1.2 Noise

This subsection presents the concept of noise in terms of both classical RF parameters and circuit level parameters. Classical RF noise parameters are the optimal noise match (Γ_{opt}), equivalent noise resistance (R_{n}), and minimum noise figure (F_{min}). The circuit level noise parameters are the noise voltage (Vn), current noise (In), and their correlation admittance (Yc)[‡]. Importantly, these are all input referred noise

[‡]The terms impedance, admittance, and reflection coefficient are used interchangeably because their transformations are well defined.

parameters. This is due to the fact that any noise in a two-port can be transformed to these input referred noise parameters. To understand and analyze the noise coupling in array coils it is vital that the circuit level parameters are defined. Whereas when working with RF preamplifiers it is the conventional design procedure to utilize the RF parameters which results in e.g. plotting noise circles. It is more convenient using the RF parameters than the circuit level parameters. Before the conversion between the two parameters are derived, the concept of noise figure is described. The noise figure describes the SNR degradation caused by noise in a two-port,

$$F = \frac{S_\mathrm{i}/N_\mathrm{i}}{S_\mathrm{o}/N_\mathrm{o}}, \tag{2.6}$$

where S_i and N_i is the signal and noise on the input, respectively. S_o is the signal and N_o is the noise on the output. Although there is principally nothing hindering defining the noise figure in amplitude, it is conventionally defined in terms of power and this convention is abided to in this work. The output SNR is further described as

$$\frac{S_\mathrm{o}}{N_\mathrm{o}} = \frac{S_\mathrm{i}G}{N_\mathrm{a} + N_\mathrm{i}G}, \tag{2.7}$$

where G is the gain of the preamplifier and N_a is the added noise. Hence, combining (2.6) and (2.7) yields

$$F = 1 + \frac{N_\mathrm{a}}{N_\mathrm{i}G}. \tag{2.8}$$

The significance of (2.8) is that the noise figure depends not just on the noise added by the two-port, but also the noise input. By definition the input noise temperature is 290 K [79]. Hence, some caution is needed when using the noise figure as a metric for SNR degradation in cryogenic systems because the reference temperature (T_0) is most likely not 290 K. Another metric is the equivalent noise temperature defined as

$$T_\mathrm{e} = (F - 1)\, T_0. \tag{2.9}$$

Hence, noise figure and equivalent noise temperature are interchangeable and are used as such throughout this work. The SNR degradation caused by the noise figure is defined as $1 - 1/F$. As an example, the noise figure of a preamplifier is 0.5 dB ($T_\mathrm{e} \approx 35.4$ K), resulting in an SNR degradation of a room temperature coil of approximately 11 %. If instead a cryogenic coil cooled with liquid nitrogen to 77 K is

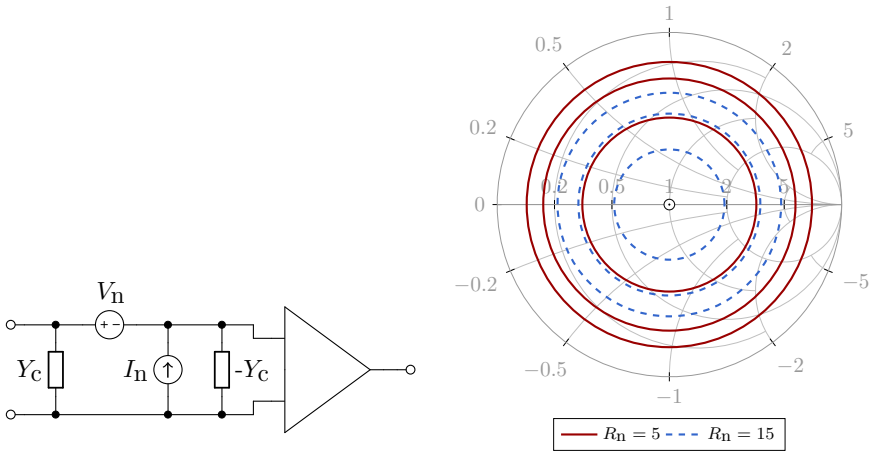

Figure 2.1: (a) input equivalent noise sources and their correlation. (b) calculated noise circles for different R_n in steps of 1 dB.

utilized, $T_0 = 77$, and the noise figure becomes 1.64 dB, resulting in an SNR degradation of approximately 31 %. Thus, in this case, the SNR degradation caused by the preamplifier increases by 20 % when using a cryogenic coil compared to a room temperature coil. Moving forward, unless explicitly noted, the reference temperature $T_0 = 290$ K. Further aspects of this is investigated in Subsection 3.2.3.

Noise from a two-port is completely characterized in terms of its input referred noise parameters. The commonly used equation relating the RF noise parameters is

$$F = F_{\min} + \frac{r_n}{g_s}|y_s - y_{opt}|^2, \tag{2.10}$$

where r_n is the normalized equivalent noise resistance, $y_s = g_s + jb_s$ is the normalized source admittance, and y_{opt} is the normalized optimal noise admittance. Relating the noise figure and the source admittance of (2.10) results in circle equations, described by the center and radius

$$c_F = \frac{\Gamma_{opt}}{1 + k_F}, \tag{2.11}$$

$$r_F = \frac{1}{1 + k_F}\sqrt{k_F^2 + k_F\left(1 - |\Gamma_{opt}|^2\right)}, \tag{2.12}$$

respectively, where $k_F = \frac{F - F_{\min}}{4r_n}|1 + \Gamma_{opt}|^2$. A preamplifier is now assumed to exhibit an optimal noise impedance equal to the source impedance and the minimal noise figure is 0.5 dB. The corresponding noise circles are seen in Fig. 2.1b given an equivalent

noise resistance of either 5 Ω or 15 Ω. Importantly, the noise figure (at the optimal noise impedance) is constant even though the equivalent noise resistance varies.

To perform a detailed circuit analysis of the noise coupling between elements in an array in Chapter 4 the conversion between Γ_{opt}, R_{n}, F_{min} and V_{n}, I_{n}, Y_{c} is described. The bandwidth is assumed to be 1 Hz thus the bandwidth term is neglected in the following equations. See Fig. 2.1a for the schematic of the input referred noise model. The input referred series noise voltage is

$$V_{\mathrm{n}} = 4k_{\mathrm{b}}T_0R_{\mathrm{n}}, \tag{2.13}$$

where k_{b} is the Boltzmann constant. The input referred shunt noise current is

$$I_{\mathrm{n}} = 4k_{\mathrm{b}}T_0G_{\mathrm{u}}, \tag{2.14}$$

where G_{u} is an equivalent (uncorrelated) noise conductance defined as

$$G_{\mathrm{u}} = \left(G_{\mathrm{opt}}^2 - G_{\mathrm{c}}^2\right) R_{\mathrm{n}}, \tag{2.15}$$

where G_{c} is the correlation conductance. $Y_{\mathrm{c}} = G_{\mathrm{c}} + jB_{\mathrm{c}}$ is not an actual admittance but used for including correlation and is described by the correlation conductance

$$G_{\mathrm{c}} = \frac{F_{\mathrm{min}} - 1}{2R_{\mathrm{n}}} - G_{\mathrm{opt}}, \tag{2.16}$$

and the correlation susceptance

$$B_{\mathrm{c}} = -B_{\mathrm{opt}}. \tag{2.17}$$

Similarly, the conversion from the circuit level to RF parameters are

$$R_{\mathrm{n}} = \frac{V_{\mathrm{n}}}{4k_{\mathrm{b}}T_0}, \tag{2.18}$$

$$Y_{\mathrm{opt}} = \sqrt{G_{\mathrm{c}}^2 + \frac{G_{\mathrm{u}}}{R_{\mathrm{n}}}} - jB_{\mathrm{c}}, \tag{2.19}$$

$$F_{\mathrm{min}} = 1 + 2R_{\mathrm{n}}\left(G_{\mathrm{opt}} + G_{\mathrm{c}}\right). \tag{2.20}$$

Using the circuit in Fig. 2.1a and the conversions presented it is possible to perform circuit analysis of the noise using the conventional RF parameters. However, it is not only gain and noise which is important when designing preamplifiers for HMR. Also, the input impedance is of key importance when dealing with array coils and is described in the following.

2.1.3 Input Impedance

The input impedance of the preamplifier implicitly defines the degree of achievable decoupling between elements in an array. The theory and design procedure for constructing preamplifiers with optimal input impedance while maintaining noise performance is described in depth in Paper A, and is thus only described in very brief terms here. Fig. 2.2 is reproduced from Paper A and shows (a) an overview of the preamplifier divided into three two-ports and (b) simulated input impedance circles for different stages in the design. The equations governing the design are

$$\Gamma^{(\mathrm{T})} = S_{11}^{(\mathrm{T})} + \frac{S_{12}^{(\mathrm{T})} S_{21}^{(\mathrm{T})} \Gamma^{(\mathrm{O})}}{1 - S_{22}^{(\mathrm{T})} \Gamma^{(\mathrm{O})}}, \tag{2.21}$$

$$\Gamma^{(\mathrm{P})} = S_{11}^{(\mathrm{I})} + \frac{{S_{21}^{(\mathrm{I})}}^2 \Gamma^{(\mathrm{T})}}{1 - S_{22}^{(\mathrm{I})} \Gamma^{(\mathrm{T})}}. \tag{2.22}$$

Hence, if the isolation of the transistor is non-zero, it is possible to adjust the input impedance of the preamplifier while the optimal noise match remains constant. In Fig. 2.2b, $\Gamma^{(\mathrm{T})}$ is the reflection coefficient of the transistor, $\Gamma^{(\mathrm{In})}$ is the resulting reflection coefficient of the preamplifier when it is noise matched, $\Gamma^{(\mathrm{P,initial})}$ is the initial reflection coefficient, and $\Gamma^{(\mathrm{P})}$ is the final reflection coefficient of the preamplifier. The circles represent the impedance that can be realized when $\Gamma^{(\mathrm{O})} < 1$. This concept is used extensively in the following three design implementations. The first preamplifier design, described in the following section, is used as a reference for both the single and array coils in later chapters.

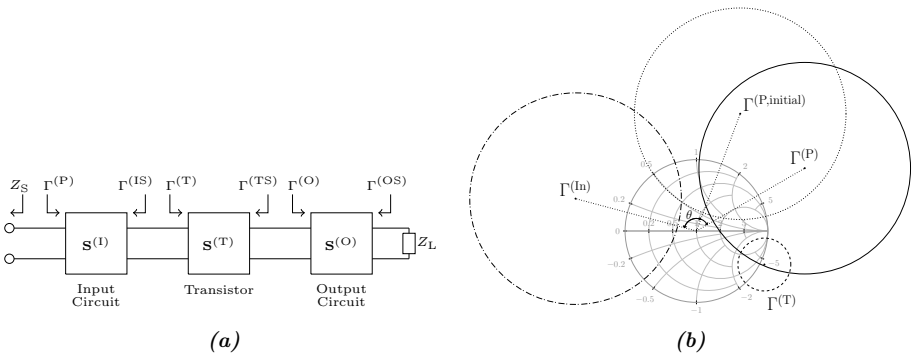

Figure 2.2: (a) Overview of the preamplifier which is divided into three two-ports; input circuit, transistor and output circuit. (b) impedance circles realizable with a passive output circuit. The figures are reproduced from Paper A.

2.2 Design 1: Optimal Noise Figure

The first preamplifier design optimizes the noise figure by ensuring an approximately 50 Ω optimal noise impedance while exhibiting a high input reflection coefficient. This design improves upon the preamplifier presented in Paper A by further simplifying the input network, adding transmit protection, and embedding the active decoupling signal. The schematic of the preamplifier and associated power supply is found in Fig. 2.3. The noise figure matching is achieved by C2, C5, and L1 in Fig. 2.3a. The biasing network consisting of R1, R2, R3, R4, C3, C4, and L1 ensures low frequency stability and a biasing voltage of approximately 0.5 V. Low frequency stability is

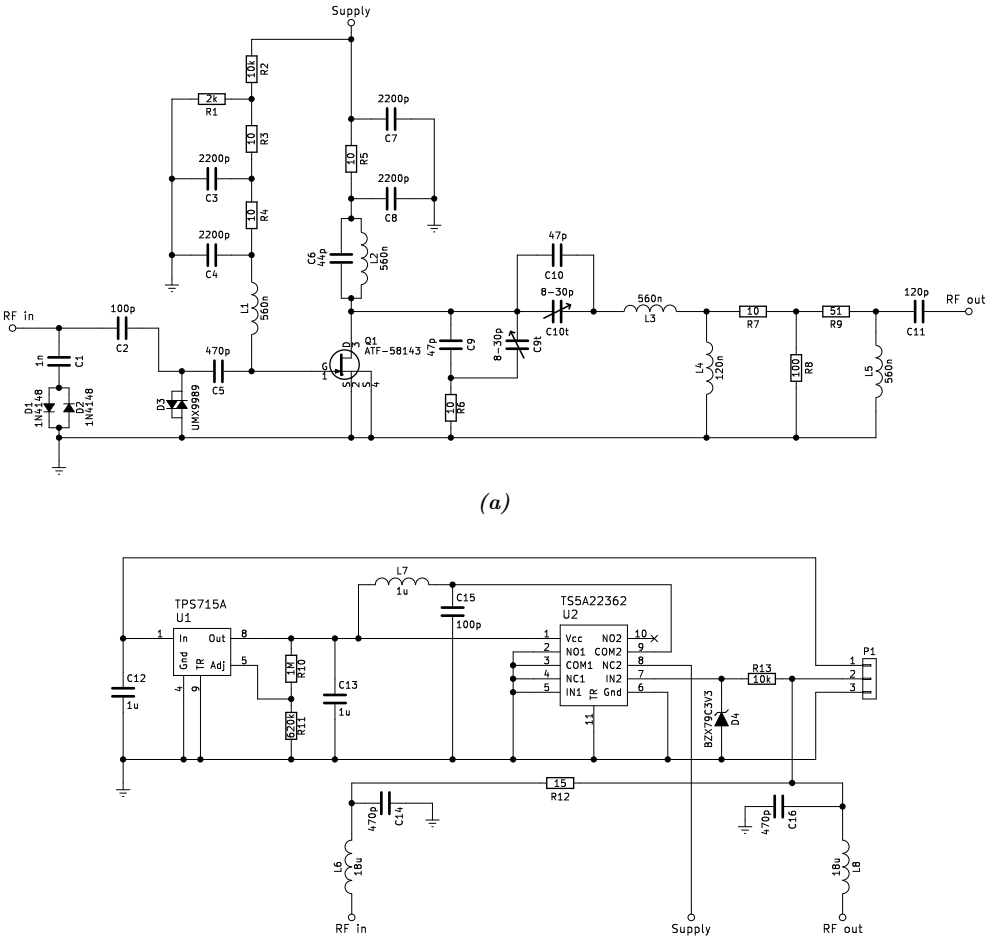

Figure 2.3: Schematics of (a) the preamplifier and (b) the power supply.

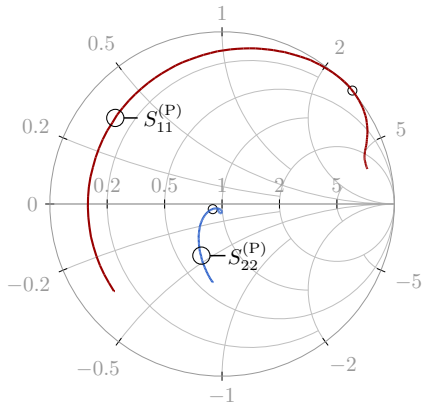

(a)

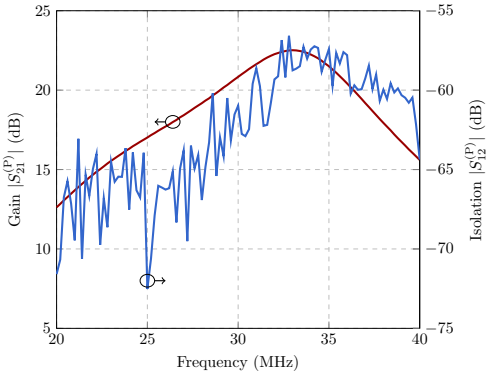

(b)

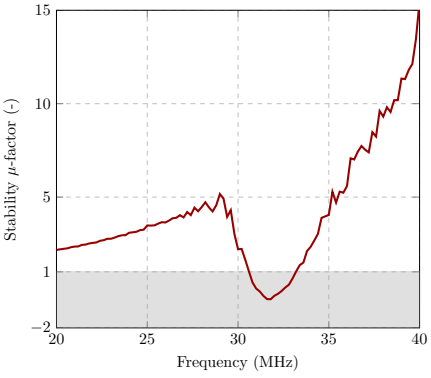

(c)

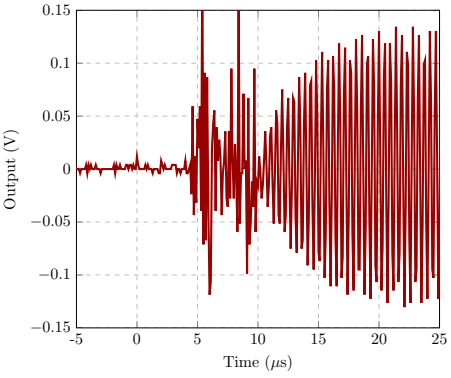

(d)

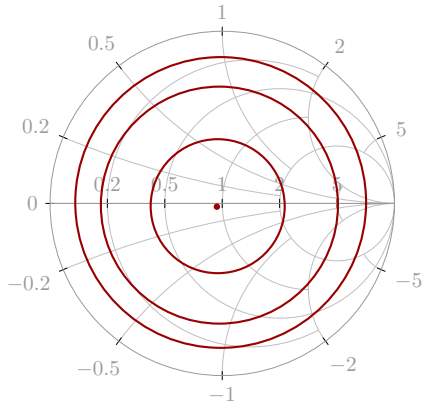

(e)

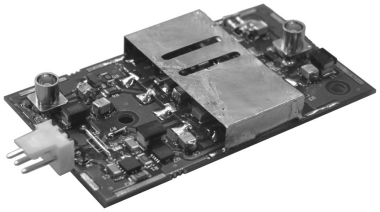

(f)

Figure 2.4: Characteristics of the preamplifier. (a) measured input and output impedance. (b) measured gain and isolation. (c) measured stability factor. (d) measured switching time of the power supply. (e) simulated noise circles. (f) picture of the preamplifier.

primarily ensured by the resonance of L1 and C4 which is approximately 4.5 MHz. The crossed diodes D1, D2, and D3 ensures protection against the transmit pulse. To be able to adjust the input impedance tunable capacitors C9t and C10t are utilized. C9t together with C9 and R6 form a low pass filter seen from the output of the transistor. Hence, adjusting C9t the impedance seen from the drain of the transistor changes. C10, C10t, L3 forms a series resonance and by adjusting C10t the resonance is tuned. This series resonance ensures that the input reflection coefficient is only high in a narrow bandwidth, which in turn ensures that the preamplifier is only potentially unstable in a narrow bandwidth. R7, R8, and R9 is an attenuator which decreases the gain of the preamplifier and thus increases stability. L5 and C11 match the output of the preamplifier to 50 Ω.

The power supply is seen in Fig. 2.3b. Pin 1 of P1 is the 10 V supply from the scanner. A surface mounted non-magnetic regulator (U1) is configured by R10 and R11 to output 3.15 V at pin 8 of U1. The regulated voltage is filtered by C13, L7, and C15 before it is fed to a switch, pin 9 of U2. The switch (U2) is implemented as an additional transmit protection because the preamplifiers exhibit negative input impedance. Pin 8 of U2 is the switched voltage supply. The switch is controlled on pin 7 where D4 and R13 is connected. The Q-spoiling signal comes from either pin 2 of P1 or the RF out and is -5 V during reception and 150 mA during transmission. Hence, D4 and R13 ensures that the voltage on pin 7 of U2 does not exceed -0.4 V (knee voltage of D4) or +3.3 V (conduction voltage of D4). R13 limits the current of D4. L6 and L8 are feeding inductors and are connected to the input and output of the preamplifier.

The measured input and output impedance is seen in Fig. 2.4a. The input impedance is -0.8+j134 Ω. The small negative resistance compensates for the loss in the matching and Q-spoiling circuit and thus a very high preamplifier decoupling is possible, as detailed in Paper F. The gain, $|S_{21}|$, of the preamplifier is approximately 22 dB and the isolation, $|S_{12}|$, is approximately -60 dB as seen in Fig. 2.4b. All S-parameters are measured using a two-port vector network analyzer. The measured stability factor is seen in Fig. 2.4c. The preamplifier is only potentially unstable in a narrow bandwidth around 32.1 MHz, and otherwise unconditionally stable. Having a negative input impedance it is impossible to achieve an unconditionally stable preamplifier. Importantly, the system remains stable if the total resistance of the system is larger than zero. The coil is matched at 50 Ω and thus the total system resistance is 49.2 Ω. Hence, the system is stable. However, if the coil is highly mismatched the system can become unstable and start to oscillate. The measured switching time of the preamplifier is seen in Fig. 2.4d where the preamplifier is in steady state after approximately

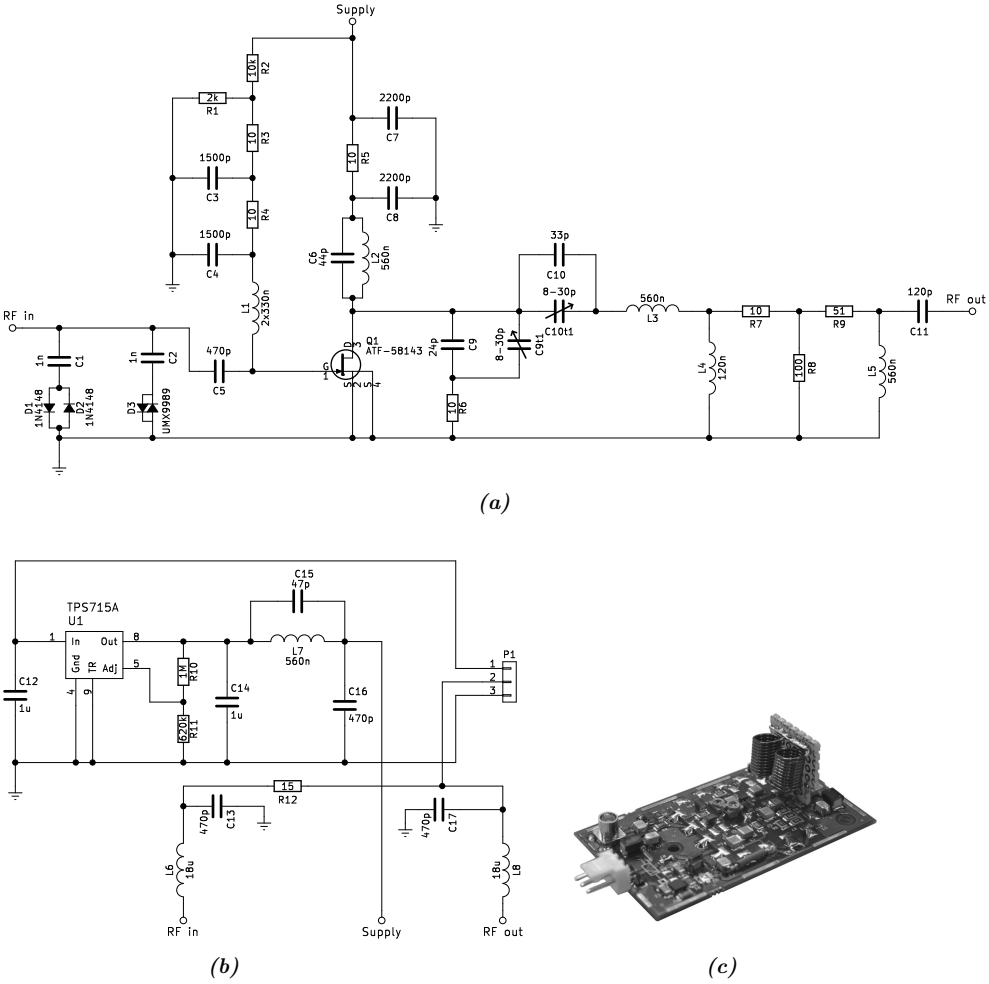

Figure 2.5: Schematics of (a) the preamplifier and (b) the power supply and (c) is a picture of the second preamplifier design.

20 μs. Simulated noise figures are found in Fig. 2.4e where the noise parameters are $R_{\mathrm{n}} = 1.021\ \Omega$, $F_{\mathrm{min}} = 0.186$ dB, and $\Gamma_{\mathrm{opt}} = -0.031 - j0.019$. The measured noise figure in 50 Ω is 0.45 dB. This is, however, within expected uncertainties as detailed in Paper G. An image of the preamplifier is seen in Fig. 2.4f.

2.3 Design 2: Minimized Array Noise

The second design is based heavily upon the first with only a few details changed. These changes, however, show a tremendous difference in the performance of an array

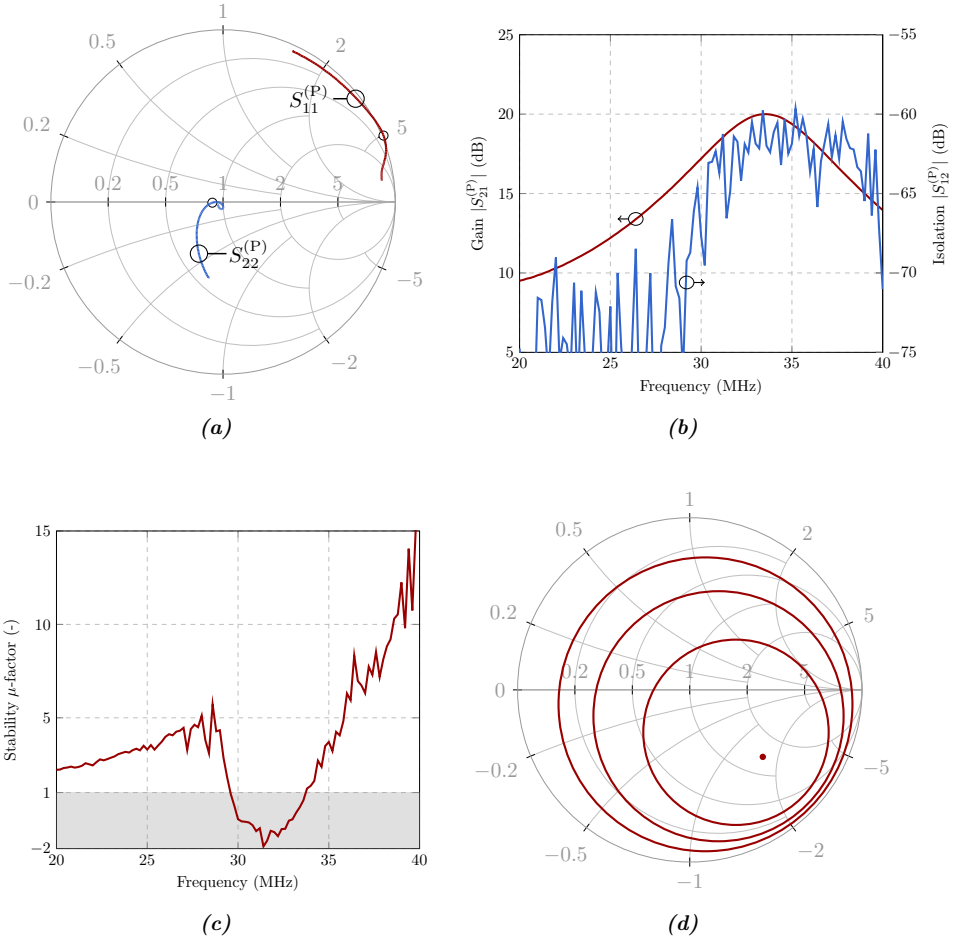

Figure 2.6: Characteristics of the preamplifier. (a) measured input and output impedance. (b) measured gain and isolation. (c) measured stability factor. (d) simulated noise circles.

coil, as is shown later. In this section, a design for minimizing the noise and thus maximizing SNR in an array is presented. The fundamental principle is that the optimal noise impedance should only be 50 Ω in the case of using a single coil. When multiple coils are coupled the noise from the preamplifiers couple through the coils and thus decrease the SNR significantly. Hence, by changing the optimal noise impedance it is possible to achieve an SNR gain of more than 40 %. The schematic of the preamplifier for minimizing array noise is seen in Fig. 2.5a. The changes from the previous design is primarily in the input circuit. Now, L1 is 2x330 nH air wound inductors. Combined with the lower C4 this yields an optimal noise match $\Gamma_{\text{opt}} = 0.424 - j0.389$. Double crossed diodes for transmit protection are still utilized (D1,

D2, D3). Further, the power supply, shown in Fig. 2.5b, has been revised. It was found that the switch in design 1 is not needed for transmit protection. Hence, it has been removed. Also, an additional parallel resonance is placed in series with the voltage supply to further filter potential noise on the supply line (L7, C15).

The measured input and output impedance is seen in Fig. 2.6a. The measured input impedance is -5.6+j251 at 32.1 MHz which was tuned to exhibit more than 50 dB of preamplifier decoupling. The measured gain is approximately 18 dB with an isolation below -60 dB, depicted in Fig. 2.6b. The stability factor shown in Fig. 2.6c shows that the preamplifier is potentially unstable from approximately 29 MHz to 34 MHz. This is an increase over the previous design but posed no issues during implementation in a prototype array described in Section 4.3. Finally, the simulated noise parameters (Fig. 2.6d) are $R_{\mathrm{n}} = 1.779\ \Omega$, $F_{\mathrm{min}} = 0.092$ dB, and $\Gamma_{\mathrm{opt}} = 0.424 - j0.389$. The measured noise figure is 0.5 dB in 50 Ω and is again accounted for by the measurement uncertainty.

2.4 Design 3: Cryogenic

The final preamplifier design presented in this chapter is based on design 1 and cooled by liquid nitrogen to 77 K. In Paper B the concepts of cryogenic preamplifiers are discussed in detail. However, in Paper B, even though the preamplifier exhibits a high input reflection coefficient, it is not designed specifically for array coils. Hence, this section describes, in brief, the latest design version of a cryogenic preamplifier for array coils. Based on the analysis in Paper B, the only change to the schematic in Fig. 2.3a is that R2 is 6.7 kΩ for the cryogenic preamplifier. The power supply is the same as seen in Fig. 2.3b but is not placed in the liquid nitrogen. The resulting bias voltage is approximately 0.75 V resulting in a DC current of the transistor of 104 mA at room temperature, exceeding the maximum safe operating value. However, at 77 K the DC current decreases to 48 mA which is the same as design 1. The preamplifier was placed in a styrofoam box and coaxial cables were added to the input and output of the preamplifier.

Measurements of the input and output impedance is found in Fig. 2.7a. The input impedance at 32.1 MHz is -8+j533 Ω. The phase of the input impedance is shifted because the coaxial cables used to connect to the preamplifier inside the liquid nitrogen adds additional phase. The gain is approximately 22 dB with an isolation of approximately -60 dB (Fig. 2.7b). The measured stability factor is found in Fig. 2.7c and shows similar results to that of the previous designs. The measured noise figure in 50 Ω is 0.05 dB.

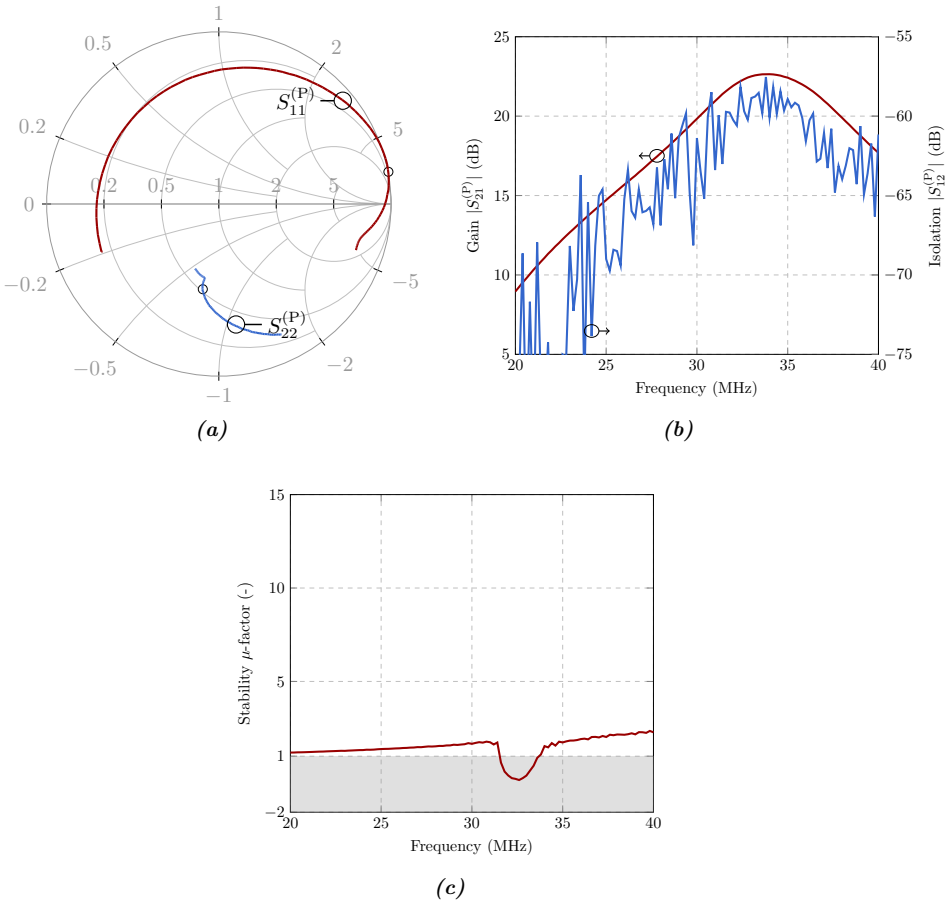

(a) *(b)* *(c)*

Figure 2.7: Characteristics of the preamplifier. (a) measured input and output impedance. (b) measured gain and isolation. (c) measured stability factor.

2.5 Summary

This chapter presented requirements for the preamplifiers, which diverge from conventional RF preamplifiers. The primary requirement is that the preamplifier should exhibit a high input reflection coefficient while maintaining noise performance.

Additionally, three different preamplifier designs were presented using the design procedure published in Paper A. Preamplifier design 1 (PD1) is used as a reference and is noise matched to 50 Ω while exhibiting an inductive, negative resistance input impedance. The reason for utilizing a negative resistance is covered in Paper F. The second preamplifier design (PD2) is designed to maximize SNR of an array

coil following the analysis of noise coupling in Chapter 4. It is noise matched to $\Gamma_{\text{opt}} = 0.424 - j0.389$ while showing a noise figure of 0.5 dB (in 50 Ω). The third, and final, preamplifier design (PD3) is a cryogenic version of PD1. The design is based on Paper B and achieves a noise figure of 0.05 dB while maintaining an inductive, negative resistance input impedance.

The three designs are further developments of what was presented in Paper A and B and are used in the following chapters.

Volume Coils 3

Volume coils have been and still are the back-bone for MRI. Hence, this chapter devotes attention to the investigation of two volume coils for both room temperature and cryogenic operation. Especially for transmit purposes the volume coils find their merit. A wide selection of volume coils are available such as the solenoid [82, 83], Alderman-Grant (saddle) [84, 85], Helmholtz [86], litz [87], and birdcage coil [26, 88]. In this chapter the primary focus is on volume coils for small animal imaging where a standard low pass birdcage coil (Section 3.2) and a variant of the solenoid coil (Section 3.3) is investigated. The reason for investigating volume coils for small animal scanning is a consequence of the high sample loading of volume coils for human imaging. In short, for cryogenic cooling to yield proper SNR gain the sample loading of the coil must be small, which is not usually the case of volume coils for clinical applications. This is described theoretically in the following section.

3.1 Comparative SNR

The basis of comparative SNR is the principle of reciprocity described in depth by e.g. Hoult et al. [82, 83, 89]. Conceptually, the principle of reciprocity states that the magnetic field produced by a coil at a point in space (given unit current in the coil) is proportional to the voltage (principally the electromotive force) induced in the coil by a magnetic dipole placed in the same point in space. Hence, the transmit field of a coil implicitly yields the receive sensitivity of the coil. The relative SNR of a coil is usually described by [90]

$$\psi \propto \frac{B_1}{I\sqrt{T_\mathrm{c}R_\mathrm{c} + T_\mathrm{s}R_\mathrm{s}}}, \tag{3.1}$$

where T_c and R_c is the temperature and equivalent resistance of the coil, respectively. T_s and R_s is the likewise the temperature of the sample and the equivalent resistance of the sample introduced into the coil, respectively. I is the current in the coil. For some coil topologies (3.1) is easily applicable such as surface coils where it is (principally) simple to simulate or measure the resistance of the coil and the sample directly. However, for e.g. a birdcage coil, extracting the equivalent resistances is not immediately apparent. Additionally, applying 1 A to a quadrature tuned birdcage coil is also not apparent. Hence, the relative SNR is often described in terms of the

power absorbed by the coil and sample, [90]

$$\psi \propto \frac{B_1}{\sqrt{T_\mathrm{c} R_\mathrm{c} I^2 + T_\mathrm{s} R_\mathrm{s} I^2}} \tag{3.2}$$

$$\propto \frac{B_1}{\sqrt{T_\mathrm{c} P_\mathrm{c} + T_\mathrm{s} P_\mathrm{s}}}, \tag{3.3}$$

where P_c and P_s is the power absorbed by the coil and sample, respectively. Simulating the absorbed power in the coil and sample is possible using a time-domain solver (e.g. FDTD). However, when designing coils that are electrically small the simulation time quickly becomes infeasible. For room temperature coils, the sample and coil is assumed at the same temperature, $T_\mathrm{c} = T_\mathrm{s}$. Thus (3.3) simplifies to

$$\psi \propto \frac{B_1}{\sqrt{T_\mathrm{c} P_\mathrm{T}}}, \tag{3.4}$$

where $P_\mathrm{T} = P_\mathrm{c} + P_\mathrm{s}$ is the total power. Given that the total power is equal when comparing two coils, the comparative SNR, based on (3.4), is

$$\Psi_\mathrm{R} = \frac{\psi^{(1)}}{\psi^{(2)}} = \frac{B_1^{(1)}}{B_1^{(2)}}, \tag{3.5}$$

where $\psi^{(1)}$ and $\psi^{(2)}$ is the relative SNR of an improved and reference coil respectively. Hence, (3.5) is easy to evaluate using a frequency domain solver which decreases simulation time by a substantial amount compared to using a time domain solver for electrically small coils. However, (3.5) is only valid when the coils and sample are at the same temperature, and thus of no use when comparing room temperature and cryogenic coils. A traditional derivation is based on (3.1) where it is assumed that the two coils are at different temperatures, but otherwise equal

$$\Psi_\mathrm{C,R} = \sqrt{\frac{T_\mathrm{s} R_\mathrm{s} + T_\mathrm{c}^{(\mathrm{r})} R_\mathrm{c}^{(\mathrm{r})}}{T_\mathrm{s} R_\mathrm{s} + T_\mathrm{c}^{(\mathrm{c})} R_\mathrm{c}^{(\mathrm{c})}}}, \tag{3.6}$$

where superscripted (r) and (c) indicate the room temperature and cryogenic coil respectively. A more convenient form of (3.6) is

$$\Psi_\mathrm{C,Q} = \sqrt{\frac{T^{(\mathrm{r})} \cdot {Q_\mathrm{u}^{(\mathrm{r})}}^{-1} + T^{(\mathrm{r})} \cdot {Q_\mathrm{s}^{(\mathrm{r})}}^{-1}}{T^{(\mathrm{c})} \cdot {Q_\mathrm{u}^{(\mathrm{c})}}^{-1} + T^{(\mathrm{r})} \cdot {Q_\mathrm{s}^{(\mathrm{c})}}^{-1}}}, \tag{3.7}$$

where Q_u is the unloaded Q-factor, and $Q_\mathrm{s}^{-1} = Q_\mathrm{l}^{-1} - Q_\mathrm{u}^{-1}$ where Q_l^{-1} is the loaded Q-factor. As the cryogenic temperature approaches zero, the SNR gain approaches

$$\Psi_\mathrm{U} = \lim_{T^{(\mathrm{c})} \to 0} \Psi_\mathrm{C,Q} = \sqrt{\frac{1}{1 - \frac{Q_\mathrm{l}^{(\mathrm{r})}}{Q_\mathrm{u}^{(\mathrm{r})}}}}, \tag{3.8}$$

where Ψ_U is the ultimate or ideal SNR gain. Hence, if the loaded Q-factor equals the unloaded Q-factor the maximal theoretical SNR gain is infinite. However, as the loaded to unloaded Q-factor decreases from unity, the maximum SNR gain is also decreased. Thus, it is paramount to minimize the sample loading of the coil before cooling (without impairing the B_1 field).

The problem with (3.7) is the fact that it compares only coils which are, besides their temperature, equal. To compare for example a room temperature birdcage with a cryogenic surface coil another derivation is needed for the general case when the coils are not the same temperature and not equal. The general derivation takes its origin in (3.2). The unloaded to loaded Q-factor is described by

$$\frac{Q_\mathrm{u}}{Q_\mathrm{l}} = \frac{\frac{|X|}{R_\mathrm{c}}}{\frac{|X|}{R_\mathrm{c}+R_\mathrm{s}}} = \frac{R_\mathrm{c} + R_\mathrm{s}}{R_\mathrm{c}} = 1 + \frac{R_\mathrm{s}}{R_\mathrm{c}}, \tag{3.9}$$

where $X = \omega L$ and L is the inductance of the resonator. Further,

$$R_\mathrm{c} I^2 + R_\mathrm{s} I^2 = P_\mathrm{T}, \tag{3.10}$$

where $I^2 = \frac{P_\mathrm{T}}{R_0}$ and $R_0 = R_\mathrm{c} + R_\mathrm{s}$. Now, combining (3.9) and (3.10) yields

$$R_\mathrm{c} = \frac{R_0 Q_\mathrm{l}}{Q_\mathrm{u}}, \tag{3.11}$$

$$R_\mathrm{s} = R_0 \left(1 - \frac{Q_\mathrm{l}}{Q_\mathrm{u}}\right). \tag{3.12}$$

The relative SNR in terms of the Q-factors is now given by (3.2), (3.11), and (3.12) as

$$\psi \propto \frac{B_1}{\sqrt{P_\mathrm{T}\left[T_\mathrm{c}\frac{Q_\mathrm{l}}{Q_\mathrm{u}} + T_\mathrm{s}\left(1 - \frac{Q_\mathrm{l}}{Q_\mathrm{u}}\right)\right]}}. \tag{3.13}$$

In the case when $T_\mathrm{c} = T_\mathrm{s}$, (3.13) simplifies to (3.4). Finally, the comparative SNR in

the general case, assuming $P_{\mathrm{T}}^{(\mathrm{r})} = P_{\mathrm{T}}^{(\mathrm{c})}$, is

$$\Psi_{\mathrm{Q}} = \frac{B_1^{(\mathrm{c})}}{B_1^{(\mathrm{r})}} \sqrt{\frac{T_{\mathrm{c}}^{(\mathrm{r})} \frac{Q_{\mathrm{l}}^{(\mathrm{r})}}{Q_{\mathrm{u}}^{(\mathrm{r})}} + T_{\mathrm{s}} \left(1 - \frac{Q_{\mathrm{l}}^{(\mathrm{r})}}{Q_{\mathrm{u}}^{(\mathrm{r})}}\right)}{T_{\mathrm{c}}^{(\mathrm{c})} \frac{Q_{\mathrm{l}}^{(\mathrm{c})}}{Q_{\mathrm{u}}^{(\mathrm{c})}} + T_{\mathrm{s}} \left(1 - \frac{Q_{\mathrm{l}}^{(\mathrm{c})}}{Q_{\mathrm{u}}^{(\mathrm{c})}}\right)}}. \tag{3.14}$$

A very important aspect of (3.14) is the fact that it is defined with a constant power applied to the coil rather than unit current. Hence, even though coils are equal (except temperature) the B_1 terms must be included. This is the same as (3.4). Hence, (3.14) makes calculation of the comparative SNR between any coil straight forward using any field solver (time or frequency domain). Having described the theoretical foundations of comparative SNR, the following section utilizes these insights to design a cryogenic birdcage coil for small animal imaging.

3.2 Cryogenic Birdcage*

Since the advent of the birdcage coil in the 1980s it has, probably, become the most used coil for clinical scanning for 1.5 and 3 T [91]. This is due to its inherent small form factor, natural alignment with the patient (as opposed to solenoid coils), very good homogeneity, and excellent SNR. By many researchers and clinicians, the birdcage coil is regarded as the reference coil to which other coils must prove their worth. This section begins by exploring the usage of birdcage coils for human subjects at room and cryogenic temperatures. However, as will be shown, cryogenic birdcage coils are not ideal for human subjects due to high sample loading. Hence, the latter part of this section presents a cryogenic birdcage for small animal scanning.

In Fig. 3.1a a birdcage coil is shown for human head/brain imaging. A birdcage is structured by two end rings and a number of legs. The number of legs typically vary from eight to 32 depending on required FOV and homogeneity. Generally, two types of birdcage coils exist; low- and high-pass (with a bandpass type a combination of the two). The low-pass birdcage coil (Fig. 3.1a) has capacitors mounted on the legs whereas the high-pass type has capacitors mounted on the end rings. The capacitors ensure a correct phase shift between the loops formed by the end rings and legs such that a circulating current follows. Another advantage of the birdcage coil is its natural ability to be quadrature excited (generate a circularly polarized B_1 field) by adding a second feeding port 90 degrees shifted relative to the first feeding port. Operating the birdcage coil in quadrature then requires the addition of a hybrid coupler.

*Some of the content of this chapter is reproduced from Paper H.

3.2.1 Human Brain Imaging

The birdcage coil in Fig. 3.1a is 24 cm in diameter with a length of 25 cm fitting a human head. It has 16 legs, is made of 1 cm wide copper, and is quadrature excited.

The simulated B_1 fields are found in Fig. 3.1b, 3.1c, and 3.1d. From a qualitative point of view the homogeneity looks good, especially in the XY-plane (Fig. 3.1d). The generated B_1 field is approximately 2 mT when excited with 1 W. Hence, the birdcage coil has a good efficiency in relation to its excited volume.

The simulated unloaded Q-factor is 1220, whereas the loaded Q-factor is 43. Using (3.8) to estimate the maximum SNR gain possible results in $\Psi_U = 1.8$ %. Thus, it is not feasible to utilize cryogenic birdcage coils for human head/brain imaging, even

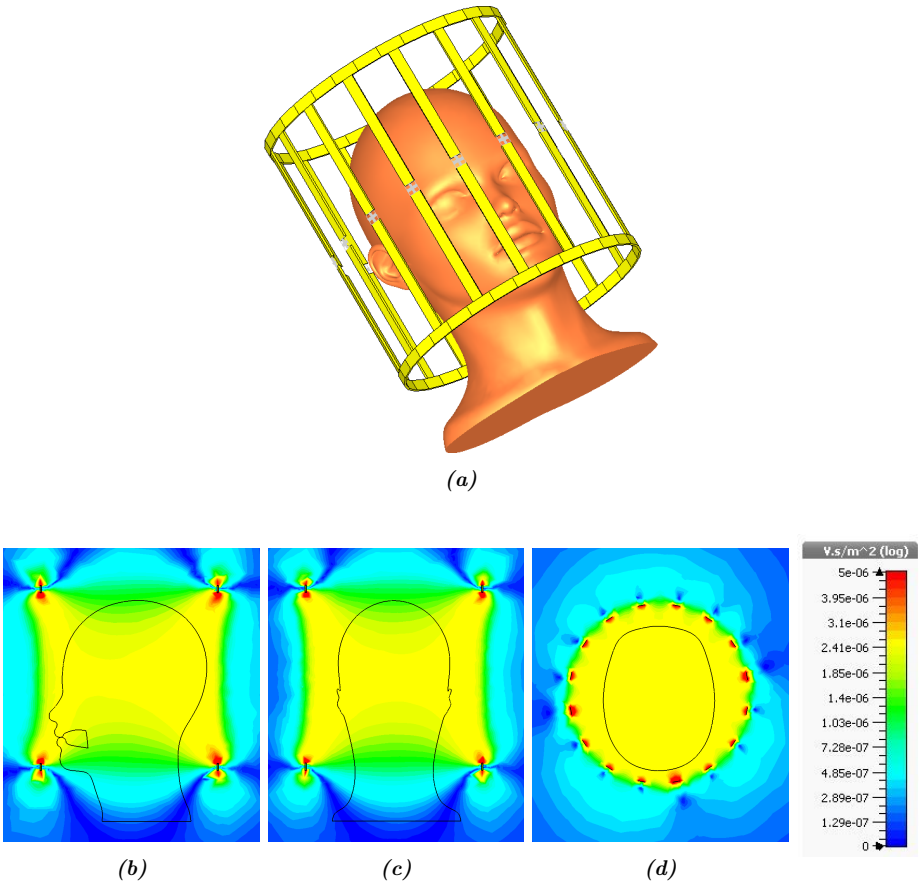

(a)

(b) *(c)* *(d)*

Figure 3.1: Geometry (a) and simulated B_1 fields (b, c, d) of a birdcage coil for human brain imaging.

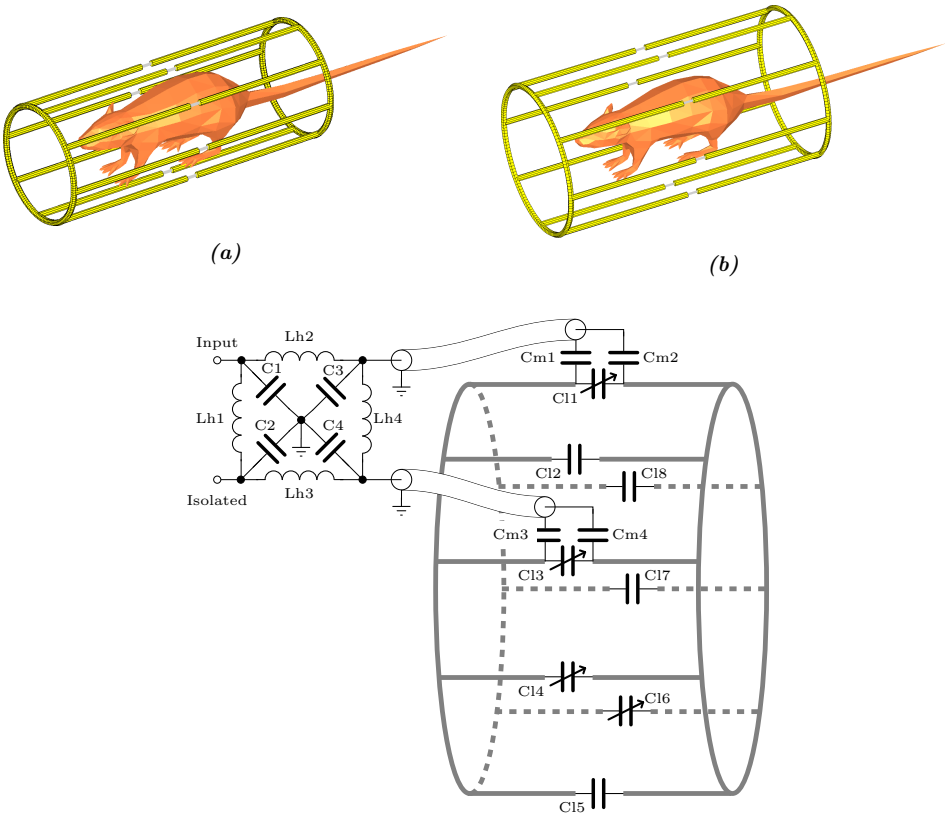

Figure 3.2: Small animal birdcages with (a) 35 mm bore and (b) 50 mm bore, and (c) is a schematic of the implemented birdcage coil including the hybrid coupler.

when imaging ^{13}C at 3 T. Hence, for ^{1}H imaging, due to the higher dielectric constant of the human body, the sample loading is higher and the use of cryogenics becomes even more futile.

3.2.2 Small Animal Imaging

Instead of focussing on human imaging using birdcage coils it makes sense to investigate the application of small animal imaging, such as mice. An example of a birdcage for a mouse is seen in Fig. 3.2a. The birdcage coil is 35 mm in diameter, has a length of 100 mm and has 8 legs. The simulated unloaded Q-factor is 508 and the loaded Q-factor is 503. Hence, the ideal SNR gain is approximately 100 times that of the room temperature equivalent. However, this is only in the limit of 0 K. Using liquid

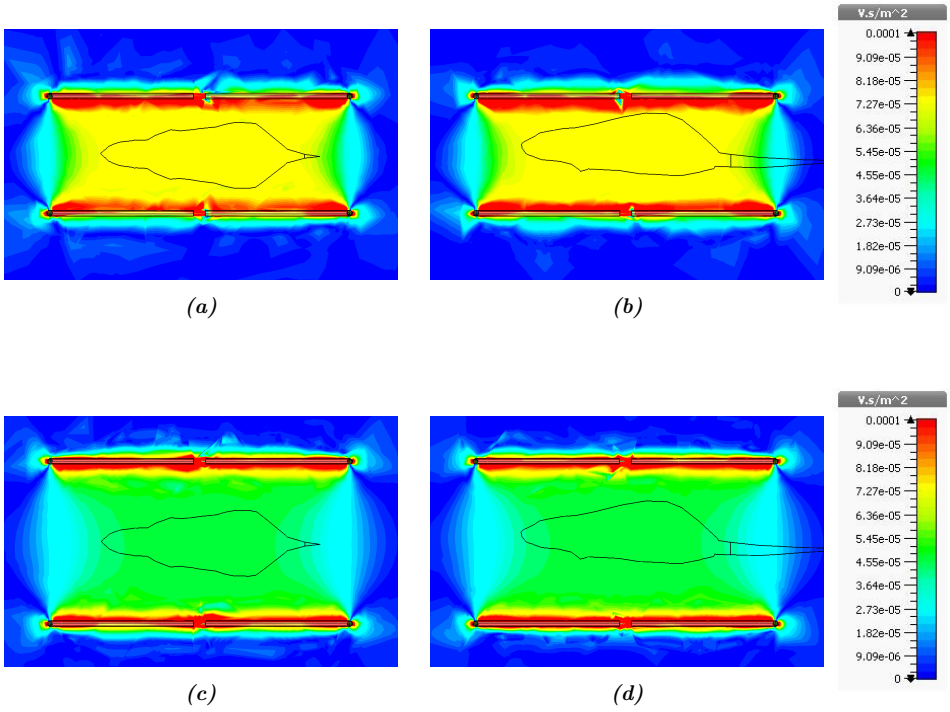

Figure 3.3: Simulated B_1 fields of the birdcage coils with 35 mm bore (a, b) and 50 mm bore (c, d). (a) and (c) are in the XZ-plane. (b) and (d) are in the XY-plane.

nitrogen (77 K) is a cost effective means of cooling and is used in this work. For simplicity copper is utilized instead of e.g. HTS. Further, due to practical limitations a 50 mm diameter birdcage is utilized instead of the 35 mm. Simulated unloaded Q-factor for the 50 mm bore is 505 with a loaded Q-factor of 503. This results in $\Psi_{\mathrm{U}} = 252$. However, the increased bore size impairs the B_1 field as shown in Fig. 3.3. The mean B_1 field is approximately 69 mT for the 35 mm bore and 47 mT for the 50 mm bore. Hence, an SNR loss of approximately 32 % entails from the larger bore size. In spite of the SNR loss when using a larger bore, the resulting ultimate SNR gain is still in favour of the larger bore. Another aspect is the homogeneity, defined as the standard deviation of B_1, which is 0.36 mT and 0.58 mT for the 35 mm and 50 mm bore, respectively. The homogeneity is simulated in the mouse, excluding the tail.

For comparing the room temperature and cryogenic performance of the 50 mm bore birdcages, two low-pass eight-rung birdcage coils operated in quadrature as both transmit and receive where constructed using 2 mm diameter copper wire. The fab-

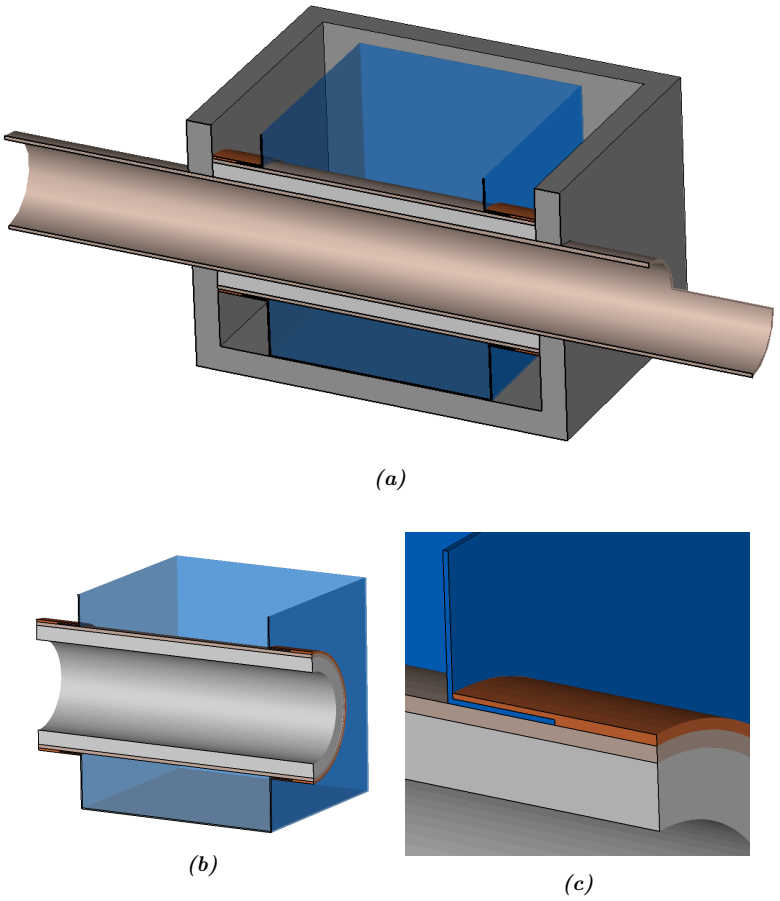

Figure 3.4: Cryostat. (a) shows a 3D model of the cryostat with a cut plane. (b) shows the cryo-bag insert and (c) is a zoom in of the cryo-bag insert showing the kapton tape being wrapped around the bag.

ricated birdcage coils are 100 mm in length with an inner diameter of 51.5 mm. The size of the birdcage coils does not reflect an optimal geometry, however, it provides a larger FOV. The room temperature birdcage coil uses, in each leg, 170 pF placed at the center of the leg. The coupling to the birdcage coil is capacitive (series) and matches the coil to the hybrid coupler. The two matching circuits are placed at a 90 degree angle to provide quadrature operation. Further, two variable capacitors are used in the legs to provide symmetry recovery. They are placed at a 90 degree angle compared to each other and at a 45 degree angle compared to the feed point. The hybrid coupler connects to the T/R switch and the preamplifier. The cryogenic birdcage coil is similar except for the component values.

The cryostat, detailed in Fig. 3.4, is comprised of three primary parts: A styrofoam

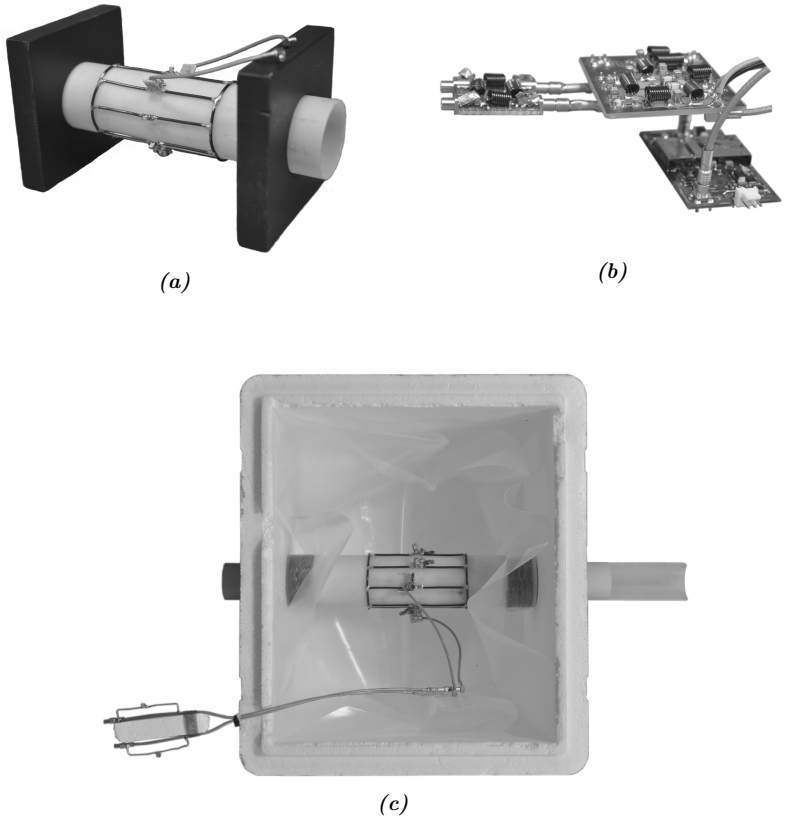

(a) *(b)* *(c)*

Figure 3.5: Images of the implemented coils. (a) shows the room temperature birdcage. (b) shows the quadrature hybrid, T/R switch, and preamplifier. (c) shows the cryogenic birdcage and cryostat (excluding the top cover). Figures reproduced from Paper H.

box (300 mm by 200 mm by 100 mm with thickness 20 mm), a tubular animal bed of glass fiber (inner radius of 17.5 mm with thickness 1.5 mm), and the cryogenic insert. The cryogenic insert, detailed further in Fig. 3.4b and 3.4c, consists of four parts: Insulation (with inner radius of 19 mm and thickness of 6 mm), a glass fiber tube (inner radius of 25 mm with thickness 1.5 mm) onto which the coil is mounted, a plastic bag, and Kapton tape which is taped over the lip of the plastic bag. The implemented coils, cryostat, and RF front end is seen in Fig. 3.5.

To assemble the cryostat first the coil is mounted on the glass fiber tube. Then, the lip of the plastic bag is made by cutting a circle of diameter 40 mm and pulling the circular hole over the glass fiber tube. The Kapton tape is then taped over the lip of the plastic bag where it is crucial that no folds occur in the first layer. Ten layers of tightly wounded Kapton is applied. The insulation is then pushed into the glass fiber

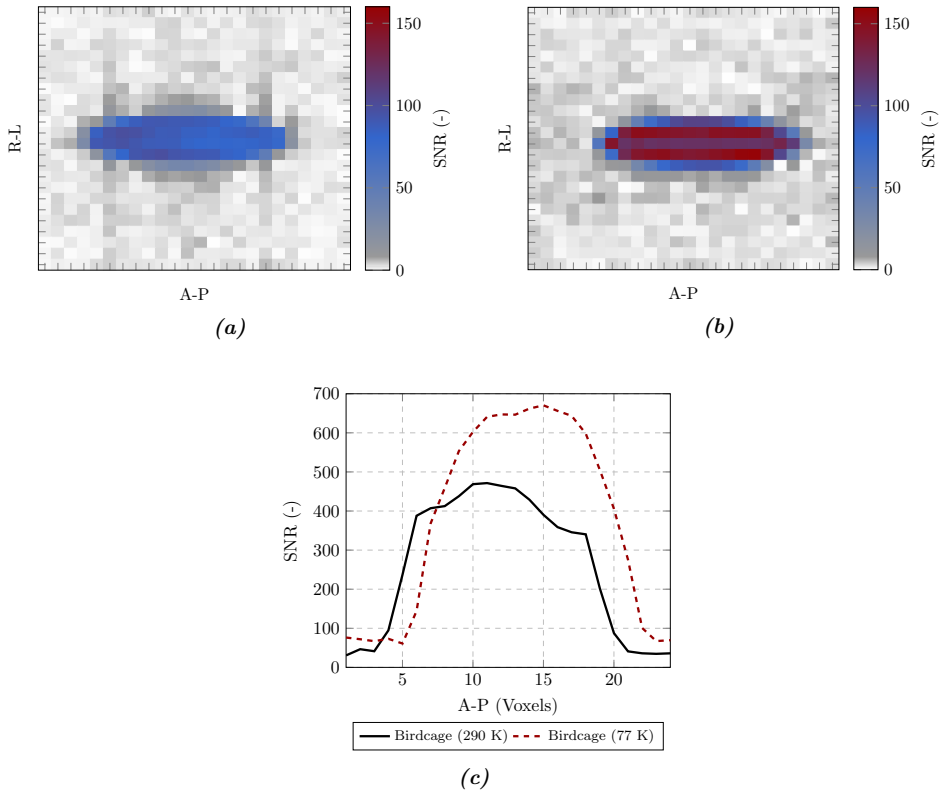

Figure 3.6: Measured SNR of the birdcage coil (a) at 290 K and (b) at 77 K. (c) the summed SNR comparing the room temperature and cryogenic birdcage coil.

tube. Now, the cryogenic insert is placed in the styrofoam box and the animal bed slides through the styrofoam box and cryogenic insert. Liquid nitrogen is now filled into the plastic bag until it submerges the coil completely.

The two coils were characterized on the bench and measured at 32.1 MHz (^{13}C) in a clinical 3T scanner (MR750, GE Healthcare, Waukesha, WI, USA) using a CSI sequence with TR=500 ms and 30 degree flip angle. The sample was a 50 ml tube with 30 mm diameter and length of 120 mm filled with ethylene glycol mixed with 17 g/L of NaCl (to provide adequate loading).

Bench measurements show $Q_{\mathrm{u}}^{(\mathrm{r})} = 362$, $Q_{\mathrm{l}}^{(\mathrm{r})} = 356$, $Q_{\mathrm{u}}^{(\mathrm{c})} = 627$, and $Q_{\mathrm{l}}^{(\mathrm{c})} = 616$. The corresponding SNR gain calculated using (3.7) yields 2.5. The measured SNR in the scanner is seen in Fig. 3.6 for the anterior-posterior (A-P) and right-left (R-L) orientations. The maximum achieved SNR for the room temperature birdcage is approximately 470 and 670 for the cryogenic birdcage. This amounts to an SNR gain

of approximately 42 % when cooling the birdcage coil to 77 K. The achieved SNR gain is indeed a ways from the expected of 150 %. However, the impairment of the room temperature hybrid coupler, T/R switch, and preamplifier has thus far been neglected.

3.2.3 RF Front End

Many articles dealing with cryogenic coils assume that the RF front end is the same for both the room temperature and cryogenic coil [37]. However, this is not a good assumption because the noise figure of the RF front end is defined in terms of the noise on the input, which depends on the temperature. Hence, even though the RF front end is physically the same for the two cases, the noise figure changes in respect to the reference temperature. In this subsection, formulas are presented for including the noise of the RF front end based on noise figure simulations or measurements. Further, it is shown that, in many cases, excluding the noise added by the RF front end yields too optimistic SNR gain estimates.

The RF front end is in this work assumed to be the electronics from the coil, besides matching, up to and including the preamplifier. This is due to Friis' equation for noise,

$$F^{(\mathrm{RF})} = F^{(\mathrm{H})} + \frac{F^{(\mathrm{Sw})} - 1}{G_{\mathrm{Av}}^{(\mathrm{H})}} + \frac{F^{(\mathrm{P})} - 1}{G_{\mathrm{Av}}^{(\mathrm{H})} G_{\mathrm{Av}}^{(\mathrm{Sw})}}, \tag{3.15}$$

where $F^{(\mathrm{RF})}$, $F^{(\mathrm{H})}$, $F^{(\mathrm{Sw})}$, and $F^{(\mathrm{P})}$ are the noise figures of the RF front end, the hybrid coupler, the T/R switch, and the preamplifier, respectively. $G_{\mathrm{Av}}^{(\mathrm{H})}$ and $G_{\mathrm{Av}}^{(\mathrm{Sw})}$ is the available gain of the the hybrid coupler and T/R switch, respectively. The reason for including the noise only up to and including the preamplifier is because the noise figure impairment is mitigated by the gain of the preamplifier. By definition, $F = \frac{1}{G_{\mathrm{Av}}}$ for a passive two-port at room temperature. Hence, (3.15) simplifies to,

$$F^{(\mathrm{RF})} = \frac{F^{(\mathrm{P})}}{G_{\mathrm{Av}}^{(\mathrm{H})} G_{\mathrm{Av}}^{(\mathrm{Sw})}}. \tag{3.16}$$

In (3.7) it is assumed that the preamplifier only adds a negligible amount of noise. However, if the preamplifier is used for both the room temperature and cryogenic coil, the noise figure (and thus the SNR impairment) increases as the reference temperature drops. This is because the noise figure is a relative measure. The reference temperature is the equivalent noise generated by a resistor, usually $T_{\mathrm{ref}} = 290$ K.

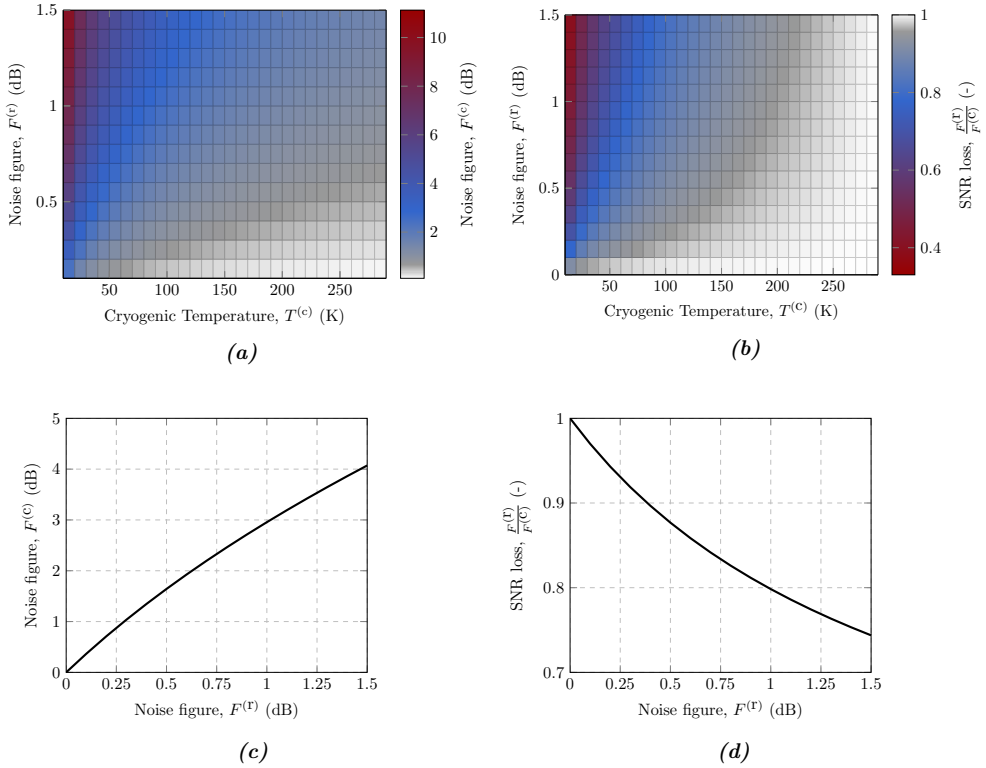

Figure 3.7: Simulated additional SNR loss from RF front end. (a) shows the noise figure and (b) the SNR loss as a function of the noise figure at room temperature and the cryogenic temperature. (c) and (d) shows the noise figure and SNR loss as a function of room temperature noise figure, when the cryogenic temperature is 77 K.

Hence, when the reference temperature changes the noise figure also changes. The equivalent noise temperature is defined as

$$T_{\mathrm{e}}^{(\mathrm{r})} = T_{\mathrm{ref}} \left(F^{(\mathrm{r})} - 1 \right), \tag{3.17}$$

where $F^{(\mathrm{r})}$ is the noise figure of the RF front end measured at a given reference temperature T_{ref}. Hence as the reference temperature is decreased by cooling the coil, while the equivalent noise temperature of the RF front end remains constant, the resulting cryogenic noise figure increases as described by

$$F^{(\mathrm{c})} = \frac{T_{\mathrm{e}}^{(\mathrm{r})}}{T^{(\mathrm{c})}} + 1. \tag{3.18}$$

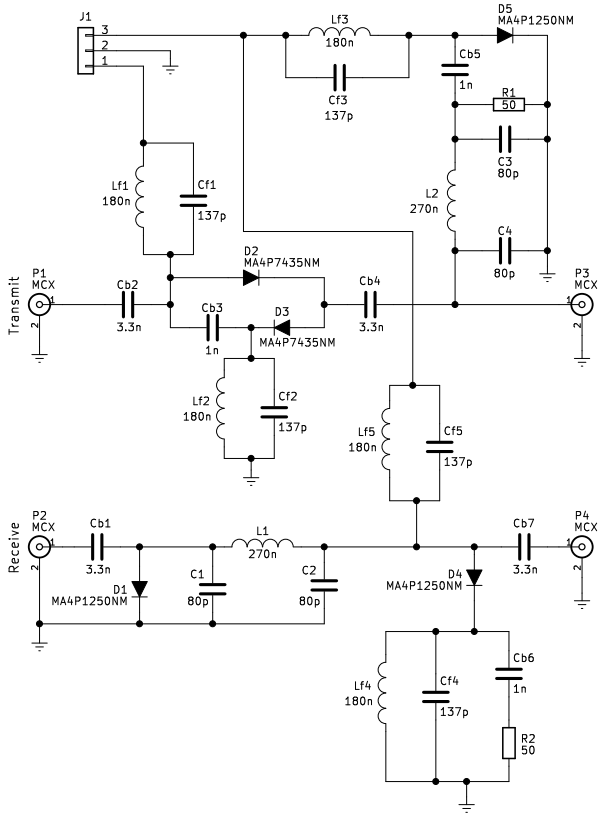

Figure 3.8: Schematic of the transmit/receive switch.

Extending (3.7) with (3.17) and (3.18) yields

$$\Psi_{\text{coil+preamp}} = \Psi_{\text{coil}} \sqrt{\frac{F^{(\text{r})}}{F^{(\text{c})}}} \tag{3.19}$$

$$= \Psi_{\text{coil}} \sqrt{\frac{F^{(\text{r})} T^{(\text{c})}}{T_{\text{ref}} \left(F^{(\text{r})} - 1 \right) + T^{(\text{c})}}}. \tag{3.20}$$

The consequence of (3.20) is that when using a room temperature RF front end for a cryogenic coil, the expected SNR gain decreases. This is because the noise figure increases when a cryogenic coil is used because the reference noise decreases. This is plotted in Fig. 3.7. What is also highlighted is that the impairment of the RF front end increases almost exponentially when the coil temperature tends towards 0 K. In Fig.3.7a the resulting noise figure of the RF front end is plotted as a function of the temperature of the coil and noise figure at room temperature. This is further detailed in Fig. 3.7c for 77 K. Interestingly, when the noise figure of the RF front end at room

temperature is 1 dB, the resulting noise figure when utilizing a cryogenic coil at 77 K is 3 dB. The SNR loss is shown in Fig. 3.7b as a function the cryogenic temperature and noise figure at room temperature. Further, the SNR loss at 77 K is shown in Fig. 3.7d. Given a room temperature noise of the RF front end of 1 dB the resulting loss in SNR gain is approximately 20 %.

The schematic of the hybrid coupler used for the room temperature and cryogenic birdcage coils is seen in Fig. 3.2c. The custom made T/R switch is seen in Fig. 3.8. The connectors P3 and P4 are connected to the hybrid coupler's input and isolated port, respectively. When transmitting, pin 3 of J1 is biased with approximately 345 mA. This current is shared between PIN diodes D1, D4, and D5 resulting in 115 mA bias for each of the diodes. This means that the RF equivalent of the PIN diode is a short. L2, C3, and C4 constitute a 90 degree phase shifter and the corresponding impedance is thus high. The same applies to L1, C1, and C2. The shorting of D4 results in a 50 Ω equivalent resistance. This ensures that the hybrid coupler is appropriately loaded while transmitting and thus remains balanced. Pin 1 of J1 is biased with approximately 150 mA, which forward biases D2 and D3. D2 and D3 are placed in this 'crossed' configuration to ensure that neither diode is driven into reverse bias by the resulting voltage when transmitting with high power. When a positive voltage is applied from P1 to P3, D2 is forward biased. Now, when a negative voltage across P1 and P3 is applied, if D3 was not present, the biasing voltage of D2 should be sufficiently high, such that D2 is not driven into reverse bias. This can result in a very high DC current. By adding D3, when a negative voltage across P1 and P3 is applied, D3 is forward biased and no problems with reverse bias occurs. Hence, the biasing current should only make sure that D2 and D3 are conducting to avoid non-linear modulation of the transmit signal. In receive mode, pin 1 and 3 of J1 are reverse biased with -5 V. Hence, the RF equivalent of all PIN diodes is an open circuit. This results in a 50 Ω load looking into P3 (toward P1) while the path from P4 to P2 is now low loss. Cb signifies DC blocking capacitors, and Lf and Cf signifies feeding components. In terms of the feeding components, a conventional approach is to use an electrically large inductor. However, electrically large inductors tend to exhibit high loss. Hence, usage for cryogenic purposes would result in additional power dissipation inside the cryogen, which is unwanted. Instead, a parallel resonance circuit using high Q-factor inductors is implemented.

The measured loss of the receive path for the T/R switch and hybrid coupler at 290 K is 0.45 dB. The preamplifier exhibits a 0.45 dB noise figure. Hence, the total noise figure of the RF front end is 0.9 dB. This amounts to an additional SNR loss of 19 %. The expected SNR gain of the cryogenic birdcage is thus 2 instead of 2.5 when

utilizing a room temperature RF front with the cryogenic birdcage.

The RF front end was also cooled to 77 K. The loss of the hybrid coupler and T/R switch was measured to be 0.32 dB. Preamplifier design 3 is utilized exhibiting a noise figure of 0.05 dB. Hence, the noise figure of the RF front end amounts to 0.136 dB, which in turn yields an SNR gain decrease by 4 %. The expected SNR gain, if using a cryogenic RF front end, is thus 2.4.

3.2.4 Discussion

The performance of the cryogenic birdcage coil for small animal imaging has an ideal SNR gain which is 2.5, when cooled to 77 K using liquid nitrogen. However, an SNR gain of only 1.43 has been realized in practise. This is in part due to the usage of a room temperature RF front end which impairs the potential SNR gain to 2.0. Further, the discrepancy in predicted and measured SNR gain might be due to a faulty capacitor when cooling the coil. The terminals of the capacitors tend to break. Thus, the coil can pass testing on the bench, however, in the scanner the environment may cause problems. This could be vibrations causes by gradient switching which triggers a crack in a terminal of a capacitor.

If the RF front end is also cooled to 77 K the corresponding noise figure is decreased from 0.9 dB to 0.136 dB. This decrease in noise figure amounts to an impairment on the SNR gain caused by the RF front end which is decreased from 19 % to 4 %. Yielding an expected SNR gain of 2.4 when cooling both the coil and RF front end. Hence, it is vital to also cool the RF front end to deliver on the theoretical SNR gain of the coil.

However, this is for similar bore size coils. A smaller birdcage coil (bore of 35 mm) was simulated showing an approximate 46 % increased SNR over the 50 mm bore coil. Hence, the cryogenic coil (including cryogenic RF front end) potentially offers 63 % better SNR than the smaller bore coil. Given a thinner isolation, required to maintain room temperature inside the bore, it is possible to either use a larger bore size and thus larger samples, or decrease the bore size and thus gain more SNR. This is possible by utilizing a vacuum chamber as described in [92]. Hence the potential isolation thickness is decreased from 10 mm to 3 mm and the potential SNR gain is recovered. Thus, it is possible in theory to achieve an SNR gain in excess of the 'magic' two times, which is the somewhat arbitrary number in which it is assumed that cryogenics will be worthwhile to use, despite the additional complexities.

3.3 Paranoide

In the early days of MRI, the solenoid coil was the prevalent detection coil. It offers, in principle, superior homogeneity and sensitivity compared to a birdcage coil. However, it must be placed perpendicular to the main field and is thus impractical for human imaging. Especially at higher field strengths and thus higher frequency the solenoid coil losses out to the birdcage coil because the solenoid coil becomes radiative. Hence, at higher field strengths the solenoid coil begins to act more as a helical antenna and a significant sensitivity loss follows. In an attempt to challenge the birdcage as the premium volume coil for small animal imaging this section presents the concept of a paranoide coil.

3.3.1 Design

The basic idea is to route several solenoids in parallel. This increases the homogeneity and resonance frequency of the coil. The paranoide is seen in Fig. 3.9. An early iteration of the paranoide was a solenoid with a copper sheet. This does increase the homogeneity and resonance frequency, however, it also shields the sample from the transmit field. Hence, the solenoid constructed with a sheet, requires a T/R switch. The addition of extra circuitry increases loss and thus lowers sensitivity. Hence, the idea of using a sheet was not pursued further. Instead, to avoid shielding of the sample, the concept of the paranoide combined with a Helmholtz transmitter coil was implemented. The Helmholtz and paranoide coils are inherently decoupled because of their linearly polarized orthogonal B_1 fields.

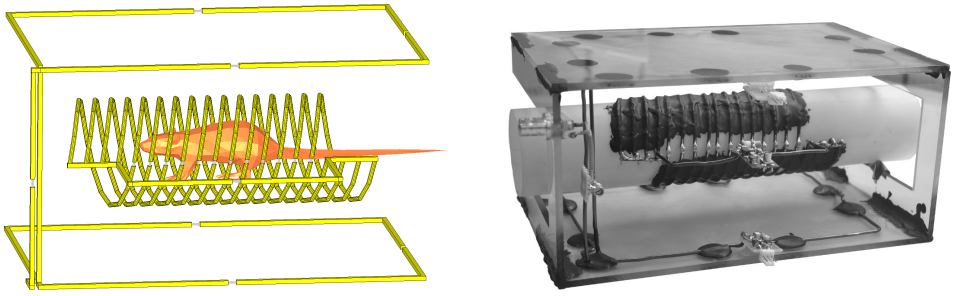

(a) *(b)*

Figure 3.9: Small animal paranoide combined with a Helmholtz transmitter. (a) is a 3D model and (b) is the implemented coil.

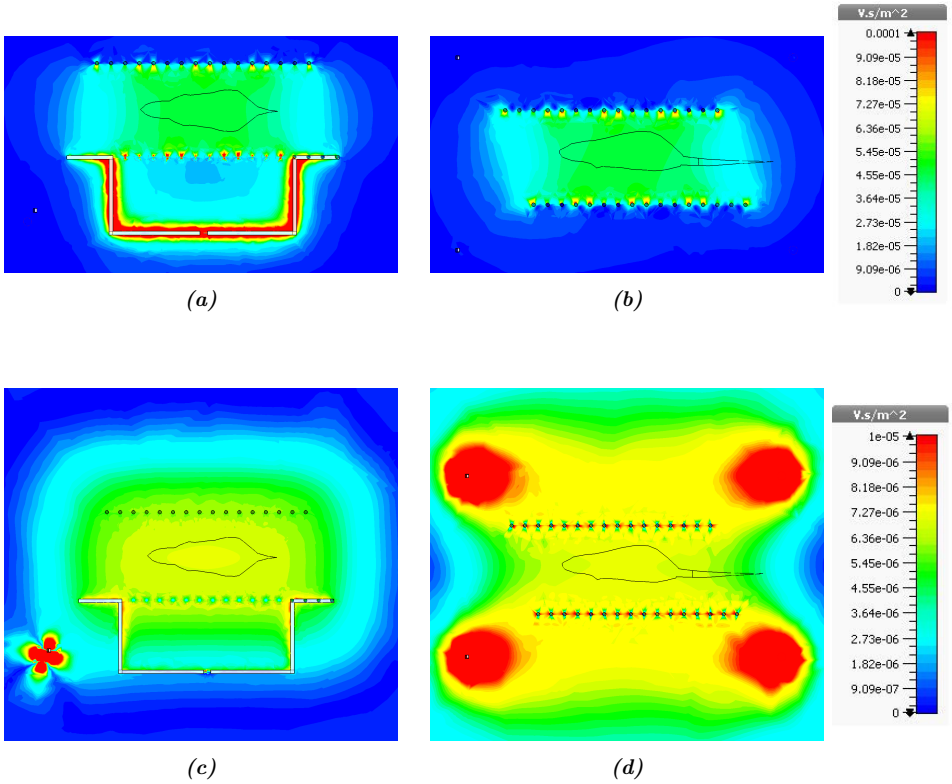

Figure 3.10: Simulated B_1 fields of the paranoide (a, b) and Helmholtz coil (c, d). (a) and (c) is in the XZ-plane. (b) and (d) is in the XY-plane.

The investigated topology of combining solenoids in parallel (paranoide) for receive with a Helmholtz coil for transmit is seen in Fig. 3.9. Both coils are constructed using 2 mm diameter copper wire. The paranoid is constructed by placing four solenoids with four windings in parallel. The individual solenoids are segmented by three capacitors to avoid excessive shifting of the resonance frequency. The bore size is 50 mm, and the paranoide is mounted on a glass fiber tube with a thickness of 1 mm. Hence the diameter of the paranoide is 52 mm. To cover the approximate FOV of a mouse with acceptable homogeneity, a length of 150 mm is required. The Helmholtz transmitter is glued to 5 mm bicarbonate plates. The length and width is 180 mm and 120 mm, respectively, with a height of 100 mm. The Helmholtz coil is segmented by six capacitors. In two positions, however, a PIN diode switch is mounted, to further increase the decoupling in receive mode between the paranoide and Helmholtz coil.

3.3.2 Results

Simulations of the B_1 fields of the paranoide and Helmholtz coils are seen in Fig. 3.10. The paranoide exhibits a mean B_1 field of approximately 46 mT with a standard deviation of 0.87 mT. Hence, the paranoide coil has an expected SNR performance which is equal to that of the birdcage coil detailed in the previous section. The Helmholtz coils exhibits a mean B_1 field of 6.4 mT with a standard deviation of 106 uT. The much worse B_1 field of the Helmholtz coil is of no major concern because it is only used as a transmitter. Hence, by applying more power the lower B_1 field (at 1 W) is easily compensated.

The measured unloaded Q-factor is 320, while the loaded Q-factor drops to 277. Hence, the unloaded to loaded Q-factor is approximately 1.16.

Imaging experiments are found in Fig. 3.11 where the paranoide is compared to the 50 mm bore birdcage presented in the previous section. The peak SNR of the bird-

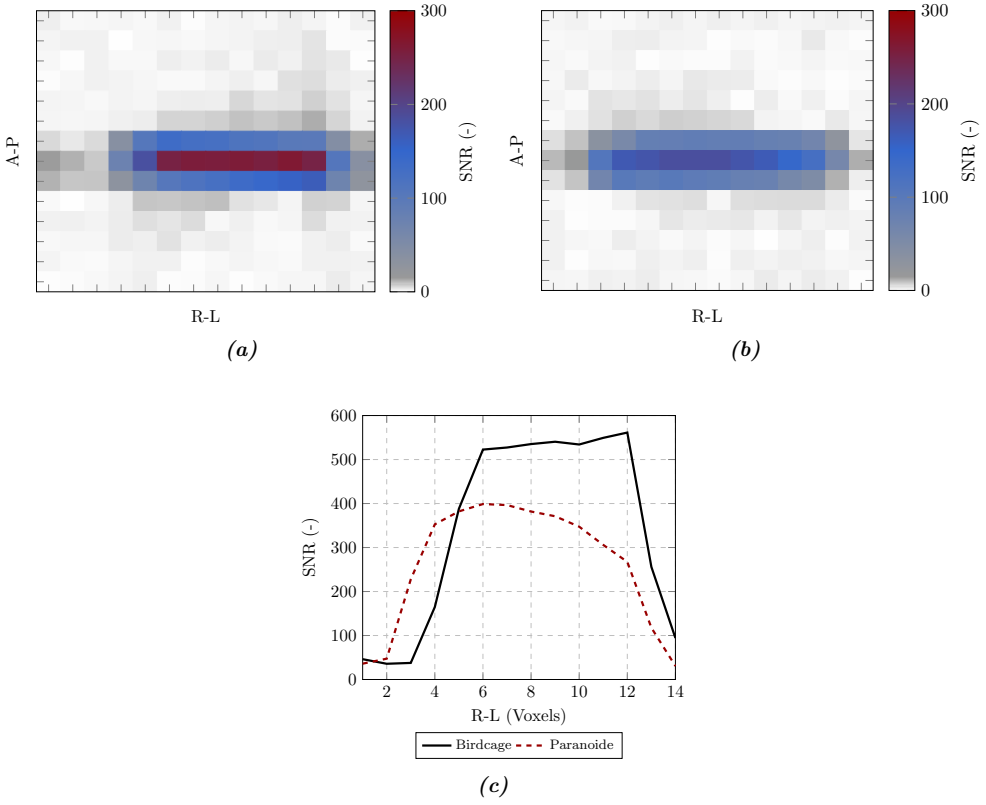

Figure 3.11: Measured SNR of the birdcage coil (a) and the paranoide (b). (c) the summed SNR comparing the paranoide and birdcage coil.

cage coil is approximately 263 and approximately 184 for the paranoide coil. Hence, comparing the peak SNR the paranoide is 30 % worse that the birdcage coil. Looking at Fig. 3.11c, it can be speculated that the homogeneity of the paranoid is also significantly worse than the birdcage coil. This is not too surprising when looking at the simulated B_1 field because the inhomogeneity of the paranoide coil and the Helmholt coil stacks.

3.3.3 Discussion

The loss in SNR of 30 % is surprising. However, it is potentially a consequence of the sensitive nature of the paranoide coil. The paranoide coil is highly sensitive to its environment. Metal, even some 10-20 cm from the paranoide coil, causes a not insignificant shift of the resonance frequency. Hence, the paranoide coil might be mismatched to the preamplifier when placed in the scanner. The mismatch (given that the preamplifier has an optimal noise impedance of 50 Ω) results in a higher effective noise figure of the preamplifier and could easily account for the impaired SNR as compared to simulations. Now, even if the paranoide had similar SNR and homogeneity compared to the birdcage coil, it would not be a serious contender. Simply because it is more sensitive to sample loading and it must be placed perpendicular to the main field making it more difficult to work with.

3.4 Summary

Theoretically comparing the potential SNR gain of coils at different temperatures is a fundamental prerequisite of designing cryogenic coils. The first section described some well-known formulas in terms of both normalized current and power. The equations for predicting SNR gain using normalized power was extended to also include the effects of different temperatures of the coils. This enables the comparison of both structural and temperature different coils.

Using these formulas for SNR gain a cryogenic birdcage coil for small animal imaging was designed and implemented. It promises an SNR gain of 2.4 times, when both the coil and RF front is cooled to 77 K. Further, including the noise of the RF front end in the SNR gain calculation is paramount.

Lastly, a contender to the birdcage coil was examined. However, the paranoide coil shows a measured 30 % decrease in SNR over the birdcage coil and is more prone to environmental changes. Hence, it is not viable in comparison with the birdcage coil.

32 Channel Brain Coil 4

The brain is of particular interest for HMR because metabolism in the brain of ^{13}C is correlated with neurological diseases such as multiple sclerosis [93], Alzheimer's [94–97], Parkinson's [98–101], as well as cancer tumours [102, 103]. The quintessential work by Roemer et al. [52] demonstrated the extension of single surface coils to arrays, proving that increased SNR is obtainable by utilizing phased coil arrays. The usage of coil arrays also enables the use of parallel acquisition by exploiting the uniqueness of the individual coil elements' sensitivity profiles. One major challenge of HMR is the inherent transient nature of the polarization which relaxes on a time scale of 60 s. Hence, for e.g. brain imaging obtaining an image of the entire brain, with acceptable SNR, is a major challenge using volume coils. However, using coil arrays it is possible to decrease the acquisition time by combining coil arrays and parallel imaging. Another critical aspect of array coils is the fact that they can achieve the ultimate SNR in the center of a head with as few elements as 12 (for ^{1}H imaging). By increasing the channel count (assuming that the electronic noise remains neglectable) the ultimate center SNR is not impaired. However, the increased channel count has a large impact on the ability of the array to perform parallel imaging.

This chapter covers the design and implementation of a 32 channel brain coil for ^{13}C imaging which is presented in the following sections. Using non-overlapped elements increase parallel imaging capabilities, but as will be analyzed in Section 4.3 can also severely impair the SNR because of noise coupling from the preamplifiers. This noise coupling is a problem when using room temperature coil arrays and devastating in the case of cryogenic coil arrays.

4.1 Methods

4.1.1 Design

The housing for the brain coil was acquired from RAPID Biomedical GmbH and is seen in Fig. 4.1. It is a rigid plastic frame measuring 197 mm in the R-L orientation and 220 mm in the A-P orientation. The height of the housing is 50 cm where there is room in the top part for the preamplifiers.

All coil elements are constructed with 2 mm diameter copper wire. Each element has a

proton block which is made by bending the copper wire (making a small inductor) and adding a parallel capacitor, Cp in Fig. 4.2. There are no segmenting capacitors used because the sample loading causes no significant shift of the resonance frequency. The matching circuit (Fig. 4.2) features double safety by active and passive Q-spoiling. D1 and D2 shorts Lq creating a parallel resonance with Cq. C1 and C2 are the tune and match capacitors. C3 enables tuning of the preamplifier decoupling. PD1 (Section 2.2) is used as the preamplifier. The input impedance of the preamplifier exhibits a small negative resistance. The negative resistance compensates for the loss in the matching network and enables preamplifier decoupling of more than 50 dB.

The geometry is shown in Fig. 4.1. Viewing the coil from the top, the coils are numbered counter clockwise from superior to inferior starting at the left eye. The

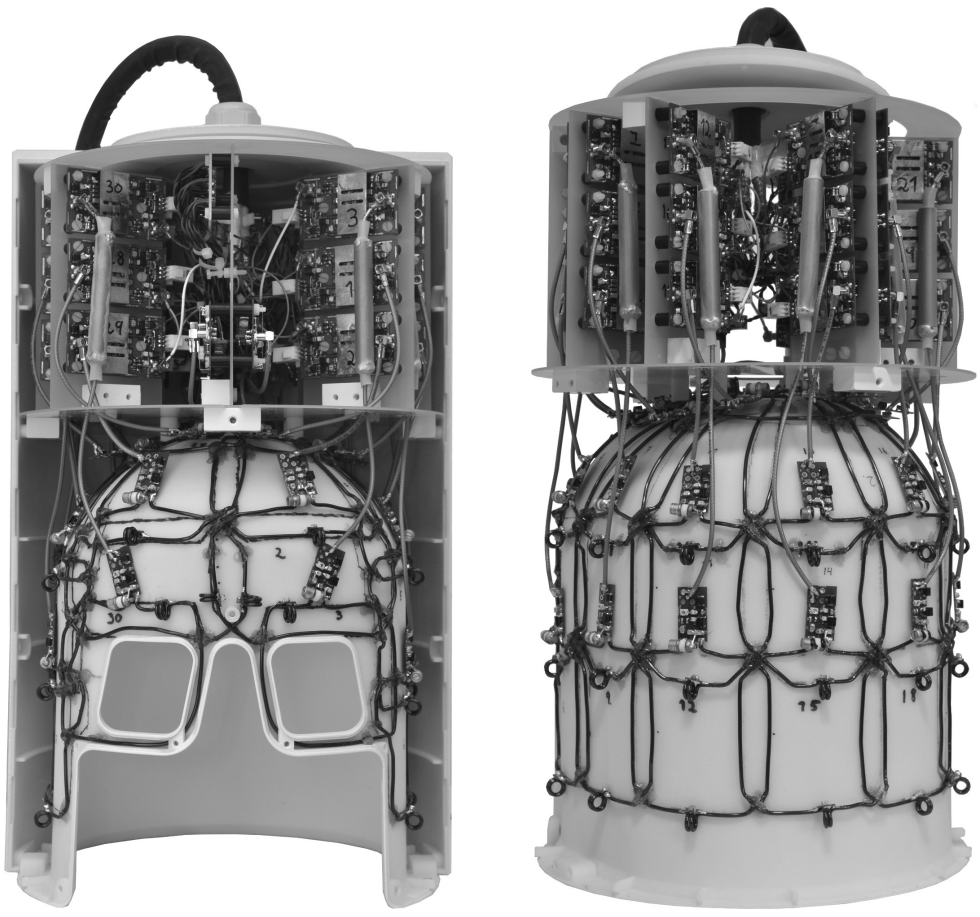

(a) *(b)*

Figure 4.1: Images of the head coil where (a) is the front and (b) is the back.

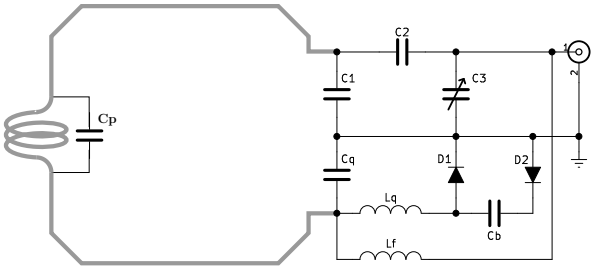

Figure 4.2: Matching circuit of the brain coil. (Component values: C1 ≈ 79-126 pF, C2 ≈ 9-15 pF, C3 = 8-30/1-8 pF, Cp ≈ 56-75 pF, Cq = 445 pF, Lq = 49 nH, Cb = 1000 pF).

anterior part of the coil (Fig. 4.1a) is made with overlapping coils (coils 1-6, 24-30). Whereas for the posterior part of the coil (Fig. 4.1b) only the horizontal and vertical coils are overlapped (e.g. coils 12 and 15 are overlapped, but 12 and 14 are non-overlapped). Hence, diagonal coils are non-overlapped. The idea is to maintain a proper size of the elements and thus pertain sample loading. Having the diagonal elements non-overlapped is not a problem because of very high preamplifier decoupling (in terms of matching and sensitivity profile at least). Two coils are also placed on the top of the head. Each coil element is connected with a coaxial cable to the preamplifiers mounted in the top part of the housing. The coil elements which are placed in the bottom of the housing are connected to the preamplifiers in the top of the housing and thus requires a proton cable trap (Bazooka type used).

4.1.2 Bench Characterization

The brain coil is designed for a GE MR750 scanner and uses a P-port. A custom made P-port emulator box was used to connect the coils on the bench. The P-port emulator provides power for the preamplifiers (10 V), the Q-spoiling signal (150 mA), and coaxial RF connectors for each coil.

The proton filters are the first to be adjusted. See Fig. 4.2. This was achieved by shorting the coil elements and measuring the S_{21} between two decoupled small loop probes, with an isolation of approximately -80 dB, in vicinity of the coil element. Next the Q-spoiling was adjusted by adding Cx, Lx, D1 and D2, and measuring the S_{21} between two small loop probes when a 150 mA current was supplied to the PIN diodes. Now, C1, C2, and C3 was added and the matching to 50 Ω adjusted and the unloaded to loaded Q-factor was assessed. Finally, the preamplifier decoupling was adjusted by C3, again measuring the S_{21} of two small loop probes. The preamplifier decoupling was measured with all other coil elements being Q-spoiled.

4.1.3 Image Acquisition and Reconstruction

The phantom used for imaging is a SAM head usually used for specific absorption rate (SAR) evaluations of cellular communication devices. It is filled with natural abundance ethylene glycol ($T_1 \approx 700$ ms) where 17 g/L NaCl was added to provide loading.

Flip angle calibration is conducted on the ethylene glycol by averaging over the entire phantom volume using a hard pulse by the Bloch-Siegert method [104].

Images were acquired using a CSI with a flip angle of 70 degrees, FOV of 36 cm by 36 cm, slice thickness of 20 mm, matrix size of 24 by 24, TR=1000 ms, spectral bandwidth of 5 kHz, and 1024 points. The TE was 9.3 ms with the brain coil. As a reference a head sized birdcage coil was also tested. However, the birdcage coil was tested with a TE=2.7 ms. The longer TE of the brain coil biases the SNR approximately 9 % in favour of the birdcage coil.

A noise reference measurement was acquired using a flip angle of 0 and a transmit gain of 0. The TR=1000 ms, spectral bandwidth was 5 kHz, with 1024 points.

To acquire quantitative SNR images the method described in depth in [105] is used. For the brain coil, smoothing is added as described in [106] and coil combination is done as described in [52].

4.2 Measured Results

The measured unloaded Q-factors where minimally 342 (coil 7) and maximally 406 (coil 31). The mean is 376 with a standard deviation of 12. The unloaded to loaded Q-factors range from 1.45 to 2.2. This large span is due to the diverging sizes of the elements. The Q-spoiling and proton filtering provides more than 45 dB of decoupling at the ^{13}C and ^{1}H frequencies, respectively. The preamplifier decoupling was measured to also exceed 45 dB for all elements.

In Fig. 4.3 the images acquired from the MRI experiments are shown. Fig. 4.3a and 3.11a shows SNR images of the brain and birdcage coil, respectively. The summed SNR is shown in Fig. 4.3c and 4.3d for the right-left (R-L) and anterior-posterior (A-P) orientations, respectively. It is seen that the SNR is lower in the center compared to the birdcage coil. The center SNR for the brain coil, taken for voxels spanning (R-L)=(11-14) to (A-P)=(11-14), is 22.3. The center SNR for the birdcage coil, taken for voxels spanning (R-L)=(11-14) to (A-P)=(9-12), is 42.6. Hence, the center SNR of the brain coil is decreased by approximately 47.7 % compared to the birdcage coil.

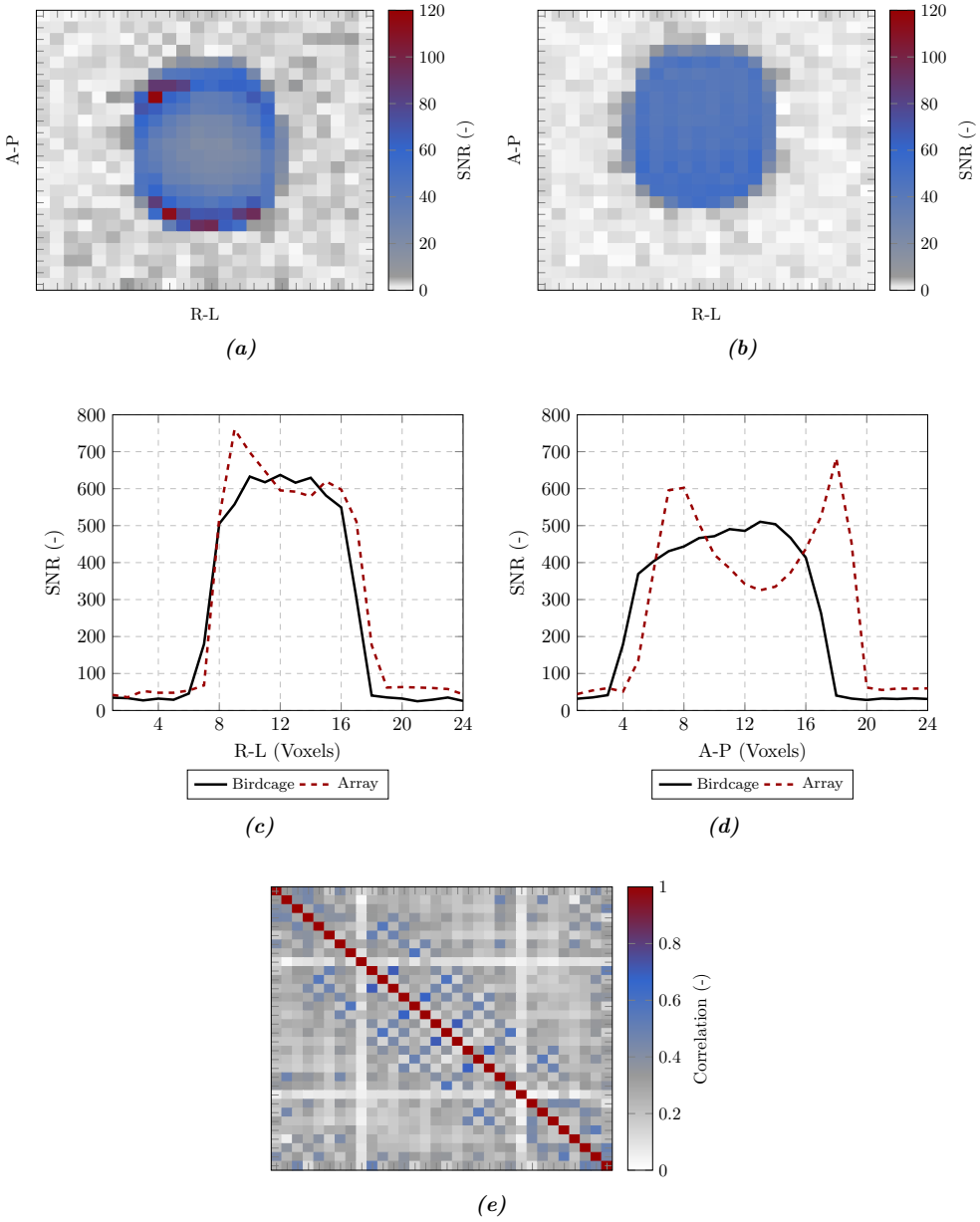

Figure 4.3: Measured performance of the 32 channel brain coil. (a) axial image using the 32 channel brain coil. (b) axial image using a clinical birdcage coil. (c) summed SNR in the right-left orientation. (d) summed SNR in the anterior-posterior orientation. (e) noise correlation matrix for the 32 channel brain coil.

The noise correlation matrix is shown in Fig. 4.3e. The mean noise correlation is 25.3 % with a standard deviation of 11.1 %. It is seen that e.g. coils 13 and 15 are highly correlated. This is because coils 11 and 17 act as noise sources which are coupled into coil 13 and 15. Hence, the noise added by the diagonal elements cause a noise correlation in the top and bottom coils. The mitigation of the noise coupling caused by the non-overlapped diagonal elements are discussed in the following section.

4.3 Noise Coupling

It is inevitable that the preamplifier generates noise. This noise, if not handled appropriately, can be a major source of SNR degradation. The problem of noise coupling principally arises when the coupling factor (k) between two coils is larger than zero. Hence, the larger the coupling factor, the more noise is coupled. Thus, the noise coupling is a bigger problem in non-overlapped and closely spaced coil topologies. Reducing the coupling factor to essentially zero can be achieved by overlapping, inductive decoupling, or capacitive decoupling. The prevalent method is overlapping. However, these methods are usually only practically applicable for the nearest neighbours. In most coil arrays the next nearest neighbours are relatively far from each other causing a low coupling factor. Preamplifier decoupling is the prevalent method of decoupling next nearest neighbours. However, a crucial aspect of preamplifier decoupling is that noise is not decoupled. Indeed, unique sensitivity profiles follow from using preamplifier decoupling. Noise, however, is not mitigated. Hence, in the case of non-overlapping elements (as is the case for the brain coil) the concept of noise coupling is vital.

To analyze the noise coupling from the preamplifiers a two channel array is investigated as seen in Fig. 4.4. The inductor L_1 and L_2 have an inductance of 170 nH with a Q-factor of 180. C_1, C_2, and C_3 match L_1 to 50 Ω. Likewise, C_4, C_5, and C_6 match L_2 to 50 Ω. The noise of the preamplifiers are characterized by their noise

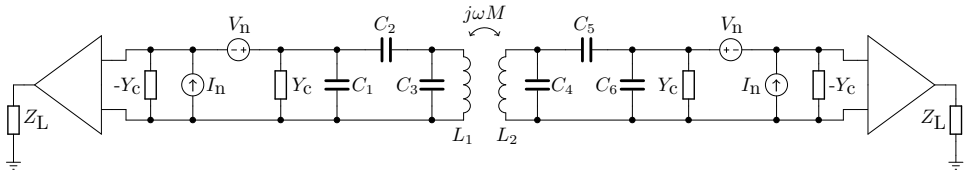

Figure 4.4: Schematic of a 2 channel coil setup used for analyzing noise coupling of the noise generated by the preamplifiers.

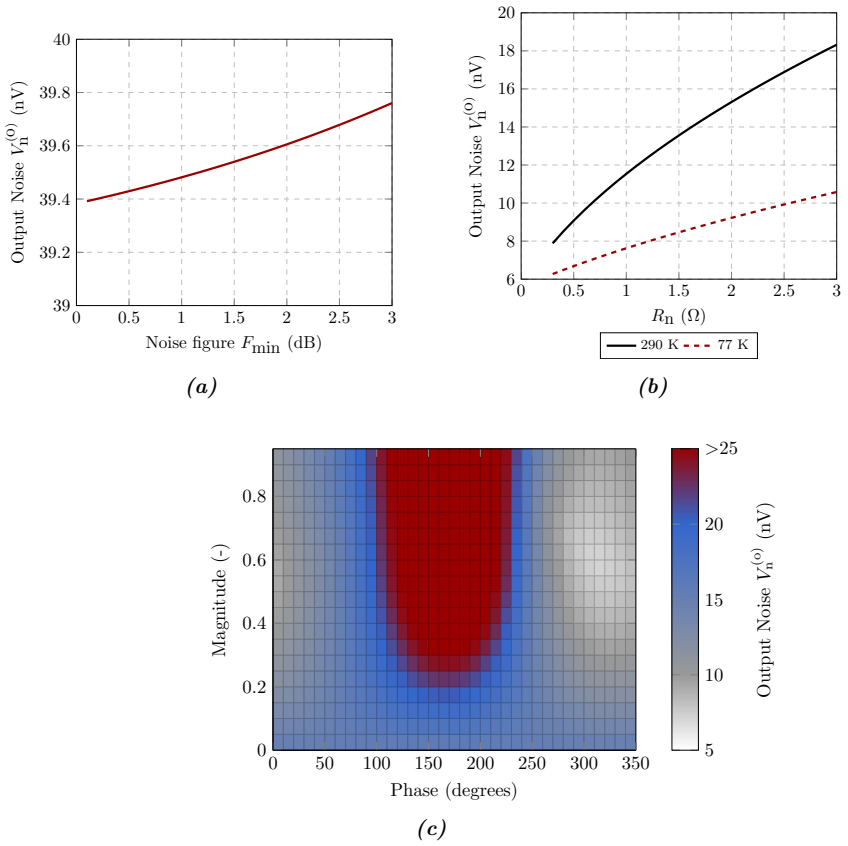

Figure 4.5: Simulated noise voltage on the output of the preamplifier in a non-overlapped 2 channel array. Noise is shown as a function of (a) minimum noise figure of the preamplifier, (b) equivalent noise resistance for both a room temperature and cryogenic preamplifier, and (c) the optimal noise impedance of the preamplifier in magnitude and phase.

voltage V_n, noise current I_n, and the correlation admittance Y_c. The preamplifiers are characterized by an input impedance of 0.1 Ω with an inductance of 600 nH. Further, the gain $S_{21} = 3 - j11$, isolation $S_{12} = 0$, and output impedance $S_{22} = 0$.

Before considering simulations of the system in Fig. 4.4, it is considered from a qualitative point of view. Given a coupling coefficient of zero, $j\omega M = j\omega k\sqrt{L_1 L_2} = 0$, results in a coupled noise that is likewise zero. Another aspect is that given a zero input impedance of the preamplifier the contribution to the coupled noise by the noise current becomes zero. Hence, only the noise voltage from the preamplifier is coupled. Now, if the coil is matched to an infinite impedance, the voltage noise is also eliminated. However, designing a preamplifier to exhibit constant V_n and I_n while changing the input impedance requires custom designed transistors, as this is not possible via

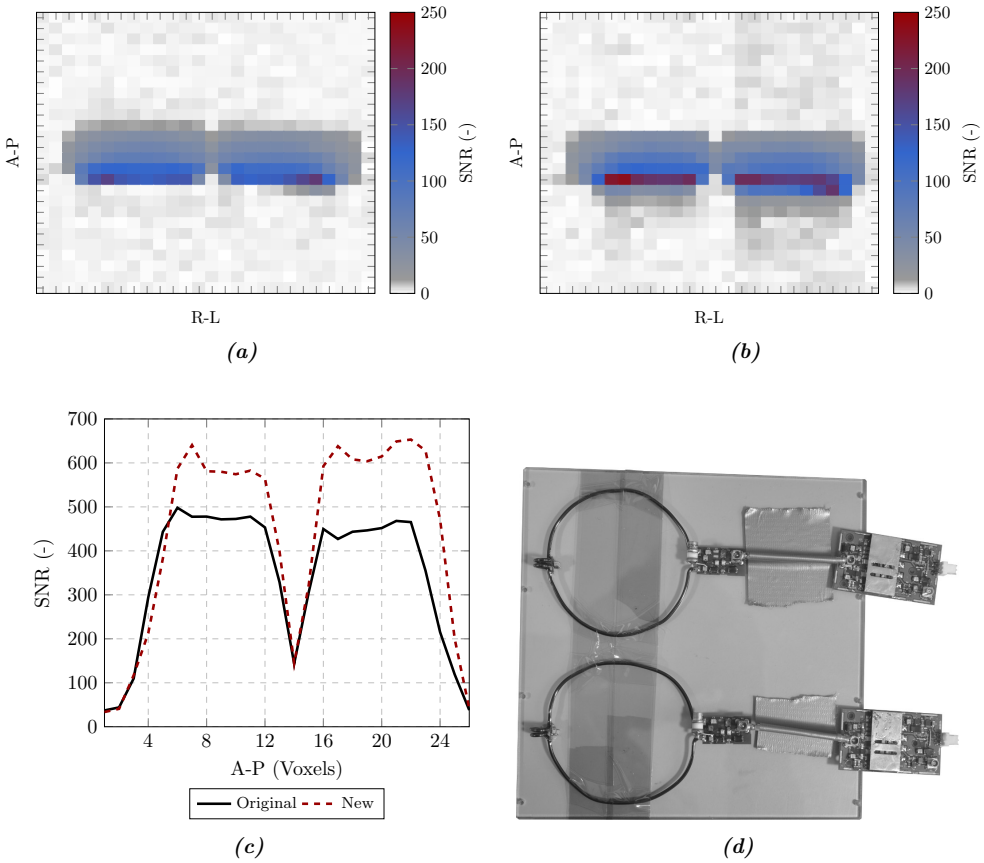

Figure 4.6: (a) and (b) shows measured axial SNR when using the first and second preamplifier designs, respectively. (c) summed SNR in the anterior-posterior orientation. (d) image of the the 2 channel prototype coil (with the first preamplifier design).

two-port theory. Thus, if the design of the preamplifiers is limited to the matching of the transistor, achieving a zero input impedance (by using e.g. a 50 Ω transmission line) simply transforms the noise current into voltage current (and vice-versa if an infinite input impedance was designed for). Importantly, is however that, the noise figure (the noise power) remains constant.

Rather than using broadband impedance matching (looking into the matching network), another approach for minimizing the coupled noise is investigated in this work. The alternative approach is to design the preamplifier such that the noise voltage, noise current, and correlation admittance are optimal. Now, this is easier understood by using the RF noise parameters of the preamplifier. These parameters are the minimal noise figure F_{min}, equivalent noise resistance R_{n}, and optimal noise match Γ_{opt}.

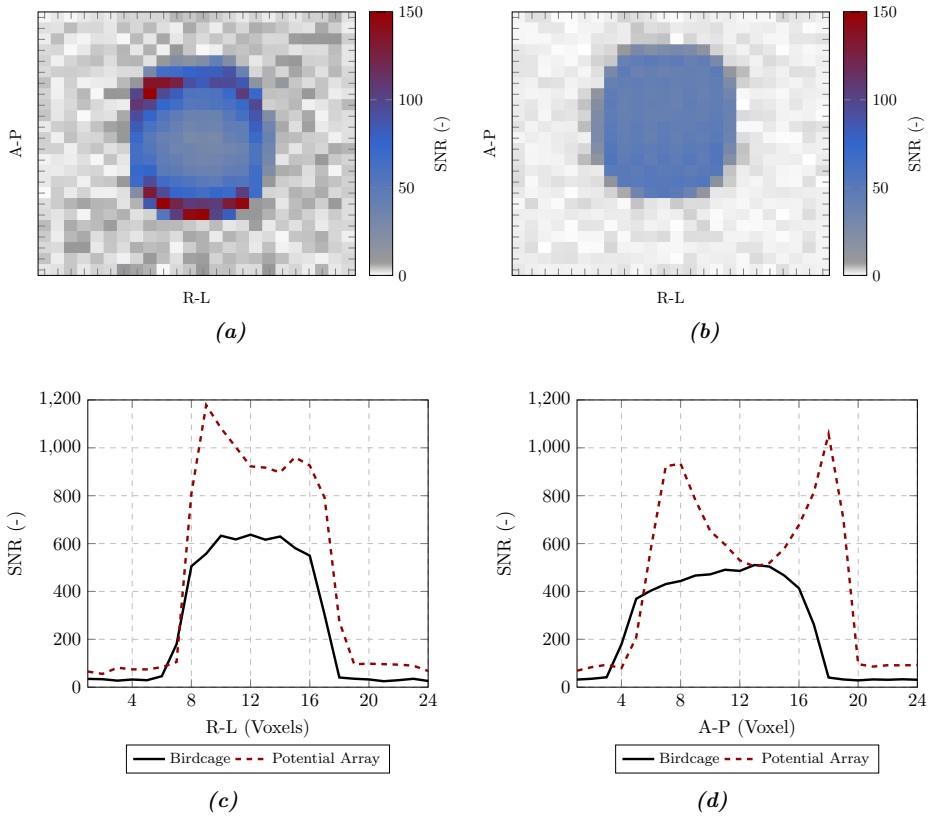

Figure 4.7: Potential SNR of the brain coil if preamplifier design 2 is used instead of design 1. (a) and (b) shows the potential SNR of the brain coil and birdcage coil, respectively. (c) and (d) shows the summed SNR for the R-L and A-P orientations, respectively.

As described in Section 2.1 the RF parameters can be converted into the circuit level parameters.

Simulations of the noise voltage in the output of the preamplifiers in the two channel array is seen in Fig. 4.5. First, the dependence of the output noise, $V_{\mathrm{n}}^{(\mathrm{o})}$, on the minimum noise figure is examined in Fig. 4.5a. The equivalent noise resistance is constant and equal to 25 Ω, and the optimal noise match is 50 Ω. As seen, the noise output hardly increases even when the minimum noise figure rises from 0.1 dB to 3 dB. This indicates that the noise figure is a poor measure for the noise generated by the preamplifiers in an array. However, examining the noise output as a function of the equivalent noise resistance in Fig. 4.5b highlights the importance of this metric. Here the output noise decreases by a significant amount, both for room temperature and cryogenic operation. Hence, the equivalent noise resistance may be a better

metric for understanding the noise generated by the preamplifiers in an array. In Fig. 4.5c the output noise is plotted as a function of the magnitude and phase of the optimal noise match of the preamplifier. Interestingly, at below 0.1 magnitude (close to 50 Ω) the output noise is fairly constant. However, at higher magnitudes the phase becomes important. Also, as the magnitude increases towards unity the output noise increases. The optimal noise match is, in this case, found at $0.6\angle 310°$ where $V_{\mathrm{n}}^{(\mathrm{o})} = 6.99$ nV. In 50 Ω, $V_{\mathrm{n}}^{(\mathrm{o})} = 15.3$ nV. Hence, by changing the optimal noise match, while $R_{\mathrm{n}} = 2\ \Omega$ and $F_{\mathrm{min}} = 0.2$ dB are constant, a potential decrease in output noise voltage is approximately 54 % which amounts to an increase in SNR of approximately 36 %.

As a proof-of-concept a two channel array is constructed and characterized in an MRI scanner. For this proof-of-concept, preamplifier design 1 is compared to preamplifier design 2. The array is seen in Fig. 4.6d. The coils are 10 cm in diameter and uses the same matching circuit as the brain coil (Fig. 4.2). Images were acquired from a GE MR750 using the same sequence as in the brain coil only with the FOV and matrix size changed to 26 cm by 26 cm and 26 by 26 voxels, respectively. The images are seen in Fig. 4.6a and 4.6b. As expected, using preamplifier design 2 yields an increased SNR. Further quantification is done by the summed SNR in the A-P orientation in Fig. 4.6c. The mean SNR of preamplifier design 1 and 2, in voxels 16 to 23, is 438 and 623 respectively. This yields an SNR increase of 42 % by using preamplifier design 2 rather than design 1. Extending this to the brain coil the potential SNR increase is plotted in Fig. 4.7. Now, the brain coil is apparently on par with the birdcage coil. However, the summed SNR is not a good measure for the center SNR. The center SNR is increased from 22.3 to 34.5 (by also correcting for the increased TE of the brain coil images compared to the birdcage coil). Hence, the center SNR remains impaired by approximately 19 % compared to the birdcage coil, even when using the preamplifiers minimizing the array noise. If preamplifier design 2 is cooled to 77 K the simulated SNR increase is approximately 11.3 % which yields a center SNR of 38.4 resulting in a center SNR impairment of 9.8 %. If instead the preamplifiers exhibited zero noise (cooled to 0 K), the SNR increase over preamplifier design 1 is 17.5 % and thus the center SNR impairment is 4.8 %. Hence, it is impossible by just changing the preamplifiers to achieve an SNR equal to that of the birdcage coil, even if using cryogenic preamplifiers.

4.4 Discussion

The construction of array coils for lower frequencies poses an issue by attaining a sufficient sample loading. The relatively low sample loading of the coil elements between 1.45 and 2.2 indicates that upwards of 70 % of the noise in the coil elements comes from the electronics. One aspect of the low sample loading is that the housing is relatively large for the SAM phantom. The distance from the ears to the housing is approximately 1-2 cm on each side. Also, the coil elements could be made larger by applying overlap in all directions thus increasing the sample loading and center SNR. The low sample loading also speaks in favour of using fully cryogenic arrays.

The choice of using a coil geometry where the diagonal elements are non-overlapped also has a severe SNR impact because of the noise coupling between preamplifiers. This is potentially mitigated by using PD2 instead of PD1, which in a two channel prototype coil increases the SNR by approximately 40 %.

An approach to mitigate the noise of the preamplifiers is to design a hybrid coil. A hybrid coil uses room temperature coils and matching, but cryogenic preamplifiers. Now, if the coil geometry is also designed to exhibit a tighter fit to the sample, a significant SNR increase is possible.

However, is it worth it to use (cryogenic) arrays compared to a birdcage coil? In terms of the potential SNR gain it is worth it, but there are many practical pitfalls which must be accounted for before the full SNR gain of cryogenic arrays can be realized.

4.5 Summary

In this chapter a 32 channel brain coil for ^{13}C imaging at 3 T was constructed and evaluated both on the bench and in the scanner using a SAM phantom. The measured SNR of the brain coil shows an approximate 48 % decrease compared to a clinical birdcage coil in the center of the phantom. This is in part due to noise coupled between preamplifiers because an array geometry where diagonal coils are non-overlapped and close spaced is used. A strategy to mitigate the noise coupled between preamplifiers was presented. A two channel prototype array showed a potential 42 % SNR increase by designing the preamplifiers. Extending this results to the brain coil limits the SNR decrease to 19 % compared to the birdcage coil (in the center of the phantom).

Closing 5

This chapter summarizes, discusses, and puts into perspective the thesis in terms of the research objectives stated in the introduction. Here, the larger picture is discussed and an outlook on the future is presented.

5.1 Discussion

Paraphrasing the first research objective, a fundamental focus of this work is to uncover the optimality principles of the preamplifiers when used in both single and array coils. The first attempts on designing preamplifiers where published in Paper E, which lead to the description of the dissociation of the optimal noise and input impedance of preamplifiers published in Paper A. At the time of publishing Paper A it was assumed that the optimal noise performance in an array would occur when the optimal noise figure of the preamplifier was equal to that of the matched coil impedance. Based on the results from Paper A, preamplifier design 1 (Section 2.2) was implemented. The assumption was, however, disproved in Section 4.3 where it was shown that the optimal noise reflection coefficient of the preamplifier has a non-zero magnitude and a unique phase for minimizing the noise coupling between coupled coils. This lead to the implementation of preamplifier design 2 in Section 2.3 which was proven to increase the SNR of a two channel prototype array by 42 % compared to preamplifier design 1. To further decrease the noise of the preamplifiers a cryogenic version of the first design was implemented based on Paper B. Hence, the first research objective has been thoroughly investigated by showing both optimal design for single and array coils.

The second research objective was to assess the feasibility of using volume coils for hyperpolarized magnetic resonance. This was primarily investigated in Chapter 3. The condition for cryogenic coils to be feasible is that the unloaded to loaded Q-factor is low. This is diametrically opposed to the conventional design strategy for designing coils which is to ensure a high sample loading such that the sample noise dominates the electrical noise. It was found that head sized birdcage coils exhibit high sample loading. The sample loading induce noise which cannot be removed by cooling. Hence, the potential SNR gain from cooling a head sized birdcage was below 2 %, thus, not feasible. However, the application of small animal imaging was then investigated because the smaller birdcage showed a very low sample loading and a

potential cryogenic SNR gain of upwards of 9 times. Hence, a cryogenic birdcage coil for small animal imaging was constructed and measured. The potential SNR of the cryogenic birdcage coil when combined with a cryogenic RF front end, is 2.4 times over an equal sized room temperature birdcage coil. However, only 43 % SNR gain was realized, probably due to a capacitor breaking during scanning. A 'magic number' of SNR gain for cryogenic coils is 2 times where researchers/clinicians will consider to use a cryogenic coil over a room temperature coil. This 'magic number' arises because of the practical and reliability difficulties in using cryogenic coils. In brief, it is feasible to use cryogenic volume coils for smaller sample sizes, if the potential SNR gain can be delivered upon. This requires the need for more reliable cryogenic components.

The third research question concerns the translation of hyperpolarized magnetic resonance into clinical practice. This requires coils that can be approved for clinical usage. The 32 channel brain coil presented in Chapter 4 was designed to be compliant with clinical requirements. However, the SNR in the center of a SAM phantom was approximately 47 % lower than a birdcage coil for similar usage. The SNR decrease is potentially mitigated to 19 % by using preamplifier design 2 rather than preamplifier design 1 in the coil. It however raises a question about the feasibility of high channel count array coils. Using fewer elements will increase center SNR but at the cost of parallel imaging performance. Seeing that the need for parallel imaging for hyperpolarized magnetic resonance remains clouded, assessing the feasibility of using the brain coil rather than the birdcage coil is not immediately possible. However, because of the inherently low sample loading of the elements in the brain coil, cooling the coil should yield appreciable SNR gains and could thus prove to be feasible in terms of both SNR and parallel imaging performance.

5.2 Outlook

Measuring the noise parameters of highly mismatched preamplifiers using 50 Ω noise meters entail an uncertainty which makes it impossible to accurately determine the parameters. Because the noise figure in 50 Ω is more or less useless in coupled array coils the impossibility of characterizing the noise parameters are crippling for further research. In this work, simulated parameters have been used, and showed decent predictions. It should be a high priority to find a better and more accurate method of determining the noise parameters of highly mismatched preamplifiers. One method could be to use a tuned coil and measure SNR directly using a spectrum analyzer by inducing known noise and signal. Hence, the reference temperature can be lowered

significantly and thus a better resolution of the measure noise figure at different source impedances (at least four to determine the noise parameters) might yield higher accuracy.

A prototype cryostat and cryogenic birdcage coil was developed. However, for practical use a cryostat such as presented in [92] is better suited for clinical use. It entails a higher price tag, and slightly higher temperature of the coil. However, it would prove to implement a cryogenic volume coil for small animal imaging. If a volume coil is required due to coverage it would almost certainly prove to be better from an SNR perspective to use an array. However, this also entails some practical challenges. The primary challenge is reliability of the coils. Using MICA capacitors have proven to be remarkably stable for cryogenic operation. However, no scientific studies have been conducted to properly quantify the reliability of different capacitor types and vendors.

In terms of human sized coils, it is expected that a hybrid array coil would be able to show equal SNR to that of a birdcage coil while enabling parallel imaging. A hybrid coil would use tightly fitted room temperature coils with cryogenic preamplifiers. Furthermore, obtaining approval for human clinical trials might be easier for a hybrid coil compared to a fully cryogenic coil. Now, a fully cryogenic coil array is expected to outperform the birdcage coil in terms of SNR and enabling parallel imaging. The cryostat could be based upon [92], but there are many practical limitation which have yet to be scientifically investigated. The practical challenges speak in favour of using a conventional room temperature birdcage coil for human imaging. However, if the birdcage is accepted as the best, all research and development more or less stops because of the inevitable high sample loading. Hence, the potential of cryogenic array coils remain a light at the end of a noisy tunnel. Principally, hyperpolarization is needed only because the hardware has not yet achieved sufficiently low noise performance. And when/if unity polarization by dDNP is shown, the SNR is still insufficient. Also, the transient nature of the hyperpolarized signal calls for parallel imaging. Hence, the quest for the ultimate limit of detection in hyperpolarized magnetic resonance lies in implementing cryogenic coil arrays for clinical usage.

References

[1] Worldwide cancer statistics. [Online]. Available: https://www.cancerresearchuk.org/health-professional/cancer-statistics/worldwide-cancer

[2] B. Chastek, C. Harley, J. Kallich, L. Newcomer, C. J. Paoli, and A. H. Teitelbaum, "Health Care Costs for Patients With Cancer at the End of Life," *Journal of Oncology Practice*, vol. 8, no. 6S, pp. 75–80, 2012.

[3] B. Jönsson, T. Hofmarcher, P. Lindgren, P. Lindgren, and N. Wilking, "The cost and burden of cancer in the European Union 1995–2014," *European Journal of Cancer*, vol. 66, pp. 162–170, 2016.

[4] M. Siddiquia and S. Rajkumarb, "The High Cost of Cancer Drugs and What We Can Do About It," *Mayo Clin Proc.*, vol. 87, no. 10, pp. 935–943, 2012.

[5] How Much Cancer Costs. [Online]. Available: https://www.cancerresearchuk.org/health-professional/cancer-statistics/worldwide-cancer

[6] R. L. Siegel, K. D. Miller, and A. Jemal, "Cancer statistics, 2017," *CA: A Cancer Journal for Clinicians*, vol. 67, no. 1, pp. 7–30, 2017.

[7] Ny teknologi lyn-evaluerer kræftbehandling. [Online]. Available: https://ing.dk/artikel/ny-teknologi-lyn-evaluerer-kraeftbehandling-209530

[8] J. H. Ardenkjær-Larsen, B. Fridlund, A. Gram, G. Hansson, L. Hansson, M. H. Lerche, R. Servin, M. Thaning, and K. Golman, "Increase in signal-to-noise ratio of > 10,000 times in liquid-state NMR," *Proceedings of the National Academy of Sciences*, vol. 100, no. 18, pp. 10 158–10 163, 2003.

[9] R. E. Hurd, Y.-F. Yen, A. Chen, and J. H. Ardenkjaer-Larsen, "Hyperpolarized 13C metabolic imaging using dissolution dynamic nuclear polarization." *J. Magn. Reson. Imaging*, vol. 36, no. 6, pp. 1314–1328, dec 2012.

[10] S. E. Day, M. I. Kettunen, F. A. Gallagher, D.-E. Hu, M. Lerche, J. Wolber, K. Golman, J. H. Ardenkjaer-Larsen, and K. M. Brindle, "Detecting tumor response to treatment using hyperpolarized 13C magnetic resonance imaging and spectroscopy," *Nat. Med.*, vol. 13, no. 11, pp. 1382–1387, nov 2007.

[11] E. Y. Chekmenev, "MRI Hyperpolarization and Molecular Imaging," *Newsl. SNMMI*, vol. 7, no. 3, pp. 2–4, 2013.

[12] M. A. Schroeder, L. E. Cochlin, L. C. Heather, K. Clarke, G. K. Radda, and D. J. Tyler, "In vivo assessment of pyruvate dehydrogenase flux in the heart using hyperpolarized carbon-13 magnetic resonance," *Proceedings of the National Academy of Sciences*, vol. 105, no. 33, pp. 12 051–12 056, 2008.

[13] K. Golman, J. S. Petersson, P. Magnusson, E. Johansson, P. Åkeson, C.-M. Chai, G. Hansson, and S. Månsson, "Cardiac metabolism measured noninvasively by hyperpolarized 13C MRI," *Magnetic Resonance in Medicine*, vol. 59, no. 5, pp. 1005–1013, 2008.

[14] M. A. Schroeder, A. Z. Lau, A. Chen, K. Connelly, X. Hu, J. Barry, D. J. Tyler, K. Clarke, G. A. Wright, and C. H. Cunningham, "Hyperpolarized 13C Magnetic Resonance Imaging and Spectroscopy Uniquely Reveal Early and Late Onset Metabolic Changes in the Failing Heart," in *Proc. Intl. Soc. Mag. Reson. Med. 19*, 2011.

[15] R. E. Hurd, Y.-F. Yen, D. Mayer, A. Chen, D. Wilson, S. Kohler, R. Bok, D. Vigneron, J. Kurhanewicz, J. Tropp, D. Spielman, and A. Pfefferbaum, "Metabolic imaging in the anesthetized rat brain using hyperpolarized [1-13C] pyruvate and [1-13C] ethyl pyruvate," *Magnetic Resonance in Medicine*, vol. 63, no. 5, pp. 1137–1143, 2010.
[16] D. Soon, D. Tozer, D. Altmann, P. Tofts, and D. Miller, "Quantification of subtle blood-brain barrier disruption in non-enhancing lesions in multiple sclerosis: a study of disease and lesion subtypes," *Multiple Sclerosis Journal*, vol. 13, no. 7, pp. 884–894, 2007.
[17] D. G. Nishimura, *Principles of Magnetic Resonance Imaging*, 1st ed. lulu.com, 2010.
[18] C.-N. Chen and D. I. Hoult, *Biomedical Magnetic Resonance Technology*, 1st ed. Institute of Physics Publishing, 1989.
[19] A. W. Overhauser, "Polarization of Nuclei in Metals," *Phys. Rev.*, vol. 92, pp. 411–415, Oct 1953.
[20] a. Abragam and M. Goldman, "Principles of dynamic nuclear polarisation," *Reports Prog. Phys.*, vol. 41, no. 3, pp. 395–467, Mar. 1978.
[21] K.-N. Hu, "Polarizing agents and mechanisms for high-field dynamic nuclear polarization of frozen dielectric solids," *Solid State Nucl. Magn. Reson.*, vol. 40, no. 2, pp. 31–41, sep 2011.
[22] K. R. Keshari and D. M. Wilson, "Chemistry and biochemistry of 13C hyperpolarized magnetic resonance using dynamic nuclear polarization," *Chem. Soc. Rev.*, vol. 43, pp. 1627–1659, 2014.
[23] S. Waiczies, J. M. Millward, L. Starke, P. R. Delgado, T. Huelnhagen, C. Prinz, D. Marek, D. Wecker, R. Wissmann, S. P. Koch, P. Boehm-Sturm, H. Waiczies, T. Niendorf, and A. Pohlmann, "Enhanced Fluorine-19 MRI Sensitivity using a Cryogenic Radiofrequency Probe: Technical Developments and Ex Vivo Demonstration in a Mouse Model of Neuroinflammation," *Sci. Rep.*, vol. 7, no. 1, p. 9808, 2017.
[24] C.-l. Lim, P. Serano, and J. L. Ackerman, "Pre-amplifiers for a 15-Tesla magnetic resonance imager," in *IEEE Int. RF Microw. Conf.*, 2013, pp. 295–299.
[25] S. H. Yadav, "Design of Low Noise Amplifier For MRI Scanner using Cascode Technology," *Int. J. Innov. Res. Comput. Commun. Eng.*, pp. 1504–1510, 2017.
[26] F. D. Doty, G. Entzminger, J. Kulkarni, K. Pamarthy, and J. P. Staab, "Radio frequency coil technology for small-animal MRI," *NMR Biomed.*, vol. 20, no. 3, pp. 304–325, 2007.
[27] *WMA32C: 32.19 MHz Low Noise Low Impedance Preamplifier*, WanTcom Inc., 2013, rev. B.
[28] Teledyne e2v (UK) Ltd. [Online]. Available: http://www.e2v.com/
[29] J. G. Heteren, N. Fenzi, T. W. James, and L. C. Bourne, "Thin Film High Temperature Superconductor RF Coil and Cryogenic Preamplifier for Low Field MRI," in *IEEE Nucl. Sci. Symp. Med. Imaging Conf.*, 1993, pp. 1708–1712.
[30] F. Resmer, H. C. Seton, and J. M. S. Hutchison, "Cryogenic receive coil and low noise preamplifier for MRI at 0.01 T," *J. Magn. Reson.*, vol. 203, pp. 57–65, 2010.
[31] P. Styles and N. F. Soffe, "A High-Resolution NMR Probe in Which the Coil and Preamplifier Are Cooled with Liquid Helium," *J. Magn. Reson.*, vol. 60, pp. 397–404, 1984.
[32] M. G. Richards, A. R. Andrews, C. P. Lusher, and J. Schratter, "Cryogenic GaAs FET amplifiers and their use in NMR detection," *Rev. Sci. Instrum.*, vol. 57, pp. 404–409, 1986.
[33] G. Fontana, R. Mezzena, S. Vitale, and M. Cerdonio, "Improved Sensitivity of Planar Microwave Biased RF-SQUIDs using a Cryogenic HEMT Preamplifier," *IEEE Trans. Appl. Supercond.*, vol. 3, no. 1, pp. 1820–1823, 1993.
[34] R. Mathur, R. W. Knepper, and P. B. O'Connor, "A Low-Noise Broadband Cryogenic

Preamplifier Operated in a High-Field Superconducting Magnet," *IEEE Trans. Appl. Supercond.*, vol. 18, no. 4, pp. 1781–1789, 2008.

[35] J. D. Sanchez-heredia, E. Søvsø, S. Hansen, C. Laustsen, V. Zhurbenko, and J. H. Ardenkjær-larsen, "Low-Noise Active Decoupling Circuit and its Application to 13C Cryogenic RF Coils at 3 T," *Tomography*, vol. 3, no. 1, pp. 60–66, 2017.

[36] J. D. Sánchez-Heredia, E. Søvsø, S. Hansen, C. Laustsen, V. Zhurbenko, and J. H. Ardenkjær-Larsen, "Decoupling Scheme for a Cryogenic Rx-Only RF Coil for 13C Imaging at 3T," in *Proc. Intl. Soc. Mag. Reson. Med. 25*, 2017.

[37] B. Hu, G. Varma, C. Randell, S. F. Keevil, T. Schaeffter, and P. Glover, "A novel receive-only liquid nitrogen (LN_2)-cooled rf coil for high-resolution in vivo imaging on a 3-tesla whole-body scanner," *IEEE Transactions on Instrumentation and Measurement*, vol. 61, no. 1, pp. 129–139, Jan 2012.

[38] I.-T. Lin, H.-C. Yang, and J.-H. Chen, "A Temperature-Stable Cryo-System for High-Temperature Superconducting MR In-Vivo Imaging," in *PloS one*, 2013.

[39] M. R. Kamel, L. M. Xie, L. Xue, J. Wosik, K. Nesteruk, K. Bockhorst, and P. A. Narayana, "Very High SNR Superconducting Receive-only 7 Tesla Coil for Rat Brain Imaging," in *Proc. Intl. Soc. Mag. Reson. Med. 15*, 2007.

[40] J. Wosik, L. Xue, L.-M. Xie, M. R. Kamel, K. Nesteruk, and J. A. Bankson, "Superconducting array for high-field magnetic resonance imaging," *Applied Physics Letters*, vol. 91, no. 18, p. 183503, 2007.

[41] J. Wosik, M. R. Kamel, L.-M. Xie, L. Xue, K. Nesteruk, A. C. Wright, and F. W. Wehrli, "HTS surface coil for MRI of the patella," in *Proc. Intl. Soc. Mag. Reson. Med. 15*, 2007.

[42] J.-C. Ginefri, M. Poirier-Quinot, O. Girard, and L. Darrasse, "Technical aspects: Development, manufacture and installation of a cryo-cooled HTS coil system for high-resolution in-vivo imaging of the mouse at 1.5T," *Methods*, vol. 43, no. 1, pp. 54–67, 2007.

[43] Q. Ma, K. Chan, D. Kacher, E. Gao, M. Chow, K. Wong, H. Xu, E. Yang, G. Young, J. Miller, and F. Jolesz, "Superconducting rf coils for clinical mr imaging at low field," *Acad. Radiol.*, vol. 10, no. 9, pp. 978–987, 2003.

[44] E. Gao and Q. Y. Ma, "A refined circuit model of high temperature superconducting spiral coils for MRI," *IEEE Tran. on Applied Superconductivity*, vol. 11, no. 1, pp. 403–406, March 2001.

[45] J. C. Nouls, M. G. Izenson, H. P. Greeley, and G. A. Johnson, "Design of a superconducting volume coil for magnetic resonance microscopy of the mouse brain," *Journal of Magnetic Resonance*, vol. 191, no. 2, pp. 231–238, 2008.

[46] S. Wei and W. Yang, "A high-temperature superconducting RF coil design for low field MRI," in *Asia-Pacific Intern. Symp. on Electromagnetic Compatibility (APEMC)*, vol. 1, May 2016, pp. 1093–1095.

[47] M. C. Cheng, B. P. Yan, K. H. Lee, Q. Y. Ma, and E. S. Yang, "A high temperature superconductor tape RF receiver coil for a low field magnetic resonance imaging system," *Superconductor Science and Technology*, vol. 18, no. 8, p. 1100, 2005.

[48] J. Wosik, K. Nesteruk, M. R. Kamel, F. Ip, L. Xue, A. C. Wright, and F. W. Wehrli, "Cryogenic Varactor-Tuned 4-element Array and Cryostat for μ-MRI of Trabecular Bone in the Distal Tibia," in *Proc. Intl. Soc. Mag. Reson. Med. 16*, 2008.

[49] W. Myers, D. Slichter, M. Hatridge, S. Busch, M. Mößle, R. McDermott, A. Trabesinger, and J. Clarke, "Calculated signal-to-noise ratio of MRI detected with SQUIDs and Faraday detectors in fields from 10μT to 1.5T," *Journal of Magnetic Resonance*, vol. 186, no. 2, pp. 182–192, 2007.

[50] K. Huang, S. Liao, H. Yang, H. Chen, H. Horng, M. J. Chen, and S. Yang, "Low-Field Nuclear Magnetic Resonance and Magnetic Resonance Imaging Using a High-

T_cSQUID for Tumor Detection," *IEEE Tran. on Applied Superconductivity*, vol. 21, no. 3, pp. 461–464, Jun. 2011.

[51] J. Wosik, L.-M. Xie, K. Nesteruk, L. Xue, J. A. Bankson, and J. D. Hazle, "Superconducting single and phased-array probes for clinical and research MRI," *IEEE Trans. on Applied Superconductivity*, vol. 13, no. 2, pp. 1050–1055, Jun. 2003.

[52] P. B. Roemer, W. A. Edelstein, and C. E. Hayes, "The NMR Phased Array," *Soc. Magn. Reson. Med.*, vol. 225, pp. 192–225, 1990.

[53] M. A. Ohliger, A. K. Grant, and D. K. Sodickson, "Ultimate intrinsic signal-to-noise ratio for parallel MRI: Electromagnetic field considerations," *Magnetic Resonance in Medicine*, vol. 50, no. 5, pp. 1018–1030, 2003.

[54] F. Wiesinger, N. D. Zanche, and K. Pruessmann, "Approaching Ultimate SNR with Finite Coil Arrays," in *Proc. Intl. Soc. Mag. Reson. Med. 13*, 2005.

[55] M. V. Vaidya, D. K. Sodickson, and R. Lattanzi, "Approaching ultimate intrinsic SNR in a uniform spherical sample with finite arrays of loop coils," *Concepts in Magnetic Resonance Part B: Magnetic Resonance Engineering*, vol. 44, no. 3, pp. 53–65, 2014.

[56] H.-H. Lee, D. K. Sodickson, and R. Lattanzi, "An analytic expression for the ultimate intrinsic SNR in a uniform sphere," *Magnetic Resonance in Medicine*, vol. 80, no. 5, pp. 2256–2266, 2018.

[57] M. A. Ohliger and D. K. Sodickson, "An introduction to coil array design for parallel MRI," *NMR in Biomedicine*, vol. 19, no. 3, pp. 300–315, 2006.

[58] M. Weiger, K. P. Pruessmann, C. Leussler, P. Röschmann, and P. Boesiger, "Specific coil design for SENSE: A six-element cardiac array," *Magnetic Resonance in Medicine*, vol. 45, no. 3, pp. 495–504, 2001.

[59] R. Brown, Y. Wang, P. Spincemaille, and R. F. Lee, "On the noise correlation matrix for multiple radio frequency coils," *Magnetic Resonance in Medicine*, vol. 58, no. 2, pp. 218–224, 2007.

[60] B. Keil and L. L. Wald, "Massively parallel MRI detector arrays," *Journal of Magnetic Resonance*, vol. 229, pp. 75–89, 2013.

[61] T. Schäffter, P. Börnert, C. Leussler, I. C. Carlsen, and D. Leibfritz, "Fast 1H spectroscopic imaging using a multi-element head-coil array," *Magnetic Resonance in Medicine*, vol. 40, no. 2, pp. 185–193, 1998.

[62] J. R. Porter, S. M. Wright, and A. Reykowski, "A 16-element phased-array head coil," *Magnetic Resonance in Medicine*, vol. 40, no. 2, pp. 272–279, 1998.

[63] G. Wiggins, C. Triantafyllou, A. Potthast, A. Reykowski, M. Nittka, and L. Wald, "32-channel 3 Tesla receive-only phased-array head coil with soccer-ball element geometry," *Magnetic Resonance in Medicine*, vol. 56, no. 1, pp. 216–223, 2006.

[64] B. Keil, G. C. Wiggins, C. Triantafyllou, L. L. Wald, F. M. Meise, L. M. Schreiber, K. J. Klose, and J. T. Heverhagen, "A 20-channel receive-only mouse array coil for a 3 T clinical MRI system," *Magnetic Resonance in Medicine*, vol. 66, no. 2, pp. 582–593, 2011.

[65] B. Keil, J. N. Blau, S. Biber, P. Hoecht, V. Tountcheva, K. Setsompop, C. Triantafyllou, and L. L. Wald, "A 64-channel 3T array coil for accelerated brain MRI," *Magnetic Resonance in Medicine*, vol. 70, no. 1, pp. 248–258, 2013.

[66] P. H. Chan, K. Michael, and B. Anderson, "Diagonal-Arranged Quadrature Coil Arrays for 3D SENSE Imaging," in *Proc. Intl. Soc. Mag. Reson. Med. 11*, 2004.

[67] J.V.Hajnal, D.J.Larkman, and D. Herlihy, "An array that exploits phase for SENSE imaging," in *Proc. Intl. Soc. Mag. Reson. Med. 8*, 2000.

[68] Y.-H. Chu, Y.-C. Hsu, B. Keil, W.-J. Kuo, and F.-H. Lin, "A 32-Channel Head Coil Array with Circularly Symmetric Geometry for Accelerated Human Brain Imaging," *PLOS ONE*, vol. 11, no. 2, pp. 1–13, Feb. 2016.

[69] M. F. Mueller, M. Blaimer, F. Breuer, T. Lanz, A. Webb, M. Griswold, and P. Jakob,

"Double spiral array coil design for enhanced 3D parallel MRI at 1.5 Tesla," *Concepts in Magnetic Resonance Part B: Magnetic Resonance Engineering*, vol. 35B, no. 2, pp. 67–79, 2009.

[70] M. F. Mueller, T. Lanz, F. Breuer, M. A. Griswold, and P. M. Jakob, "Three-dimensional quadrature array coil elements for improved parallel magnetic resonance imaging performance at 1.5 Tesla," *Concepts in Magnetic Resonance Part A*, vol. 38A, no. 2, pp. 61–73, 2011.

[71] J. A. de Zwart, P. J. Ledden, P. Kellman, P. van Gelderen, and J. H. Duyn, "Design of a SENSE-optimized high-sensitivity MRI receive coil for brain imaging," *Magnetic Resonance in Medicine*, vol. 47, no. 6, pp. 1218–1227, 2002.

[72] P. J. Ledden, A. Mareyam, S. Wang, P. van Gelderen, , and J. Duyn, "32 Channel Receive-Only SENSE Array for Brain Imaging at 7T," in *Proc. Intl. Soc. Mag. Reson. Med. 15*, 2007.

[73] A. Mareyam, L. Carvajal, D. Xu, J. Gordon, I. Park, D. B. Vigneron, S. J. Nelson, J. P. Stockmann, B. Keil, and L. L. Wald, "31-Channel brain array for hyperpolarized 13C imaging at 3T," in *Proc. Intl. Soc. Mag. Reson. Med. 26*, 2017.

[74] A. Autry, J. W. Gordon, L. Carvajal, I. Park, D. Mammoli, H.-Y. Chen, S. Chang, Y. Li, D. Xu, D. Vigneron, and S. J. Nelson, "Comparison between 8- and 32-channel phased-array receive coils for in vivo hyperpolarized C-13 brain imaging," in *Proc. Intl. Soc. Mag. Reson. Med. 27*, 2018.

[75] A. Einstein, "Zur elektrodynamik bewegter körper," *Annalen der Physik*, vol. 322, no. 10, pp. 891–921, 1905.

[76] A. Kolmogoroff, *Grundbegriffe der Wahrscheinlichkeitsrechnung*, 1st ed. Springer, 1933.

[77] J. L. Doob, "The development of rigor in mathematical probability (1900-1950)," *The American Mathematical Monthly*, vol. 103, no. 7, pp. 586–595, 1996.

[78] N. H. Bingham, "Studies in the history of probability and statistics xlvi. measure into probability: From lebesgue to kolmogorov," *Biometrika*, vol. 87, no. 1, pp. 145–156, 2000.

[79] H. T. Friis, "Noise Figures of Radio Receivers," *Proc. IRE*, pp. 419–422, 1944.

[80] G. Gonzalez, *Microwave Transistor Amplifiers - Analysis and Design*, 2nd ed. Prentice Hall, 1997.

[81] D. M. Pozar, *Microwave Engineering*, 3rd ed. Wiley, 2005.

[82] D. Hoult and R. Richards, "The signal-to-noise ratio of the nuclear magnetic resonance experiment," *J. Magn. Reson.*, vol. 24, no. 1, pp. 71–85, 1976.

[83] D. I. Hoult and P. C. Lauterbur, "The sensitivity of the zeugmatographic experiment involving human samples," *J. Magn. Reson.*, vol. 34, no. 2, pp. 425–433, 1979.

[84] D. W. Alderman and D. M. Grant, "An efficient decoupler coil design which reduces heating in conductive samples in superconducting spectrometers," *Journal of Magnetic Resonance*, vol. 36, no. 3, pp. 447–451, 1979.

[85] C. V. Grant, Y. Yang, M. Glibowicka, C. H. Wu, S. H. Park, C. M. Deber, and S. J. Opella, "A Modified Alderman–Grant Coil makes possible an efficient cross-coil probe for high field solid-state NMR of lossy biological samples," *Journal of Magnetic Resonance*, vol. 201, no. 1, pp. 87–92, 2009.

[86] E. M. Purcell, "Helmholtz coils revisited," *American Journal of Physics*, vol. 57, no. 1, pp. 18–22, 1989.

[87] F. Doty, G. J. Entzminger, and C. Hauck, "Error-Tolerant RF Litz Coils for NMR/MRI," *Journal of Magnetic Resonance*, vol. 140, no. 1, pp. 17–31, 1999.

[88] F. Doty, G. J. Entzminger, C. Hauck, and J. Staab, "Practical Aspects of Birdcage Coils," *Journal of Magnetic Resonance*, vol. 138, no. 1, pp. 144–154, 1999.

[89] D. I. Hoult, "The principle of reciprocity in signal strength calculations—A mathe-

matical guide," *Concepts Magn. Reson.*, vol. 12, no. 4, pp. 173–187, 2000.
[90] R. K. Harris and R. E. Wasylishen, *RF Coils for MRI*, 1st ed. Wiley & Sons, 2012.
[91] J. Tropp, "The theory of the bird-cage resonator," *Journal of Magnetic Resonance*, vol. 82, no. 1, pp. 51–62, 1989.
[92] J. D. Sánchez-Heredia, D. H. Johansen, R. A. Baron, M. Schneider, G. Spörl, J. Wosik, V. Zhurbenko, and J. H. Ardenkjær-Larsen, "3-Fold SNR Enhancement of Small Animal ^{13}C MRI using a Cryogenically Cooled (88 K) RF Coil," in *Proc. Intl. Soc. Mag. Reson. Med. 27*, 2018.
[93] C. Guglielmetti, C. Najac, A. Didonna, A. Van der Linden, S. M. Ronen, and M. M. Chaumeil, "Hyperpolarized 13C MR metabolic imaging can detect neuroinflammation in vivo in a multiple sclerosis murine model," *Proc. Natl. Acad. Sci.*, vol. 114, no. 33, pp. 6982–6991, aug 2017.
[94] A. P. Lin, F. Shic, C. Enriquez, and B. D. Ross, "Reduced glutamate neurotransmission in patients with Alzheimer's disease–an in vivo 13C magnetic resonance spectroscopy study," *Magn. Reson. Mater. Physics, Biol. Med.*, vol. 16, no. 1, pp. 29–42, 2003.
[95] Z. Chen and C. Zhong, "Decoding Alzheimer's disease from perturbed cerebral glucose metabolism: Implications for diagnostic and therapeutic strategies," *Prog. Neurobiol.*, vol. 108, pp. 21–43, 2013.
[96] H. Sancheti, K. Kanamori, I. Patil, R. Díaz Brinton, B. D. Ross, and E. Cadenas, "Reversal of Metabolic Deficits by Lipoic Acid in a Triple Transgenic Mouse Model of Alzheimer's Disease: A 13C NMR Study," *J. Cereb. Blood Flow Metab.*, vol. 34, no. 2, pp. 288–296, Nov. 2014.
[97] S. G. Snowden, A. A. Ebshiana, A. Hye, Y. An, O. Pletnikova, R. O'Brien, J. Troncoso, C. Legido-Quigley, and M. Thambisetty, "Association between fatty acid metabolism in the brain and Alzheimer disease neuropathology and cognitive performance: A nontargeted metabolomic study," *PLOS Med.*, vol. 14, no. 3, p. e1002266, Mar. 2017.
[98] C. Chassain, G. Bielicki, J.-P. Donnat, J.-P. Renou, A. Eschalier, and F. Durif, "Cerebral glutamate metabolism in Parkinson's disease: an in vivo dynamic 13C NMS study in the rat," *Exp. Neurol.*, vol. 191, no. 2, pp. 276–284, 2005.
[99] B. de Celis Alonso, S. S. Hidalgo-Tobón, M. Menéndez-González, J. Salas-Pacheco, and O. Arias-Carrión, "Magnetic Resonance Techniques Applied to the Diagnosis and Treatment of Parkinson's Disease," *Front. Neurol.*, vol. 6, p. 146, 2015.
[100] P. Bagga, A. N. Chugani, and A. B. Patel, "Neuroprotective effects of caffeine in MPTP model of Parkinson's disease: A 13C NMR study," *Neurochem. Int.*, vol. 92, pp. 25–34, 2016.
[101] A. M. Al-radaideh and E. M. Rababah, "The role of magnetic resonance imaging in the diagnosis of Parkinson's disease: A review," *J. Clin. Imaging*, vol. 40, no. 5, pp. 987–996, 2016. [Online]. Available: http://dx.doi.org/10.1016/j.clinimag.2016.05.006
[102] I. Park, P. E. Z. Larson, M. L. Zierhut, S. Hu, R. Bok, T. Ozawa, J. Kurhanewicz, D. B. Vigneron, S. R. VandenBerg, C. D. James, and S. J. Nelson, "Hyperpolarized 13C magnetic resonance metabolic imaging: application to brain tumors," *Neuro. Oncol.*, vol. 12, no. 2, pp. 133–144, Feb. 2010. [Online]. Available: http://dx.doi.org/10.1093/neuonc/nop043
[103] V. Z. Miloushev, K. L. Granlund, R. Boltyanskiy, S. K. Lyashchenko, L. M. DeAngelis, I. K. Mellinghoff, C. W. Brennan, V. Tabar, T. J. Yang, A. I. Holodny, R. E. Sosa, Y. W. Guo, A. P. Chen, J. Tropp, F. Robb, and K. R. Keshari, "Metabolic Imaging of the Human Brain with Hyperpolarized 13C Pyruvate Demonstrates 13C Lactate Production in Brain Tumor Patients," *Cancer Res.*, vol. 78, no. 14, pp. 3755–3760, Jul. 2018.
[104] R. F. Schulte, L. Sacolick, M. H. Deppe, M. A. Janich, M. Schwaiger, J. M. Wild, and F. Wiesinger, "Transmit gain calibration for nonproton MR using the Bloch–Siegert

shift," *NMR in Biomedicine*, vol. 24, no. 9, pp. 1068–1072, 2011.

[105] P. Kellman and E. R. McVeigh, "Image reconstruction in SNR units: A general method for SNR measurement," *Magnetic Resonance in Medicine*, vol. 54, no. 6, pp. 1439–1447, 2005.

[106] P. Perona and J. Malik, "Scale-space and edge detection using anisotropic diffusion," *IEEE Trans. on Pattern Analysis and Machine Intelligence*, vol. 12, no. 7, pp. 629–639, Jul. 1990.

Part II

Papers

Paper A

Association and Dissociation of Optimal Noise and Input Impedance for Low-Noise Amplifiers

D. H. Johansen, J. D. Sanches-Heredia, V. Zhurbenko, and J.H. Ardenkjær-Larsen

IEEE Transactions on Microwave Theories and Techniques, vol. 66, no. 12, pp. 5290-5299, Dec. 2018.

The layout has been revised.

Abstract

For magnetic resonance imaging (MRI) receive coil arrays, an ideal low-noise amplifier (LNA) is noise matched while exhibiting a high input reflection coefficient of unity or slightly higher. For this purpose, we present a design approach allowing to manipulate the optimal noise impedance and input impedance. The method is based on noise and S-parameters, hence, technology independent. As an example, the method is used to design an LNA for MRI receive coil arrays operating at 32.1 MHz. The design demonstrates the highest coil decoupling published so far of 54 dB. The measured noise figure of 0.44 dB is also better than other published designs. The measured gain is 22 dB with a 1-dB compression point of -14.5 dBm. The power consumption is 81 mW. We expect this method to enable better MRI receive coil array designs resulting in lower examination time and cost due to higher quality images.

A.1 Introduction

Low-noise amplifiers (LNAs) are used in a plethora of applications involving reception of small signals. In applications such as single surface or volume coils for magnetic resonance imaging (MRI), a classical noise matched (CNM) LNA is usually employed [1]. For wireless communications and nuclear magnetic resonance (NMR) spectroscopy probes, it is preferred to achieve a simultaneous noise and input match (SNIM). In the field of MRI receive coil arrays, a high input reflection coefficient, noise matched (HRNM) LNA is required [2]. Hence, within the field of magnetic resonance, three cases of LNA design are required: 1) SNIM for NMR spectroscopy probes, 2) CNM for MRI single/volume coils, and 3) HRNM for MRI coil arrays.

A general MRI system utilizes two orthogonal magnetic fields: A static field, called the main field, and a radio frequency (RF) field oscillating at the resonance frequency of the nuclei of interest (the Larmor frequency). The following description of magnetic resonance is very simplified. As a sample or a patient is placed in the main field, their nuclei become polarized (partially aligned with the main magnetic field). The RF field, if applied at the Larmor frequency, brings the nuclei out of equilibrium. When the RF field is turned off the nuclei precess back towards equilibrium producing an RF field at their Larmor frequency. Hence, the RF field is recorded by a receive coil and the signal is subsequently amplified by the LNA. The Larmor frequency is described by the product of the gyromagnetic ratio of the nuclei and the strength of the static magnetic field. Thus, the frequency of operation varies depending on

the nucleus of interest and the main field strength. An overview of the operating frequency of three nuclei, along with four common applications, is shown in Fig. A.1 in relation to the main field strength. The most commonly imaged nuclei is hydrogen (^{1}H), having a gyromagnetic ratio of approximately 42 MHz/T. Other nuclei, such as carbon-13 (^{13}C), exhibit a much lower gyromagnetic ratio. Hence, the operating frequency of an MRI system varies from a few MHz up to approximately one GHz. As a consequence, not only must the design method be applicable to the three cases, but also in a wide range of discrete frequencies. This is not the same as requiring a large bandwidth of the LNA, as the bandwidth in MRI is limited between approximately 50 kHz and 100 kHz, depending on static field strength, nucleus, and imaging pulse sequence used. [3, 4]

The method for obtaining SNIM is well described for a range of applications and is based on adding feedback to manipulate the relation between the optimal noise match and input impedance [5–10]. For narrowband applications, inductive source degeneration is often used in a common-source topology [11–14]. Series feedback offers the advantage of not degrading the noise performance of the LNA [15–17]. Parallel feedback techniques are often employed for wideband applications. In most cases, the optimal noise match is shifted by changing the amount of feedback [5, 18–20].

The CNM LNA is thoroughly described in many text books [21, 22], with the earliest description dating back to the 1960s [23, 24]. Classically, the input is noise matched to achieve the lowest noise, and the output is gain matched. The resulting input impedance may exhibit a high reflection coefficient, which may be unacceptable for some applications.

In the low frequency domain, HRNM LNAs are used in many instrumentation applications [25]. The design and review of low frequency HRNM LNAs is described

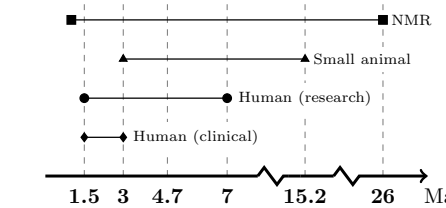

^{15}N	6.5	13	20	30	66	112	Frequency [MHz]
^{13}C	16	32	50	75	163	278	
^{1}H	64	128	200	298	647	1107	

Figure A.1: Overview of the main field and corresponding operating frequency of three commonly used nuclei when used for different MR applications.

in depth by [25]. Primary focus is on reducing flicker noise. Since flicker noise is not usually a problem in RF LNAs, much of this procedure is not very relevant at higher frequencies. In [26] a method primarily for SNIM is described. It is based on the same theory as this work. Hence, it could be used for HRNM designs. However, [26] assumes ideal reactive input and output circuits and also state that the case of negative input resistance is not considered. In the case of LNAs for MRI receive coil arrays, little has thus far been published. In [27], the authors describe a design which assumes that the input impedance of a field effect transistor (FET) is sufficiently high that an appropriately chosen inductor in the biasing of the transistor combined with a series capacitor yields acceptable input impedance and noise performance. However, neither the input impedance nor the noise performance is optimal. A 50 Ω transmission line equivalent circuit is placed in the input of the LNA to transform the input impedance to an acceptable value while the 50 Ω noise performance is constant.

This paper defines the entire range of design cases and describes a design method applicable for the cases described above. The method also works for intermittent steps between the cases of SNIM, CNM, and HRNM. These cases are dubbed design by association, equilibrium, and dissociation. The method uses S-parameters (generally, any set of linear parameters is sufficient as long as their transformation to S-parameters is well defined) and noise parameters, and is thus technology agnostic. Even though the method works for all cases, it is mostly relevant for designs by dissociation. This paper is, to the best of our knowledge, the first to propose a method for complete dissociation. Even stable negative input resistance is possible. Hence, this method can also be used for negative resistance/impedance converters [28–31]. Using the presented method, an LNA for a 32.1 MHz (^{13}C at 3 T) MRI receive coil array is implemented showing better decoupling, noise figure, and power consumption than other published LNA designs while maintaining acceptable gain and linearity performance.

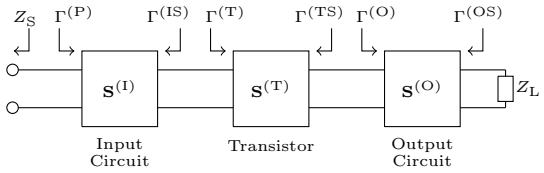

Figure A.2: Overview of the LNA which is divided into three two ports; input circuit, transistor and output circuit.

A.2 Definitions and Problem Formulation

The LNA is divided into three two-ports as seen in Fig. A.2. The input circuit, transistor, and output circuit are described by their corresponding S-parameter matrices, $\mathbf{S}^{(\mathrm{I})}$, $\mathbf{S}^{(\mathrm{T})}$, and $\mathbf{S}^{(\mathrm{O})}$, respectively. The terms impedance and reflection coefficient are used interchangeably since their conversions are well defined. To define the concepts of association, equilibrium, and dissociation the power wave reflection coefficient is used [32]. The equilibrium coefficient is defined as

$$\rho_{\mathrm{E}} = \left| \frac{Z_{50\Omega}^{(\mathrm{T})} - Z_{\mathrm{opt}}^{(\mathrm{T})^*}}{Z_{50\Omega}^{(\mathrm{T})} + Z_{\mathrm{opt}}^{(\mathrm{T})}} \right|, \tag{A.1}$$

where $Z_{50\Omega}^{(\mathrm{T})}$ is the input impedance of the transistor when it is loaded by 50 Ω. $Z_{\mathrm{opt}}^{(\mathrm{T})}$ is the optimal source impedance of the transistor that minimizes the noise figure. The asterix signifies the complex conjugate. The equilibrium coefficient is principally a figure of merit of the transistor describing the inherent mismatch between the optimal noise impedance and the input impedance of the transistor when terminated by 50 Ω. The noise-input impedance coefficient is defined as

$$\rho = \left| \frac{Z^{(\mathrm{P})} - Z_{\mathrm{opt}}^{(\mathrm{P})^*}}{Z^{(\mathrm{P})} + Z_{\mathrm{opt}}^{(\mathrm{P})}} \right|, \tag{A.2}$$

where $Z^{(\mathrm{P})}$ is the input impedance of the LNA and $Z_{\mathrm{opt}}^{(\mathrm{P})}$ is the optimal noise impedance at the input of the LNA. The noise-input impedance coefficient is a requirement specified by the designer and is thus defined at the input of the LNA. The design target for an LNA generally spans the region between the three cases:

1. **Association**, $\rho < \rho_{\mathrm{E}}$:
   Decreasing the mismatch between the optimal noise and input impedance. This also includes SNIM where the input impedance is equal to the complex conjugate of the optimal noise impedance, $Z_{\mathrm{P}} = Z_{\mathrm{opt}}^{(\mathrm{P})^*}$ resulting in $\rho = 0$.

2. **Equilibrium**, $\rho = \rho_{\mathrm{E}}$:
   When nothing is explicitly done to alter the mismatch between optimal noise and input impedance.

3. **Dissociation**, $\rho > \rho_{\mathrm{E}}$:
   When the mismatch of the optimal noise and input impedance is increased. In the case of LNAs for MRI receive coil arrays $\rho \approx 1$ as this maximizes the

potential decoupling between array elements.

The input reflection coefficient of the transistor and LNA are traditionally described as

$$\Gamma^{(\mathrm{T})} = S_{11}^{(\mathrm{T})} + \frac{S_{12}^{(\mathrm{T})} S_{21}^{(\mathrm{T})} \Gamma^{(\mathrm{O})}}{1 - S_{22}^{(\mathrm{T})} \Gamma^{(\mathrm{O})}}, \tag{A.3}$$

$$\Gamma^{(\mathrm{P})} = S_{11}^{(\mathrm{I})} + \frac{{S_{21}^{(\mathrm{I})}}^2 \Gamma^{(\mathrm{T})}}{1 - S_{22}^{(\mathrm{I})} \Gamma^{(\mathrm{T})}}, \tag{A.4}$$

respectively. Given a passive output circuit, the impedance looking into the output circuit towards the load is defined within the complex unit circle, $|\Gamma^{(\mathrm{O})}| \leq 1$. Because (A.3) and (A.4) constitute a Möbius Transformation, having the basic property of transforming a circle to a circle, $\Gamma^{(\mathrm{T})}$ and $\Gamma^{(\mathrm{P})}$ are also described by a circle [33]. This case arises when the reverse isolation and gain of the transistor is non-zero, $|S_{12}^{(\mathrm{T})}| > 0$ and $|S_{21}^{(\mathrm{T})}| > 0$. Hence, when feedback is present in the transistor, the input impedance of the transistor can be adjusted by the impedance of the output circuit.

If the gain of the transistor is high, the noise figure of the LNA can be assumed constant, regardless of loss in the output circuit (as long as the loss is lower than the gain of the transistor). The required $\Gamma^{(\mathrm{O})}$, when the input circuit and LNA input impedance are known, is given by

$$\Gamma^{(\mathrm{O})} = \frac{\Gamma^{(\mathrm{P})} - S_{11}^{(\mathrm{IT})}}{S_{22}^{(\mathrm{IT})} \left(\Gamma^{(\mathrm{P})} - S_{11}^{(\mathrm{IT})} \right) + S_{12}^{(\mathrm{IT})} S_{21}^{(\mathrm{IT})}}, \tag{A.5}$$

where superscripted (IT) indicates the combined S-parameters of the input circuit and transistor. Hence, given a certain input circuit and transistor configuration, (A.5) describes the required impedance of the output circuit looking towards the load. Using the circle equation, the input impedance can be plotted as a function of $\Gamma^{(\mathrm{O})}$ when a given input circuit and transistor is realized, as seen in Fig. A.3 (detailed in the next section). The main issue is that $\Gamma^{(\mathrm{O})}$ may become larger than unity, depending on the input circuit and transistor. In this work, only the inherent feedback present in the transistor is used. Hence, no additional feedback is added. The usage of feedback for LNA design is well described in other works (e.g. [8]). In terms of noise parameters, only the optimal noise impedance is directly manipulated in this work by the input circuit. The choice of biasing voltage/current of the transistor can have an enormous impact on all noise parameters which is also described in depth in other works (e.g. [21]). As mentioned, the main problem of (A.5) is choosing a proper input circuit

resulting in a realizable passive output circuit when a certain $\Gamma^{(\mathrm{P})}$ is required.

A.3 Design by Dissociation

This section presents the design strategy and exemplifies the implementation by designing an LNA for an MRI receive coil array. Since MRI LNAs are inherently narrowband, the design method is applied at a single frequency. A brief discussion of applying the design method for broadband applications is found in Appendix A. The design strategy is divided into six steps:

1. **Transistor selection:**
   Find an appropriate transistor by determining required optimal noise figure, reverse isolation, and gain. Plot (A.3) to confirm if desired degree of association or dissociation is possible. Determine the S-parameters of the transistor at a given bias and supply voltage.

2. **Match for optimal noise:**
   Design the input matching circuit such that the optimal noise figure impedance is transformed to the required impedance, $Z^{(\mathrm{IS})} = Z_{\mathrm{opt}}^{(\mathrm{T})}$. The required impedance can, principally, be anything but is normally 50 Ω. Furthermore, biasing and stability should be considered.

3. **Add series transmission line to input**:
   To ensure a passive output circuit, the input impedance circle determined by (A.3) and (A.4) needs to be transformed to cover the required input impedance. Adding a series transmission line, with characteristic impedance equal to the required optimal noise impedance, rotates the input impedance circle while the optimal noise match remains constant.

4. **Design output circuit**:
   First, determine $\Gamma^{(\mathrm{O})}$ such that $\Gamma^{(\mathrm{P})}$ results in the required input reflection coefficient by applying (A.5). Secondly, add loss to the output circuit to ensure stability. Also, investigate the frequency response to determine possible stability issues. Finally, the output circuit must also ensure that the output impedance of the preamplifier is matched to Z_{L}.

5. **Determine gain and linearity trade-off:**
   Since the gain and linearity of the LNA may be impaired by the choice of $\Gamma^{(\mathrm{O})}$ and length of the transmission line, iterate over steps 1) and 4) to determine the gain and linearity trade-off.

6. **Simplify input circuit**:
   Since the implementation of a transmission line may be inconvenient, especially at lower frequencies, a Pi- or T-network equivalent can be utilized. The input thus consists of a noise match and discrete transmission line equivalent which may entail high losses (due to undesirable values). The entire input circuit can be further simplified to either a T- or Pi-network using basic circuit theory.

Because the MRI array elements couple inductively, the impedance looking into the individual element's matching network should be large, particularly during reception, to limit their coupling [2, 34]. The coupling between elements degrades signal-to-noise ratio (SNR), making it difficult in practice to match all the elements, and increases noise correlation, which can be detrimental for parallel imaging. The combination of matching and decoupling circuits are described in [2, 35, 36].

The requirements for the LNA is an optimal noise match at 50 Ω with an inductive input impedance of approximately 360 nH. To ensure that the analog-to-digital converter of the MRI scanner is not saturated, the maximum allowable gain is 27 dB. Finally, the LNA needs to be output matched to 50 Ω. The primary target is to maximize the decoupling between elements, which requires a negative input resistance of -1.1 Ω to compensate for the loss in the matching circuit.

In this example, the selection of transistor is based primarily on two parameters: The rated noise figure and cryogenic operation capability (even though it is not used at cryogenic temperatures in this work). Further, the MRI system features only a positive voltage supply. Hence, it decreases the necessary auxiliary circuitry to use a transistor, which requires a positive bias voltage. To satisfy the requirements outlined above, the enhancement mode pseudormorphic high electron mobility tran-

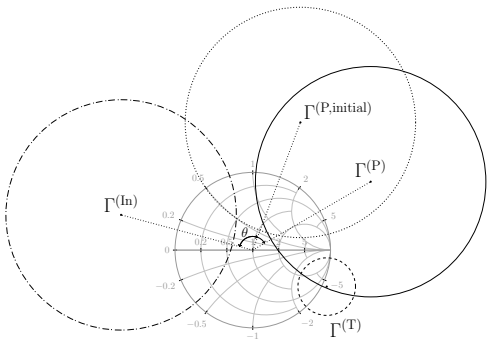

Figure A.3: Simulated transistor impedance circle (dashed), noise matched impedance circle (dash-dotted), initial input impedance (dotted), and final LNA input impedance circle (solid).

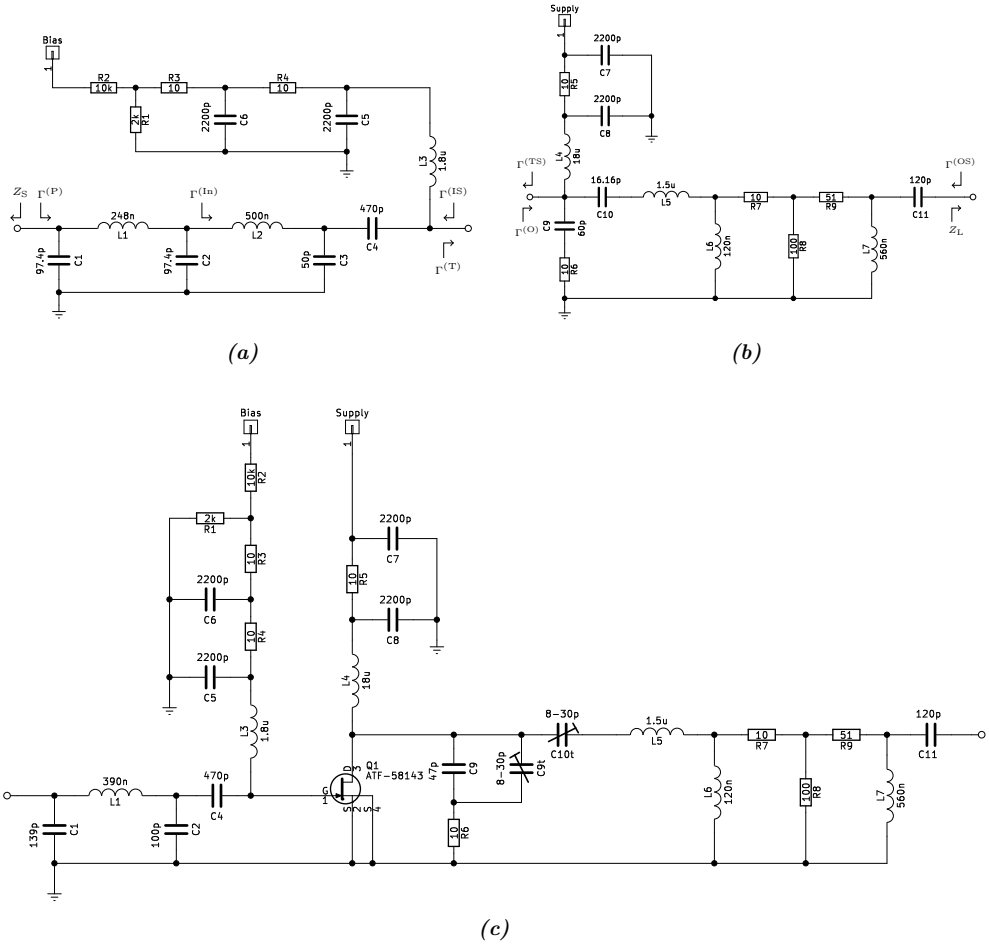

Figure A.4: Schematics used for the design and implementation of the LNA. (a) the input circuit used for analysis. The ideal transmission line is converted to a Pi-network (C1, C2 and L1). L2 and C3 perform optimal noise matching. (b) the output circuit used for analysis. R6 and C9 determine the degree of instability while C10 and L5 determine the resonance of the negative resistance. R7, R8 and R9 form an attenuator to control the gain of the LNA. C11 and L7 match the output of the LNA to 50 Ω. (c) the schematic of the implemented LNA. The input circuit has been further simplified by combining the series transmission line and noise matching components into a Pi-network (C1, C2 and L1). The output circuit is implemented using variable capacitors to control the degree of stability (C9t) and the notch where the input resistance becomes negative (C10t).

sistor Broadcom/Avago ATF58143 is chosen. It shows a minimum noise figure of 0.007 dB at 32.1 MHz (extracted from the transistor model) with a bias voltage of 0.5 V and a supply voltage of 3 V [37]. We chose to use the well-known common-

source topology for the design (with no inductive source degeneration). This further yields $Z_{11}^{(\mathrm{T})} = 7 - j632\ \Omega$ and an optimal noise impedance of $1403 + j729\ \Omega$. The equilibrium coefficient is $\rho_{\mathrm{E}} = 0.99$. The required input-noise coefficient is $\rho = 1.014$. Since $\rho > \rho_{\mathrm{E}}$, dissociation is required. Additionally, the flicker noise corner frequency, extracted from the transistor model, is 1 MHz. Hence, the design does not require methods for lowering flicker noise.

The transistor input circle $\Gamma^{(\mathrm{T})}$ is calculated using (A.3), (A.4), and the circle equation. Assuming a passive output circuit, the corresponding circle is seen in Fig. A.3 (dashed) with a center in $(0.95; -0.47)$ and radius of 0.37. This verifies that the transistor works for the degree of dissociation required.

The input circuit is shown in Fig. A.4a. The biasing inductor L3 together with C5, R4, and C6 constitute a low Q high pass filter, with a resonance at 1.8 MHz, ensuring low frequency stability. It was empirically discovered that if L1 is larger than approximately 2.2 uH instability occurs. L1 has a rated internal resistance of 1 Ω. The high pass filter exhibits an impedance at 32.1 MHz of $1.4 + j361\ \Omega$ adding noise corresponding to 0.027 dB. The final components in the feeding part of the input circuit are R1 and R2. They perform a voltage division such that the supply voltage of 3 V is decreased to approximately 0.5 V. R1 and R2 further ensure that the high pass filter is loaded with a high impedance. Hence, R1 and R2 buffers the feeding network such that the resonance of the high pass filter is not dependent on the network connected to the Bias pin.

The second part of the input circuit is the noise match. C4 is a DC block. C3 and L2 matches the optimal noise impedance to 50 Ω. The noise added by these three components is 0.011 dB. The resulting noise matched impedance is $Z^{(\mathrm{In})} = 0.4 - j12\ \Omega$ when the transistor is loaded with 50 Ω. The resulting noise matched input circle $\Gamma^{(\mathrm{In})}$ has its center in $(-1.7; 0.45)$ with radius 1.5. It is also plotted in Fig. A.3 (dash-dotted). This further yields the maximum dissociation $\rho_{\max} = 3.26$ and the minimum association $\rho_{\min} = 0.26$, which is realizable with a passive output circuit.

C1, L1 and C2 is the discrete equivalent of a transmission line with an electrical length of 47.7° and characteristic impedance of 50 Ω. The transmission line rotates the center of the noise matched circle $\Gamma^{(\mathrm{In})}$ to the corresponding angle of the required input impedance. The resulting LNA input circle $\Gamma^{(\mathrm{P,initial})}$, with center $(0.6; 1.6)$ and radius 1.5, is also seen in Fig. A.3 (dotted). The electrical length of the transmission line of 47.7° is used as the initial guess for starting the optimization procedure involving the determination of $\Gamma^{(\mathrm{O})}$, gain, and linearity of the LNA. The transmission line equivalent circuit adds another 0.033 dB noise. This yields a total noise of 0.071 dB. The transmission line length of 47.7° results in a required $Z^{(\mathrm{O})} = 210 + j24\ \Omega$. Through

theoretical and practical iterations, an acceptable trade-off between gain, linearity, and the simplicity and practicality of the output circuit resulted in a transmission line length of 67.5°. The resulting, and final, $\Gamma^{(\mathrm{P})}$ circle is shown in Fig. A.3 (solid) with center $(1.5; 0.9)$ and radius 1.5. Hence, $Z^{(\mathrm{O})} = 34 + j20\ \Omega$.

The output circuit is seen in Fig. A.4b and is made of four parts: Feed, matching for $Z^{(\mathrm{O})}$, a T-network attenuator, and matching to Z_{L}. The feed network consists of L4, C7, C8, and R5. L4 is the feed inductor. C7, C8, and R5 is a supply filter.

The matching for $Z^{(\mathrm{O})}$ is performed by C9, C10, L5, L6, and R6. R6 and C9 forms a low pass filter and ensures stability at higher frequencies. To be able to adjust $Z^{(\mathrm{O})}$, C9 is chosen such that, by varying its value, the input impedance of LNA can also be varied. C9 primarily influences the resistance of $Z^{(\mathrm{P})}$. C10 and L5 form a series resonance determining the bandwidth in which the LNA can exhibit a negative input resistance. When C10 and L5 is resonant they are simply shorted. However, slightly off resonance C10 and L5 ensure that the input impedance of LNA is not negative. This is to better control the stability due to a negative input resistance requirement. This creates a 'bump' in the frequency response of the input impedance where the negative resistance can occur, as will be shown later. Hence, by varying C9 and C10, the amount of negative input resistance and the frequency where the negative input resistance occurs can be controlled. L6 transforms the approximate 50 Ω impedance looking into R7 towards the load towards the required $Z^{(\mathrm{O})}$.

To comply with the required $Z^{(\mathrm{O})}$, while matching $Z^{(\mathrm{OS})}$ to 50 Ω, adding loss to the output circuit is required to create the desired isolation between the two ports. The loss is added by resistors R7, R8, and R9. The loss is approximately 10 dB. This yielded acceptable gain of the LNA and isolation such that C10 and C9 can be varied without changing $Z^{(\mathrm{OS})}$ significantly. The total added noise by the output circuit is 0.01 dB. Thus, the noise figure of the LNA is 0.081 dB.

L7 and C11 matches the output of the LNA to approximately 50 Ω. C11 also acts as a DC block, because, in some cases, a DC voltage will be supplied by the MRI system.

The final step in the design procedure is to simplify the input circuit. Since the input circuit also ensures stability at low frequencies this must still apply after simplification.

The implemented schematic is shown in Fig. A.4c. The input circuit is simplified by merging the noise matching components and transmission line into a single Pi-network (C1, C2, and L1). Variable capacitors are added to the output circuit to tune the output circuit's impedance accurately. Further, parasitic coupling between inductors L1, L3, L4, and L6 has been added to the model, in the order of -40 dB,

to properly simulate the impact of the layout on the performance of the LNA. This adds approximately 0.15 dB of noise and introduce changes to the input impedance. However, the input impedance is easily corrected by the variable capacitors C9t and C10t.

The implemented setup is shown in Fig. A.5. A coil with a diameter of 80 mm is used. Matching is done with a shunt-series topology as described in [36]. The matching circuit also incorporates active transmitter detuning to not distort the transmit field or damage the LNA. A cable trap is also implemented to attenuate common mode signals on the coaxial cables.

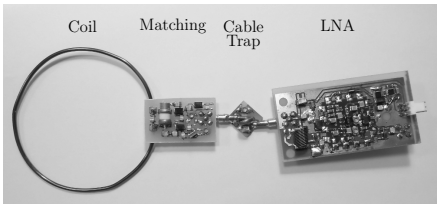

Figure A.5: Implemented setup. From left to right; MRI surface coil, matching and decoupling circuit, cable trap, and LNA. The diameter of the surface coil is 80 mm.

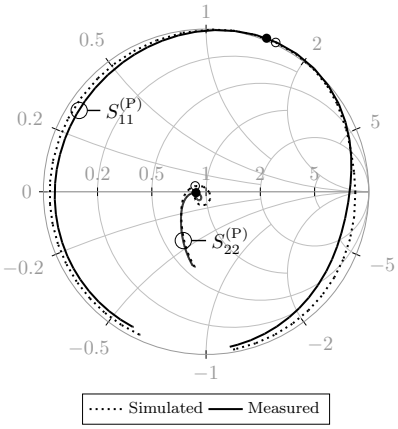

Figure A.6: Simulated and measured input impedance and output impedance of the LNA. The negative resistance occurs from approximately 31 MHz to 33 MHz.

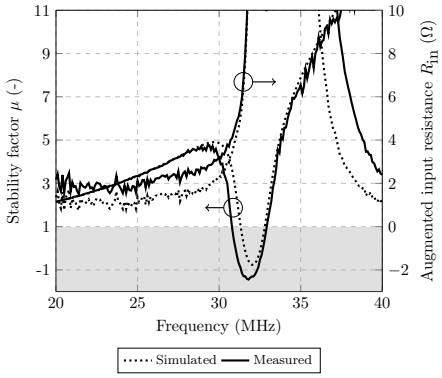

Figure A.7: Stability factor of the LNA is shown to the left. The input stability resistance is shown to the right. As the stability factor becomes smaller than one, the input stability resistance must be above zero for the LNA to be stable.

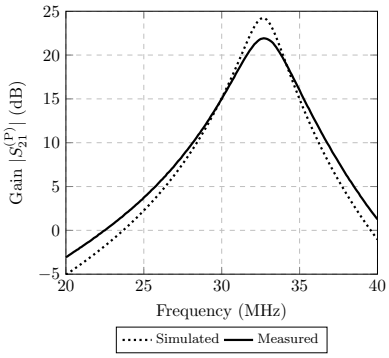

Figure A.8: Simulated and measured gain of the LNA.

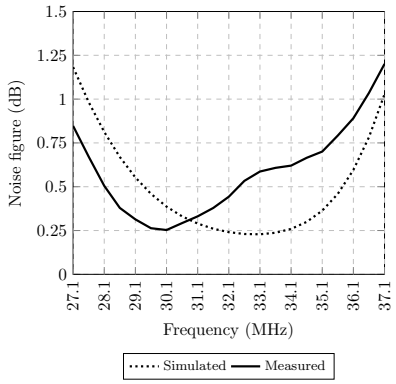

Figure A.9: Simulated and measured noise figure of the LNA.

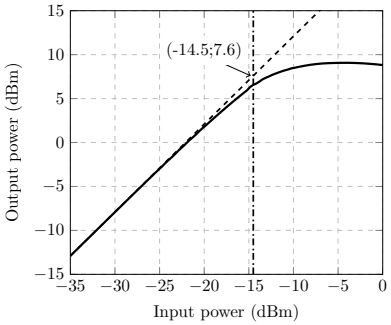

Figure A.10: Measured 1-dB compression point. The solid line is the measured response, the dashed line is the linear extrapolation from the low power gain, and the dash-dotted line signifies the 1-dB compression point.

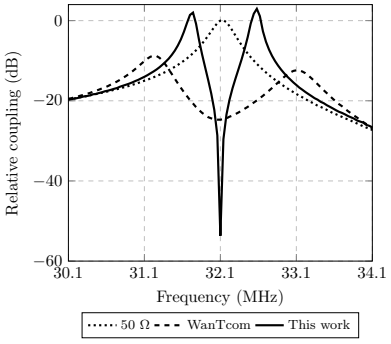

Figure A.11: Relative coupling when utilizing the implemented LNA compared to the WanTcom. The reference value is measured when the matching circuit is terminated by a 50 Ω load.

A.4 Results

The simulated and measured input and output impedance is seen in Fig. A.6. The output impedance exhibits a voltage standing wave ratio (VSWR) of less than 1.15 at 32.1 MHz for both simulated and measured results. The input impedance is $-1.1 + j73\ \Omega$ at 32.1 MHz, corresponding nicely to the required impedance. The input impedance was adjusted by the tuning capacitors C9t and C10t, such that maximum decoupling was achieved. The simulated input impedance is approximately $-1.1 + j78.5\ \Omega$. Overall, a good agreement between simulated and measured impedances is achieved.

To analyze the stability of the LNA, the Edwards-Sinsky stability factor (μ) [38] is used, as opposed to the Rollet stability factor (K) [39]. This is because the Edwards-

Sinsky stability factor, for either the input or output, constitutes the necessary and sufficient condition for stability. The Rollet stability factor requires two equations to ensure stability [22, 39]. If the LNA is designed with a negative input resistance, unconditional stability is not achievable, and the total augmented resistance on the input and output should be larger than zero [21],

$$R_{\text{in}} = \text{Re}\left(Z_{\text{S}} + Z^{(\text{P})}\right) > 0, \tag{A.6}$$

$$R_{\text{out}} = \text{Re}\left(Z_{\text{L}} + Z^{(\text{OS})}\right) > 0, \tag{A.7}$$

where R_{in} is the augmented input resistance and R_{out} is the augmented output resistance. The measured and simulated augmented output resistance is above zero over the frequency range from 20 MHz to 40 MHz. At lower and higher frequencies the input impedance has a positive resistance which ensures the stability of the amplifier at these frequencies. The μ stability factor and augmented input resistance is plotted in Fig. A.7. In the range from approximately 31 MHz to 33 MHz the LNA is conditionally stable, while the LNA is unconditionally stable outside the 31 MHz to 33 MHz range. To justify the stability of the system, (A.6) is also examined, showing that with the given combination of coil and matching circuit the amplifier is indeed stable, since the augmented input resistance is positive. As an additional precaution, the spectrum was measured to check for oscillations - none was observed. Hence, the circuit is stable with the given combination of coil, matching circuit, and LNA.

The simulated and measured gain is seen in Fig. A.8. The simulated gain of the LNA is 23 dB, while the measured gain is 22 dB at 32.1 MHz. It is slightly higher than the LNA presented in [27], which showed no SNR degradation compared to the readily available WanTcom LNA. Thus, the gain is acceptable.

At 32.1 MHz the noise figure was simulated and measured at 0.24 dB and 0.44 dB respectively. The noise figure is plotted over frequency in Fig. A.9. The measured noise figure is slightly shifted in frequency. As will be discussed later, the noise figure lies within expected tolerances. In terms of linearity, the 1-dB compression point is measured at -14.5 dBm, shown in Fig. A.10. According to [40, 41], a 1-dB compression point better than -20 dBm is sufficient. Hence, the LNA complies with linearity requirements.

The implemented LNA draws 27 mA current, from a supply voltage of 3 V resulting in a power consumption $P^{(\text{P})} = 81$ mW. The supply voltage can be lowered to also lower the power consumption. A 1.5 V supply was attempted, however, the 1-dB compression point dropped below -20 dBm which is rather low.

The coupling between two identical array elements loaded with the designed LNAs is

shown in Fig. A.11 where it is compared to one of the few commercially available MRI LNAs for 32.1 MHz operation. The coupling is measured by the S_{21} using two loop probes of 1 cm diameter separated by 4 cm connected to a vector network analyzer, as described in [42–44]. The reference value is when the matching circuit is terminated by a 50 Ω load. The WanTcom achieves 25 dB decoupling while the LNA presented in this work achieves 54 dB of decoupling. The bandwidth of the decoupling is also decreased.

A.5 Discussion

A detailed analysis of the matching circuit is required to understand why a negative input resistance LNA yields optimal decoupling. It is excluded from detailed treatment here to keep the paper focussed on the design of such an LNA. In brief terms, however, the negative input resistance of the LNA negates losses in the matching network resulting in a higher Q-factor of the decoupling circuit.

Overall, a good agreement has been achieved between simulated and measured results. The coupling between the input and output circuits adds additional feedback which must be included in simulations to achieve this level of accuracy. In the presented LNA, no shielding has been implemented. Better separation between the input and output circuits is possible by placing a shield around the input and/or output circuits. The primary purpose of the shielding is to lower the noise figure of the LNA even further. This potentially avoids the 0.15 dB increase in noise figure in comparison to the present circuit implementation.

The noise figure simulations and measurements appear slightly offset. However, the 95th percentile noise figure uncertainty of the transistor, as specified by the manufacturer, is 0.15 dB. Further, the 95th percentile measurement uncertainty is 0.16 dB. With this in mind, the noise figure measurements and simulations lie within expected results.

Another aspect, which has a large effect on the measured noise performance, is the noise injected by the voltage supply. The presented design utilizes a Linear Drop Out (LDO) regulator as described in [50]. A switch-mode voltage supply was used in the initial design. The switch-mode supply added approximately 0.2 dB noise compared to the LDO solution.

The concept of flicker noise has not been devoted much attention thus far because it is not an issue with the current transistor when operated at 32.1 MHz. However, using the design with a different transistor and/or at a lower frequency, the flicker

Table A.1: Comparison of LNA designs for MRI

	Siemens [45, 46]	**Cao *et. al.* [46]**	**TI [47]**	**Agile [48]**	**WanTcom [49]**	**Johansen *et. al.* [27]**	**This work**
Frequency (MHz)	128	128	63/128	43	32.1	32.1	32.1
NF (dB)	0.71	1.02	0.6	0.4	0.7	0.75	0.44
Gain (dB)	27	32	28	30	28	20	22
$Z^{(\mathrm{P})}$ (Ω)	$2.2 + j21$	$3.6 + j1.6$	1.5	2	3	$0.4 + j67$	$-1.1 + j73$
$P_{\mathrm{in,1dB}}$ (dBm)	-14.5	-28.5	12	0	9	-13.8	-14.5
$P^{(\mathrm{P})}$ (mW)	196	215	108	152	180	99	81

noise may become an issue. The primary strategy towards flicker noise is to use a transistor technology with a lower corner frequency [25].

The gain is at an acceptable level for this application. However, at higher frequencies, the gain may become an issue due to the lower inherent gain of the transistor. An additional stage can be included to increase the gain. Assuming that the additional second stage has a noise figure of 1 dB, the overall noise figure will degrade by 0.006 dB according to Friis' equation for cascaded noise figure [51]. This, of course, depends on the gain of the first stage. Assuming that the LNA had a gain of 10 dB, the overall noise figure would be degraded by 0.1 dB. Hence, from a noise perspective, increasing the gain is a simple matter entailing a minor noise impact. However, the additional stage also increase the power consumption.

One of the primary targets of this work is to demonstrate maximum achievable decoupling. Hence, having a conditionally stable LNA is acceptable. If less decoupling is tolerated, the stability of the LNA can be increased by adjusting the output circuit accordingly. The required decoupling depends immensely on the design of the coil array. Many designs use overlapping elements for nearest neighbour decoupling and the distance to the next nearest neighbour determines the amount of decoupling required. For most overlapping designs, a decoupling of around 25 dB is acceptable. For parallel imaging, however, non-overlapping elements can significantly increase performance. To collect the most magnetic flux, the non-overlapping elements need to be placed very close and higher decoupling (depending on separation and shape) is required to not impair both SNR of the individual elements and noise correlation between elements. It is expected that this method is used primarily for parallel imaging coil arrays, where a high degree of decoupling is required.

The bandwidth of the decoupling is fairly narrow, which may be an issue for some MRI sequences having a bandwidth of 50-100 kHz. A frequently used sequence for ^{13}C imaging in 3 T MRI scanners is Chemical Shift Imaging (CSI) and it typically requires a bandwidth of 5 kHz. Thus, using a CSI sequence, the bandwidth is not an issue. For broadband applications, the presented method can be used if a proper

output circuit can be synthesized.

A comparison of different LNA designs for MRI is presented in Table A.1 for, not only 32.1 MHz, but higher frequencies as well. The only readily available commercial MRI compatible LNA for 32.1 MHz is the WanTcom. This work achieves a noise figure 0.26 dB better than the WanTcom. For 43 MHz, the Agile LNA shows the best noise figure performance of 0.4 dB. The gain of the LNA presented here is lower than the other designs, however, according to [27], this does not pose a problem. As far as the authors are aware, the LNA presented here achieves the best decoupling performance thus far published (when only using the LNA for decoupling). This is because a stable negative input resistance has been realised.

This work has presented an iterative approach to dissociation LNAs. In terms of practical applicability we have experienced that an iterative approach is often employed even though the method may principally be analytic. In [26] an analytic method is described which is based on the same theory as this work and is, at least partly, capable of designing an HRNM LNA. If the analysis of maximum stable gain in [26] is replaced by an analysis of augmented resistance for stability purposes, it might be possible to change the proposed iterative solution to an analytical. However, because unconditional stability for negative impedance devices is impossible, the stability of the system will depend on the source and load. Hence, a generalization of the system source and load impedances is required and thus will not truly represent all systems.

The concept of association has not been devoted much attention thus far. The transistor used in this work cannot inherently achieve SNIM. Hence, additional feedback must be added. This is also what other methods require. However, other methods for SNIM vary only the amount of feedback. From this method, it is possible to combine both feedback and the output circuit impedance. Since bipolar junction-type transistors generally exhibit lower input impedance, they may be better suited for SNIM.

A.6 Conclusion

Using noise and S-parameters, a general approach to the LNA design has been proposed. LNA design spans three cases which we define as design by association (decreasing the mismatch between optimal noise and input impedance), equilibrium (optimal noise matched input while output is gain matched), and dissociation (high reflection coefficient input impedance while being noise matched). The primary target is an LNA with a negative resistance, inductive input impedance for MRI receive

coil arrays. The LNA design achieves a noise figure of 0.44 dB, which is better than existing MRI LNAs at 32.1 MHz. The LNA shows a decoupling of 54 dB. The presented method is primarily applicable for designing LNAs with a high input reflection coefficient while exhibiting low noise. However, the method can also be used for simultaneous noise and input match. It is expected that the presented design method and LNA enables new design strategies for MRI receive coil arrays, especially for parallel imaging applications.

Appendix

Potential Broadband Application

This appendix briefly discusses the potential of applying the design method for applications more broadband than MRI. For this discussion, an ideal common source topology is explored operating from 850 MHz to 1000 MHz (approximately the E-UTRA band 8). The corresponding relative bandwidth is approximately 16 %. The biasing and feeding inductors used are ideal (infinitely large and lossless). The same applies for DC blocking capacitors. Using these ideal components, the simulated noise figure, when the source is 50 Ω, is maximally 0.21 dB at 1000 MHz. The supply voltage is 3 V, using a biasing voltage of 0.5 V. Hence, when using the ATF58143 transistor, there is no need for additional noise matching according to simulations.

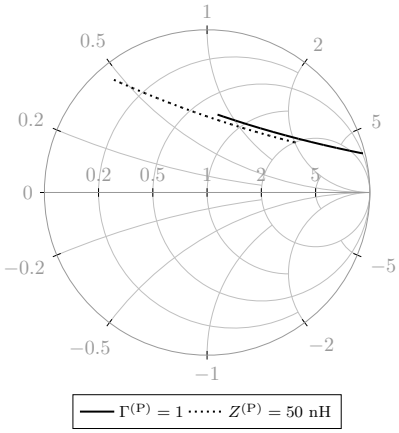

Figure A.12: Simulated required impedance of the output circuit looking toward the load in the frequency range from 850 MHz to 1000 MHz to realize either an ideal instrumentation amplifier (solid) or an ideal inductor (dotted).

Iteratively solving (A.5) over the frequency range while varying the electrical length of the input transmission line, a solution is found utilizing a passive output circuit. Instead of focussing on a single frequency and plotting the impedance circles, $Z^{(O)}$ is plotted in the Smith Chart over frequency, as seen in Fig. A.12.

For the two examples given in Fig. A.12 the required input impedance was either $\Gamma^{(P)} = 1$ (solid) or $Z^{(P)} = 50$ nH (dotted). The electrical length of the transmission line is 100° at 925 MHz, with a characteristic impedance of 50 Ω. How to synthesize an output circuit capable of (approximately) providing the required $Z^{(O)}$ will not be discussed in this paper. However, if the $Z^{(O)}$ in Fig. A.12 can be realized, it is possible to extend the design method to apply for wider bandwidths.

References

[1] X. Cao, D. Zu, X. Zhao, Y. Fan, and J. Gao, "The design of a low-noise preamplifier for mri," *Science China Technological Sciences*, vol. 54, no. 7, pp. 1766–1770, Jul 2011.

[2] P. B. Roemer, W. A. Edelstein, and C. E. Hayes, "The NMR Phased Array," *Soc. Magn. Reson. Med.*, vol. 225, pp. 192–225, 1990.

[3] C.-N. Chen and D. I. Hoult, *Biomedical Magnetic Resonance Technology*, 1st ed. Institute of Physics Publishing, 1989.

[4] D. G. Nishimura, *Principles of Magnetic Resonance Imaging*, 1st ed. lulu.com, 2010.

[5] J. Engberg, "Simultaneous input power match and noise optimization using feedback," in *European Microwave Conf.*, Sept 1974, pp. 385–389.

[6] L. Boglione, R. D. Pollard, V. Postoyalko, and T. Alam, "Specifications for a linear network simultaneously noise and available-power matched," *IEEE Microw. and Guided Wave Letters*, vol. 6, no. 11, pp. 407–409, Nov 1996.

[7] L. Boglione, R. D. Pollard, and V. Postoyalko, "BJT Feedback LNA with Input Port Simultaneously Signal and Noise Matched," in *27th EuMC*, vol. 2, Sept 1997, pp. 1052–1057.

[8] ——, "Optimum noise-source reflection-coefficient design with feedback amplifiers," *IEEE Trans. Microw. Theory Techn.*, vol. 45, no. 3, pp. 402–407, Mar 1997.

[9] T.-K. Nguyen, C.-H. Kim, G.-J. Ihm, M.-S. Yang, and S.-G. Lee, "CMOS low-noise amplifier design optimization techniques," *IEEE Trans. Microw. Theory Techn.*, vol. 52, no. 5, pp. 1433–1442, May 2004.

[10] Y. Shim, C.-W. Kim, and S.-G. Lee, "Simultaneous noise and input matched ultra wide band LNA design," *Microwave and Optical Tech. Letters*, vol. 49, no. 9, pp. 2275–2279, 2007.

[11] R. E. Lehmann and D. D. Heston, "X-Band Monolithic Series Feedback LNA," *IEEE Trans. Microw. Theory Techn.*, vol. 33, no. 12, pp. 1560–1566, Dec 1985.

[12] N. Shiga, S. Nakajima, K. Otobe, T. Sekiguchi, N. Kuwata, K. i. Matsuzaki, and H. Hayashi, "X-band MMIC amplifier with pulse-doped GaAs MESFET's," *IEEE Trans. Microw. Theory Techn.*, vol. 39, no. 12, pp. 1987–1994, Dec 1991.

[13] Y. Tsukahara, S. Chaki, Y. Sasaki, K. Nakahara, N. Andoh, H. Matsubayasi, N. Tanino, and O. Ishihara, "A C-band 4-stage low noise miniaturized amplifier using lumped elements," in *Proc. IEEE MTT-S Intern. Microwave Symp.*, May 1995, pp. 1125–1128 vol.3.

[14] S. P. Voinigescu, M. C. Maliepaard, J. L. Showell, G. E. Babcock, D. Marchesan,

M. Schroter, P. Schvan, and D. L. Harame, "A scalable high-frequency noise model for bipolar transistors with application to optimal transistor sizing for low-noise amplifier design," *IEEE J. Solid-State Circuits*, vol. 32, no. 9, pp. 1430–1439, Sep 1997.

[15] S. Hara, K. Osato, A. Yamada, T. Tsukao, and T. Yoshimasu, "Miniaturized low noise variable MMIC amplifiers with low power consumption for L-band portable communication applications," in *IEEE Microwave and Millimeter-Wave Monolithic Circuits Symp.*, June 1993, pp. 67–70.

[16] T. Seshita, K. Kawakyu, W. Wakimoto, M. Nagaoka, Y. Kitaura, and N. Uchitomi, "A 2-V operation RF front-end GaAs MMIC for PHS hand-set," in *IEEE MTT-S Intern. Microwave Symp.*, vol. 1, June 1998, pp. 167–170 vol.1.

[17] F. Lin, L. Liu, P. S. Kooi, and M. S. Leong, "Design of MMIC LNA for 1.9 GHz CDMA portable communication," in *Proc. Microwave and Millimeter Wave Techn.*, 1998, pp. 205–208.

[18] K. B. Niclas, "The Exact Noise Figure of Amplifiers with Parallel Feedback and Lossy Matching Circuits," *IEEE Trans. Microw. Theory Techn.*, vol. 30, no. 5, pp. 832–835, May 1982.

[19] ——, "Noise in Broad-Band GaAs MESFET Amplifiers with Parallel Feedback," *IEEE Trans. Microw. Theory Techn.*, vol. 30, no. 1, pp. 63–70, Jan 1982.

[20] J. Tajima, Y. Yamao, T. Sugeta, and M. Hirayama, "Gaas monolithic low-power amplifiers with rc parallel feedback (short paper)," *IEEE Trans. Microw. Theory Techn.*, vol. 32, no. 5, pp. 542–544, May 1984.

[21] G. Gonzalez, *Microwave Transistor Amplifiers - Analysis and Design*, 2nd ed. Prentice Hall, 1997.

[22] D. M. Pozar, *Microwave Engineering*, 3rd ed. Wiley, 2005.

[23] H. A. Haus, W. R. Atkinson, G. M. Branch, W. B. Davenport, W. H. Fonger, W. A. Harris, S. W. Harrison, W. W. Mcleod, E. K. Stodola, and T. E. Talpey, "Representation of Noise in Linear Twoports," *Proc. IRE*, vol. 48, no. 1, pp. 69–74, Jan 1960.

[24] A. van der Ziel, "Representation of noise in linear two-ports," *Proc. IEEE*, vol. 57, no. 6, pp. 1211–1211, June 1969.

[25] F. A. Levinzon, "Ultra-Low-Noise High-Input Impedance Amplifier for Low-Frequency Measurement Applications," *IEEE Trans. Circuits Syst. I, Reg. Papers*, vol. 55, no. 7, pp. 1815–1822, Aug 2008.

[26] W. Ciccognani, P. E. Longhi, S. Colangeli, and E. Limiti, "Constant Mismatch Circles and Application to Low-Noise Microwave Amplifier Design," *IEEE Trans. Microw. Theory Techn.*, vol. 61, no. 12, pp. 4154–4167, Dec 2013.

[27] D. H. Johansen, J. D. Sánchez-Heredia, V. Zhurbenko, and J. H. Ardenkjær-Larsen, "Practical Aspects of Preamplifier Designs for 13C Imaging," in *Proc. Intl. Soc. Mag. Reson. Med. 25*, 2017.

[28] E. W. Herold, "Negative Resistance and Devices for Obtaining It," *Proc. IRE*, vol. 23, no. 10, pp. 1201–1223, Oct 1935.

[29] J. L. Merrill, "Theory of the negative impedance converter," *The Bell System Technical Journal*, vol. 30, no. 1, pp. 88–109, Jan 1951.

[30] J. G. Linvill, "Transistor Negative-Impedance Converters," *Proc. IRE*, vol. 41, no. 6, pp. 725–729, June 1953.

[31] J. Brownlie, "On the Stability Properties of a Negative Impedance Converter," *IEEE Trans. Circuit Theory*, vol. 13, no. 1, pp. 98–99, Mar 1966.

[32] K. Kurokawa, "Power Waves and the Scattering Matrix," *IEEE Trans. Microw. Theory Tech.*, vol. 13, no. 2, pp. 194–202, 1965.

[33] E. Kreyszig, *Advanced Engineering Mathematics*, 9th ed. John Wiley & Sons, Inc., 2006.

[34] D. H. Johansen, J. D. Sanchez-Heredia, V. Zhurbenko, and J. H. Ardenkjsr-Larsen, "Towards New Vistas in Preamplifier Design for MRI," in *12th EuMIC*, Oct 2017, pp.

419–422.
[35] A. Reykowski, S. M. Wright, and J. R. Porter, "Design of Matching Networks for Low Noise Preamplifiers," *Magn. Reson. Med.*, vol. 33, no. 6, pp. 848–852, 1995.
[36] J. D. Sanchez-heredia, E. Søvsø, S. Hansen, C. Laustsen, V. Zhurbenko, and J. H. Ardenkjær-larsen, "Low-Noise Active Decoupling Circuit and its Application to 13C Cryogenic RF Coils at 3 T," *Tomography*, vol. 3, no. 1, pp. 60–66, 2017.
[37] *ATF-58143: Low Noise Enhancement Mode Pseudomorphic HEMT in a Surface Mount Plastic Package (Data Sheet)*, Avago Technologies, 2012.
[38] M. L. Edwards and J. H. Sinsky, "A new criterion for linear 2-port stability using a single geometrically derived parameter," *IEEE Trans. MTT*, vol. 40, no. 12, pp. 2303–2311, Dec 1992.
[39] J. Rollett, "Stability and Power-Gain Invariants of Linear Twoports," *IRE Transactions on Circuit Theory*, vol. 9, no. 1, pp. 29–32, March 1962.
[40] R. Behin, J. Bishop, and R. M. Henkelman, "Dynamic range requirements for MRI," in *Proc. Intl. Soc. Mag. Reson. Med. 13*, 2005.
[41] ——, "Dynamic range requirements for MRI," *Concepts in Magnetic Resonance Part B: Magnetic Resonance Engineering*, vol. 26B, no. 1, pp. 28–35, 2005.
[42] D. Hoult and R. Richards, "The signal-to-noise ratio of the nuclear magnetic resonance experiment," *J. Magn. Reson.*, vol. 24, no. 1, pp. 71–85, 1976.
[43] D. I. Hoult and P. C. Lauterbur, "The sensitivity of the zeugmatographic experiment involving human samples," *J. Magn. Reson.*, vol. 34, no. 2, pp. 425–433, 1979.
[44] D. I. Hoult, "The principle of reciprocity in signal strength calculations—A mathematical guide," *Concepts Magn. Reson.*, vol. 12, no. 4, pp. 173–187, 2000.
[45] *Part number: 7576312, 128 MHz Preamplifier*, Siemens.
[46] X. Cao, E. Fischer, J. G. Korvink, O. Gruschke, J. Hennig, and M. Zaitsev, "Design of a 3T preamplifier which is stability insensitive to coil loading," *J. Magn. Reson.*, vol. 265, pp. 215–223, 2016.
[47] *TL5500: Low-Noise Pre-Amplifier for MRI (SLAS093C)*, Texas Instruments, 2012.
[48] *AMT-AN0064: 40 MHz to 50 MHz Non-Magnetic Low Noise Amplifier*, Agile Microwave Technology Inc., rev. B.
[49] *WMA32C: 32.19 MHz Low Noise Low Impedance Preamplifier*, WanTcom Inc., 2013, rev. B.
[50] D. H. Johansen, J. D. Sanchez-Heredia, J. R. Petersen, T. K. Johansen, V. Zhurbenko, and J. H. Ardenkjær-Larsen, "Cryogenic Preamplifiers for Magnetic Resonance Imaging," *IEEE Trans. on Biomedical Circ. and Syst.*, vol. 12, no. 1, pp. 202–210, Feb 2018.
[51] H. T. Friis, "Noise Figures of Radio Receivers," *Proc. IRE*, pp. 419–422, 1944.

Paper B

Cryogenic Preamplifiers for Magnetic Resonance Imaging

D. H. Johansen, J. D. Sanches-Heredia, V. Zhurbenko, and J.H. Ardenkjær-Larsen

IEEE Transactions on Biomedical Circuits and Systems, vol. 12, no. 1, pp. 202-210, Feb. 2018

The layout has been revised.

Abstract

Pursuing the ultimate limit of detection in magnetic resonance imaging (MRI) requires cryogenics to decrease the thermal noise of the electronic circuits. As cryogenic coils for MRI are slowly emerging cryogenic preamplifiers are required to fully exploit their potential. A cryogenic preamplifier operated at 77 K is designed and implemented for ^{13}C imaging at 3 T (32.13 MHz), using off-the-shelves components. The design is based on a high electron mobility transistor (ATF54143) in a common source configuration. Required auxiliary circuitry for optimal cryogenic preamplifier performance is also presented consisting of a voltage regulator (noise free supply voltage and optimal power consumption), switch and trigger (for active detuning during transmission to protect the preamplifier). A gain of 18 dB with a noise temperature of 13.7 K is achieved. Performing imaging experiments in a 3T scanner showed an 8 % increased signal-to-noise ratio (SNR) from 365 to 399 when lowering the temperature of the preamplifier from 296 K to 77 K while keeping the coil at room temperature. This work thus enables the merger of cryogenic coils and preamplifiers in the hopes of reaching the ultimate limit of detection for MRI.

B.1 Introduction

Combining anatomical proton (^{1}H) magnetic resonance imaging (MRI) and hyperpolarized metabolic carbon (^{13}C) magnetic resonance spectroscopic imaging (MRSI) yields a superlative clinical diagnostic tool for investigation cancer aggressiveness and treatment response much earlier than with other non-invasive imaging procedures [1, 2]. One of the primary concerns of MRI is the inherently limited signal-to-noise ratio (SNR) impairing image quality (making it harder for clinicians to evaluate results) and acquisition speed (increasing scanner time and thus cost) [3]. Further, for hyperpolarization due to the transient nature of the experiment, higher baseline SNR is invaluable because averaging is generally not viable since it would involve multiple injections of contrast agent [4]. To approach the ultimate limit of detection in MRI and especially for applications of hyperpolarization, cryogenics are paramount. Cryogenically cooled receive coils are receiving a lot of attention in the form of either copper or high temperature superconducting (HTS) surface coils. However, design and implementation of cryogenic preamplifiers and required auxiliary systems have largely been omitted within the MRI community.

A clinical MRI system consist of two primary magnetic fields. The main field B_0 is a

static magnetic field generally ranging from 1.5 to 7 T, which create a proportional weak polarization of the nuclear spins of the patient. The primary nuclear spin in a clinical setting is ^{1}H. In the hyperpolarized regime many different nuclei can be imaged such as ^{129}Xe, ^{3}He, ^{15}Ni or ^{13}C [5]. Here focus is limited to ^{13}C. The precession (resonance) frequency of the nuclear spins is the product of the main field strength and the gyromagnetic ratio of the nuclei. By applying an RF pulse (a second magnetic field) orthogonally to the main field at the Larmor frequency of the nuclei of interest tilts them away from equilibrium. When the RF pulse is switched off the nuclei relax back to equilibrium. The precession is then captured by Faraday induction [6, 7].

Using cryogenics to improve SNR within nuclear magnetic resonance spectroscopy (NMR) and MRI is well known. H. Kovacs *et al.* [8] thoroughly reviews the history of cryogenic probes for NMR. L. Darrasse *et al.* [9] reviewed cryogenic biomedical MRI probes. Within biomedical MRI the largest breakthrough so far is achieved by Bruker with their CryoProbe for preclinical small animal studies [10, 11].

Publications and commercial products for room temperature preamplifiers for MRI is plentiful. C. Lim *et al.* [12] describes three designs for 619 MHz. S. Yadav [13] presents simulations of a cascaded topology for 64 MHz. F. Doty *et al.* [14] provides a topology for 300 MHz excluding stabilization components. Several vendors source room temperature MRI preamplifiers e.g. WanTcom [15], Teledyne e2v [16] and Hi-Q.A. Inc. [17].

The focus of this work is cryogenic preamplifiers for MRI where publications are very sparse. M. Pospieszalski has written a general review on cryogenic amplification using field effect transistors [18]. Cryogenic preamplifiers are used in a range of different applications ranging from the deep space network [19] over SQUIDs [20, 21] and proof-of-concepts [22–24] to NMR [25–28]. For MRI applications, J.G. van Heteren *et al.* [29] mentions the use of a cryogenic preamplifier based on a JFET for 2.7 MHz cooled to 77 K. However, no design is supplied and thus reproducing is not possible. F. Resmer *et al.* [30] provides a design for 425 kHz MRI also based on a JFET operating at 77 K. Hence the field of cryogenic preamplifiers for MRI is a sparse field with only a few publications aimed at low main magnetic field applications and excluding a complete design.

The primary contributions of this work is the design and implementation of a cryogenic preamplifier for MRI based on an enhancement mode pseudomorphic high electron mobility transistor (pHEMT) utilizing a common source topology cooled to 77 K using liquid nitrogen for ^{13}C imaging at 3 T (32 MHz). Furthermore, no current literature describe required auxiliary systems when using preamplifiers in a clinical

MRI scanner. The auxiliary systems contains circuitry such as voltage regulators and active detuning switching for protecting the preamplifier. Hence, an additional contribution of this work is the description of auxiliary circuitry used for both room temperature and cryogenic preamplifiers.

B.2 System Overview

Before exploring the intricacies of developing cryogenic preamplifiers the system architecture is presented. Apart from the coils generating the main, gradient and RF fields the general system is seen in Fig. B.1. It is a receive only system based on a volume coil with attached matching and active detuning network. Following the coil and matching circuit is the preamplifier placed inside a cryostat. The cryostat is cooled to 77 K using liquid nitrogen. Separating the cryogenic preamplifier from the coil is an unusual constellation. Normally the coil and matching circuit would also be cooled. However, only the preamplifier is cooled because it is the primary focus of this work. This also makes characterization of the cryogenic preamplifier much easier since the input and output terminals are at room temperature. The matching and active detuning circuit is described by J. D. Sanzhez-Heredia *et al.* [31].

The auxiliary circuitry consists of the regulator, trigger and switch. In order to optimize the power consumption for a given preamplifier a voltage regulator is usually needed. Also, the voltage regulator further filters the supply signal. An active detuning signal is also supplied from the scanner. A high voltage level indicates that RF transmission is commencing. A low voltage indicates that the scanner is ready to receive. Hence, at a high active detuning voltage the switch needs to disengage

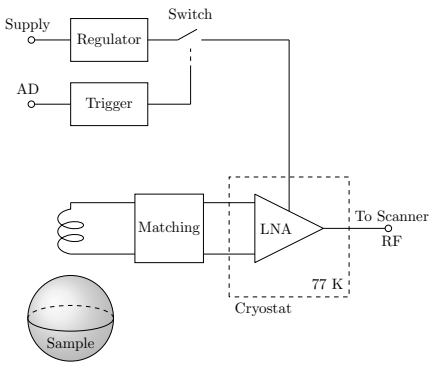

Figure B.1: Overview of the system. The regulator, switch and trigger constitute the auxiliary system. The low noise preamplifier (LNA) is operated at 77 K while the coil is kept at room temperature.

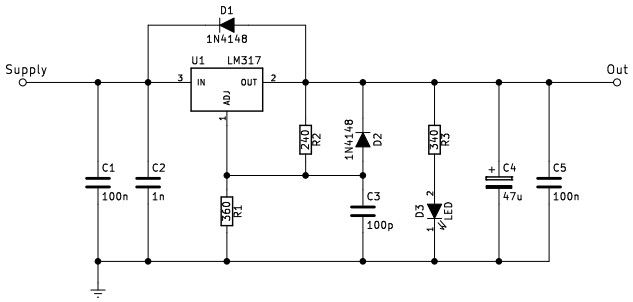

Figure B.2: Schematic of the voltage regulator [32]. This is a classic design where D3 and R3 is added to act as a state indicator and to draw a small current which lock the output voltage of the LM317 which otherwise is floating.

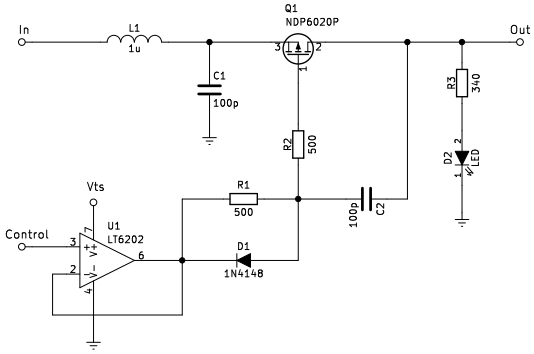

Figure B.3: Schematic of the fast supply switch based on a P-channel MOSFET acting as the supply switch. It is controlled by the signal from the trigger which is buffered by U1 in order to ensure proper current sourcing and sinking during switching.

the supply voltage to the preamplifier in order to minimize the impact of the high powered RF pulse. The trigger thus acts both as an inverter and a filter.

B.2.1 Voltage Regulator

The voltage regulator circuit is based on an LM317 linear regulator and seen in Fig. B.2 [32]. Here the capacitors C1, C2, C4 and C5 ensures stability and filters unwanted noise. The diodes D1 and D2 are overvoltage protection. The resistors R1 and R2 determine the output voltage. If no current is drawn from the regulator the output voltage is undefined and could cause problems when the preamplifier is off during transmission. The resistor R3 and LED D3 are loading the regulator with a small current to ensure that the output voltage remains constant even with no load.

B.2.2 Switch

The switch, Fig. B.3, is designed around a P-channel MOSFET Q1. To control and limit the preamplifier inrush current the transistor turn on must be controllable and reproducible. This is done by increasing the transistors Miller capacitance via C2. With R2 working as a current source, driving C2 and the transistor gate. The transistor thus ramps the output voltage up linearly. Turn off is fast due to the diode D1, pulling the transistor gate to the positive supply rail, only limited by R1 and the operational amplifiers, U1, output current. R2 prevents the transistor from oscillating when turning on and off. L1 and C1 low-pass filters the power supply to the amplifier. R3 and D2 is a simple power on indicator.

B.2.3 Schmitt Trigger

The trigger circuit is seen in Fig. B.4. It is a non-inverting Schmitt trigger topology using an LT6202 operational amplifier triggering a low output when the input voltage transitions above a threshold voltage V_{h}. When the input transitions below V_{l} the output is pulled high. The diodes D1 and D2 prevent the input to the operational amplifier from going above or below the supply rails by more than the knee voltage of the diodes. The series resistor R1 limits the current and is chosen such that only a few hundred micro amperes are drawn from the active decoupling circuit at maximum applied voltage. This also protects the diodes from failure by limiting the current they

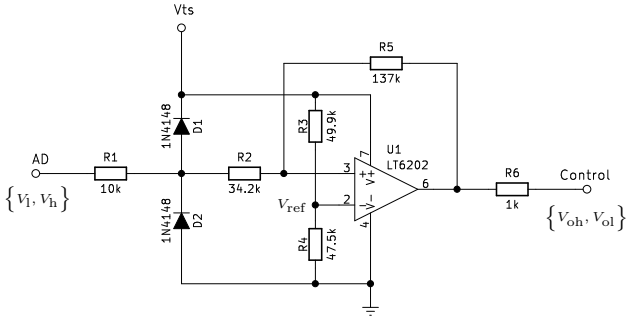

Figure B.4: Schematic of the trigger circuit. It is a non-inverting Schmitt trigger topology with input protection in the form of R1, D1, and D2.

can source or sink. The non-inverting Schmitt trigger is described by

$$R1 + R2 = \frac{R_5 \left(V_\mathrm{l} - V_\mathrm{h}\right)}{V_\mathrm{oh} - V_\mathrm{ol}}, \tag{B.1}$$

$$V_\mathrm{ref} = \frac{V_\mathrm{h} V_\mathrm{ol} - V_\mathrm{l} V_\mathrm{oh}}{V_\mathrm{h} - V_\mathrm{l} - V_\mathrm{oh} + V_\mathrm{ol}}, \tag{B.2}$$

where V_oh and V_ol are the high and low output of the operational amplifier respectively. In this case the operational amplifier is a singly supply, rail to rail and thus the high voltage is equal to Vts and the low voltage is 0 V. V_ref is the voltage at pin 2 of U1 determined by the voltage division of R3 and R4. The voltage Vts is a regulated voltage fed from a separate regulator circuit identical to Fig. B.2. This is to separate the switching supply from the more critical preamplifier supply voltage.

B.3 Preamplifier Design

B.3.1 Transistor

Transistors are typically separated into two basic types; the bipolar junction transistor (BJT) and field effect transistor (FET). An NPN type BJT is made by sandwiching a P-type semiconductor between two N-type semiconductors. In the N-type semiconductor the majority charge carriers are electrons, whereas in the P-type they are holes. Thus when a voltage (principally an electric field) is applied, electrons are injected from the emitter and into the base where they diffuse to the collector. In the base, being a P-type material, the electrons are minority charge carriers [33]. Minority charge carriers can only be thermally excited. Hence at low temperatures the electrons excited into the conduction band is essentially zero and thus freeze out occurs; the semiconductor becomes an insulator. At low temperatures the diffusion length, especially from base to emitter, becomes significantly impaired. Hence electron mobility in a BJT at low temperatures is very low and the current gain approaches unity [34, 35]. The story is somewhat the same for the PNP type BJT. Here the emitter and collector are P-type exhibiting freeze out, which leads to an even worse performance at low temperature [36]. During the late 1980s bandgap engineering lead to the invention of the heterojunction bipolar transistor (HBT). An HBT can be used at low temperatures but require specific design of the transistor [37–42]. Since a dedicated transistor process is usually not available, we draw the conclusion that bipolar transistors are generally not an option for low temperature electronic designs. This further excludes the use of many operational amplifiers since they, for the most part, employ a mixture of NPN and PNP type BJTs.

The conclusion is, luckily, the opposite for N-type FETs. Since electrons are majority charge carriers and excitation is dominated by the electric field in the gate, N-type FETs become less dependent on temperature. Indeed fewer electrons are excited at lower temperatures but this effect is easily compensated by increasing the gate voltage [36, 43]. A higher gate voltage entails a higher electrical field in the device. Hence, the voltage cannot be increased infinitely because the transistor first electrically collapses (avalanche effect) and finally physically breaks down. MOSFETs tend to not show good cryogenic performance due to trapping in the metal oxide resulting in a significantly higher flicker noise [36]. Further, P-type FETs do not function properly at low temperatures due to the electron transport being by minority charge carriers in the P-type material. Hence operating silicon based integrated circuits using FET technology at cryogenic temperatures is a challenge due to two reasons; usage of both N- and P-type FETs and changed characteristics of the FET at lower temperature which cannot be compensated externally [44]. As BJTs evolved into HBTs so FETs developed into pHEMTs by use of bandgap engineering. A pHEMT is essentially an FET on steroids. In a pHEMT the electrons have a higher mobility yielding better gain and noise performance, especially at higher frequencies. Furthermore, having higher electron mobility decreases the freeze out temperature while still driven by field effect. Hence it should perform well at cryogenic temepratures.

B.3.2 Topology

The implemented topology consists of a pHEMT in a common source configuration with added stability measures as seen in Fig. B.5 [45]. The source of the transistor Q1 is connected to ground, the gate is used as a high impedance voltage input and the drain is a voltage controlled current output.

The stability of a two port network is determined by the Edward-Sinsky stability factor [46],

$$\mu = \frac{1 - |S_{11}|^2}{|S_{22} - S_{11}^* \Delta| + |S_{12} S_{21}|} > 1, \tag{B.3}$$

$$\Delta = S_{11} S_{22} - S_{12} S_{21}, \tag{B.4}$$

where S_{xy} are the four S-parameters of the preamplifier as a function of frequency. Equation (B.3) represents the necessary and sufficient conditions for stability of a two port. The more frequently used Rollett stability factor K constitutes only a necessary condition and must be paired with the condition $\Delta < 1$ to ensure stability [47].

Seen from the gate of Q1 the components L1, C1, C2 and R1 constitute a high pass

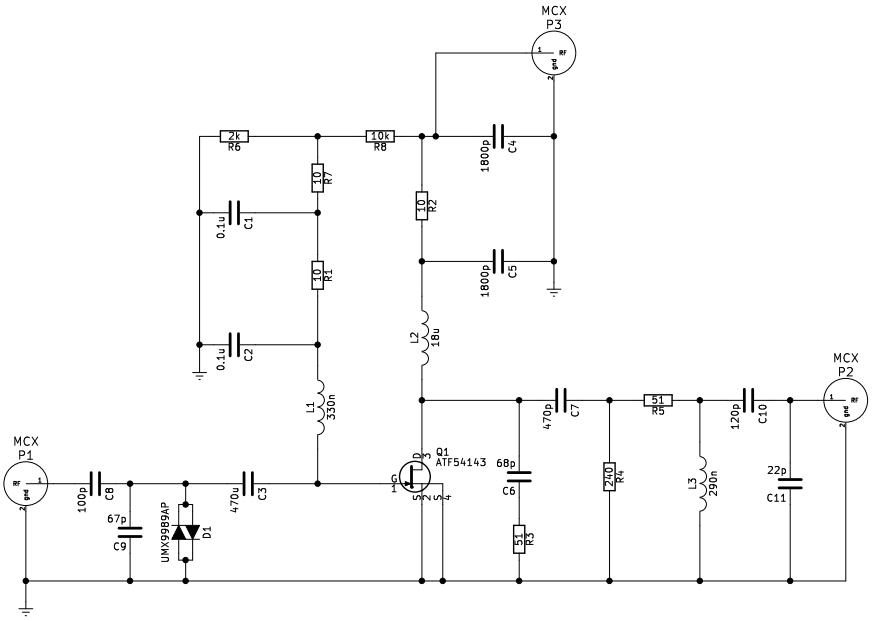

Figure B.5: Schematic of the preamplifier. The design is based on a common source topology using feed inductors in both input and output. Stability is ensured primarily on the output by resistive attenuation.

filter. The high pass filter on the input ensures low frequency stability according to (B.3). Furthermore, the inductor L1 is chosen such that the impedance at the gate (G1) is inductive. Hence, the series-shunt connected capacitors C8 and C9 match the optimal noise impedance of the preamplifier to 50 Ω. Resistors R6 and R8 determine the bias voltage. It is vital that the resistors are chosen such that the impedance seen by the high pass filter is high. If the biasing resistors alter the characteristics of the high pass filter oscillation might occur. The required bias voltage is found as a trade-off between the wanted noise and gain of the transistor. Especially at lower temperatures, as presented in the previous subsection, the bias voltage should be increased to maintain the same gain as at room temperature.

On the drain of Q1 is the feed inductor L2 which should be chosen such that the resulting impedance is high. Some designs employ a parallel capacitor across L2 resonant at the frequency of interest. L2 is preceded by a supply filter consisting of C5, C4 and R2 in order to make sure the voltage from the regulators are properly filtered. The size of R2 and the resistance of L2 implicitly determine the compression point of the preamplifier by controlling the voltage at the drain of the transistor. Larger resistance results in lower voltage at the drain of Q1 hence the compression point is also lowered. The capacitors C4 and C5 should be chosen as large as possible

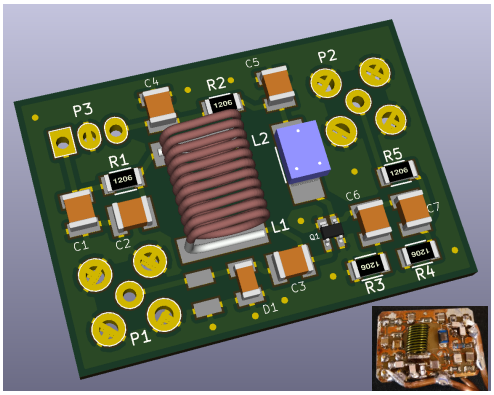

Figure B.6: Example of preamplifier layout excluding biasing resistors, input and output matching. In the bottom right the preamplifier photo is shown where biasing, input and output matching has been reworked to fit the layout. The size of the PCB is 37 mm x 26 mm.

but is a trade-off between blanking time of the preamplifier, since they increase the time constant of the filter and the resonance of the capacitors arising from internal parasitics.

The capacitor C6 and resistor R3 forms a low pass filter ensuring high frequency stability. Furthermore, resistors R4 and R5 form a broadband attenuator which also increase stability of the preamplifier. Capacitors C3 and C7 are simply DC blocks. The output matching is tuned by adjusting L3, C10 and C11. Finally, a set of UMX9989 crossed protection diodes D1 are placed at the input to short out any excess power from the transmitter.

The layout of the preamplifier is seen in Fig. B.6. The primary aspect of the layout is grounding. Especially at the protection diodes and the transistor. If the transistor source is not properly grounded an inductor is effectively connected between the source and the ground. Hence a source degenerated topology arises. By simulation and experiment this was seen to make the preamplifier more low frequency stable, but more high frequency unstable.

B.3.3 Passive Components

Passive components for cryogenic operation are not readily available. Even though most passive components are rated in the -50 to 150 degree centigrade range they can be used at lower temperatures. Their value, however, will change by some significant amount. Given resistors of 200 ppm/K a corresponding 5 % additional resistance occurs at 77 K.

Capacitors, depending on the materials used for construction, can behave much different. Examples of X5R and Y5V type capacitors at 77 K shows not only an 80 % decreased capacitance, but also a significant increase in equivalent series resistance (ESR). In brief, all capacitors operated at cryogenic temperatures should be NP0 type showing an approximate 3 % capacitance increase whereas ESR is decreased [48, 49]. Hence the Q-factor is increased. This must be taken into account when designing the preamplifier.

B.4 Measurement Setup

B.4.1 Bench Characterization

For bench characterization the preamplifier is disconnected from the coil in Fig. B.1. The S-parameter matrix is measured using an Agilent ENA (E5062A) network analyzer by performing a two port measurement. In order to measure the noise an Agilent PSA (E4440A) spectrum analyzer with noise extension (346B) is used. For noise measurements the noise source is connected to the input of the preamplifier and the output is connected to the spectrum analyzer. The preamplifier and cryostat are placed in a shielded box (R&S CMW-Z10) to attenuate spurious signals impairing the noise measurement.

B.4.2 Verification in Scanner

The system shown in Fig. B.1 is tested in a scanner with a small animal (mouse) volume coil. In this work a clinical 3 T General Electric Signa HDx is used. To obtain images a chemical shift imaging (CSI) sequence is used with a field-of-view of 120 mm x 120 mm, slice thickness 10 mm and 16-by-16 points. The duration of each scan is 19 s and 128 averages is used. Thus resulting in a scan time of just under 41 min. A 1 M ^{13}C-bicarbonate spherical phantom, 37.5 mm in diameter, is used. The phantom corresponds electrically to a rat.

B.5 Results

B.5.1 Auxiliary Systems

The supply voltage from the scanner is 10 V. The voltage regulator design in Fig. B.2 outputs 3.15 V. The nominal supply voltage for the preamplifier is 3 V. The extra 0.15 V is dropped in the LC filter prior to Q1 in Fig. B.3. The trigger is designed using a supply voltage of 3.15 V supplied from another regulator than the one for the preamplifier (not explicitly shown). The active detuning signal levels are 7 V and -5 V. The high threshold voltage is chosen as 1 V and the low threshold voltage to 2 V. By choosing R5 (or R2) in Fig. B.4 the reference voltage and R2 (or R5) is determined. Knowing the reference voltage, it is a simple task to determine R3 and R4. Lastly, the switch Fig. B.3 is designed to have an approximate 4 μs turn-on time verified by Spice simulation. The auxiliary systems are seen in Fig. B.7. The auxiliary systems presented are not designed using non-magnetic components. Since the auxiliary systems are placed in an aluminium box, in the fringe field of the main magnet, far from region of interest, this has not posed an issue.

B.5.2 Preamplifier

The ^{13}C Larmor frequency at 3 T is 32.115 MHz. Hence the preamplifier is designed for this frequency. The printed circuit board (PCB) is fabricated using an in-house facility. A standard double sided FR4 is used with epsilon 4.3, copper thickness 35 um and thickness 1.6 mm. The design is seen in the bottom right of Fig. B.6. The

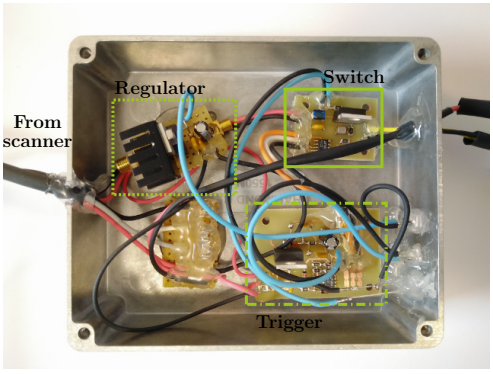

Figure B.7: Auxiliary systems consisting of the regulator, trigger and switch enclosed in an aluminium box. The size of the aluminium box is 120 mm x 100 mm x 35 mm.

fabricated PCB size is 37 mm x 26 mm.

The transistor used here is the Broadcom (formerly Avago) ATF54143. The choice of the transistor is in part due to showing the best noise performance of commercially available transistors. In part because it is an enhancement mode pHEMT. An enhancement mode pHEMT does not require a negative gate voltage to turn off. This is preferred because a negative gate voltage does not have to be generated from the single supply of the scanner. The capacitors used are PPI high-Q having an inherent tolerance of 5 %.

The bias voltage was chosen as 0.5 V which yields a fair trade-off between noise and gain of the transistor at both room and cryogenic temperature. The bias voltage is kept fixed for the room temperature and cryogenic measurements. The measured bias voltage is 0.54 V at room temperature.

The S-parameters are shown in Fig. B.8. The input reflection coefficient in Fig. B.8a shows that the preamplifier is highly mismatched. Even though the input impedance is highly mismatched the amplifier is matched primarily to decrease noise. The simulated and measured room temperature S_{11} does differ significantly when in this high mismatch regime. Further, at 77 K the mismatch is increased even further. The input reflection coefficient is seen to increase when cooled in Fig. B.8a. This is partly due to the decreased current draw. Partly that the transistor input impedance increases at lower temperatures. The reverse isolation in Fig. B.8b shows fair correlation between simulation and measurement. At 77 K the isolation is unchanged. Fig. B.8c shows the gain where the simulated and measured data at 296 K are well correlated. When cooled the gain decreases by approximate 5 dB. Having the bias voltage fixed the decrease in gain is expected at lower temperatures and can be mitigated by increasing the bias voltage. The output reflection coefficient also shows a fair correlation between simulation and measurement and a minor offset at 77 K.

The stability of the preamplifier is assessed using three different approaches. The first is to evaluate (B.3) from the measured S-parameters and is plotted in Fig. B.9. At room temperature the preamplifier is unconditionally stable both in simulation and measurement. However, when cryogenically cooled the μ-factor drops below one. Hence the preamplifier is conditionally stable/potentially unstable at 77 K. Since the preamplifier is potentially unstable, a second approach for determining stability is to measure the spectrum at the input (output) of the preamplifier while the output (input) is terminated by a short, open or load (the coil or 50 Ω). The measured spectrum shows no spurious signals indicating that the preamplifier is stable. In addition the current draw of the preamplifier is observed while the input and output is terminated by a short, open or load. When the current remains constant for all terminations, it

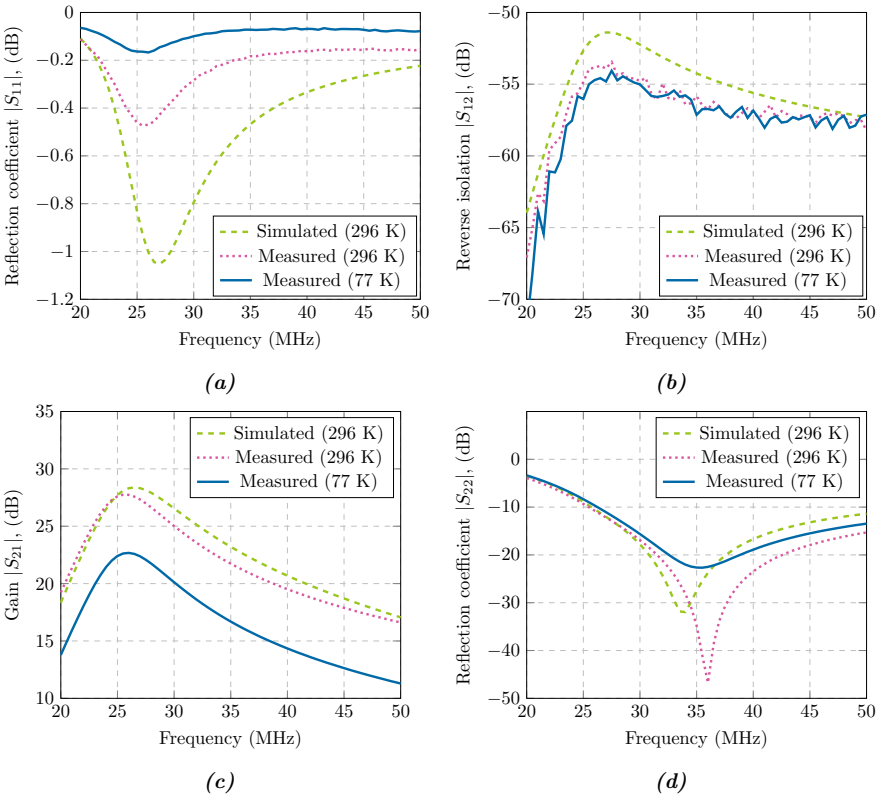

Figure B.8: Measured and simulated S-parameters of the room temperature and cryogenic preamplifier.

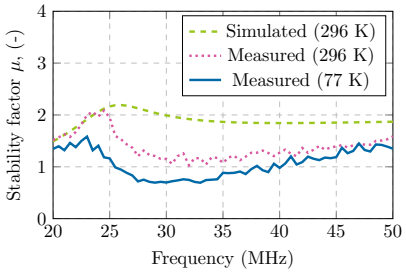

Figure B.9: Simulated and measured stability factor of the preamplifier.

is indirect indication that the preamplifier is stable. The last two approaches is basically a simplified source/load pull measurement focussed on stability. Hence, with the given combination of coil and matching circuit the preamplifier is stable. For this work, the preamplifier works sufficiently even with the potential instability. If unconditional stability is required a 200 Ω shunt resistor can be added to the output

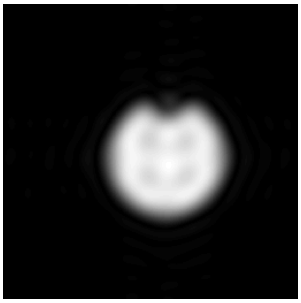

Figure B.10: Measured magnitude image of the phantom using the cryogenic preamplifier cooled to 77 K. The phantom is 37.5 mm in diameter. The field-of-view is 120 mm x 120 mm. The image is interpolated from 16-by-16 to 256-by-256 pixels using zero-filling.

of the preamplifier. This causes the μ-factor to rise above unity while the gain drops by 1 dB to 17 dB. Friis' formula for noise in cascaded two ports can be evaluated to determine if the gain drop is acceptable or not. For the application of MRI the gain drop is acceptable.

The measured noise is shown in Table B.1 at 32 MHz. Cooling the preamplifier with liquid nitrogen decreases the noise by 20.7 K, from 35.4 K to 13.7 K. The current draw of preamplifier is also lowered by 38 mA. The power consumption at room temperature is 147 mW and 33 mW at 77 K. The gain also decreases by 5 dB. This is expected due to freeze out and could be countered by increasing the biasing voltage. The noise simulated at room temperature yield 5.1 K relatively far from the 35.4 K. This discrepancy between simulated and measured noise performance is primarily because the transistor model is based on measurements only above 2 GHz and thus extrapolated downwards. Hence, the noise of the transistor model is not accurate when used at this, relatively, low frequency. Further, since the model is inaccurate, the noise matching might also be sub-optimal.

The required linearity is a 1 dB compression point better than -20 dBm [50, 51]. The 1 dB compression point of the preamplifier is measured at -13.8 dBm at both 296 K and 77 K. Hence the preamplifier complies with the linearity requirement.

The image obtained in the scanner is seen in Fig. B.10 using the cryogenic preamplifier. The image bears resemblance to an apple. This is due to the spherical phantom containing a small pocket of air. Due to the surface tension of the water this pocket of air seems to be impaled by another small pillar of liquid thus looking like the stem of an apple. In other words, the image looks as expected.

Table B.1: Measured Performance at 32 MHz

Temperature	Noise [K]	Current [mA]	Gain [dB]	SNR
296 K	35.4	49	23	365
77 K	13.7	11	18	399

B.6 Discussion

Although the frequency of operation was chosen at 32 MHz due to scanner availability all methods discussed apply generally to MRI. With little work the presented preamplifier can be redesigned to another frequency by altering the input and output matching circuits.

An aspect in choosing components is their magnetic properties. Capacitors are available from e.g. Johnson or PPI and non-magnetic inductors are available from e.g. Coilcraft. Acquiring non-magnetic resistors is a more tedious process resulting in either long lead times or high cost. Hence magnetic resistors are used in the biasing of the preamplifier. The transistor is also not available in a non-magnetic package. The magnetic packaging does disturb the main magnetic field, however the size of the components are small and they are placed approximately 30 cm away from the sample. No adverse effects were observed during imaging.

Concerning the conditional stability of the preamplifier at 77 K it is not inherently obvious looking at the S-parameter data. Since the input reflection coefficient approaches one the preamplifier must become more unstable as stated by (B.3). Lowering the gain, however, must increase stability. The reverse isolation stays constant and thus neither increase nor decrease stability. Hence, the decreased gain cannot offset the increase in input reflection coefficient. The conditionally stable preamplifier with a μ-factor of 0.75 implies that when $|S_{22}| = \mu$ the preamplifier will oscillate. The impedance present at the output of the preamplifier is known to be 50 Ω (or very close) because it is the impedance of the scanner RF ports. No problems with instability were observed.

The ATF54143 transistor was difficult to stabilize because it is designed primarily for 1-10 GHz operation. Thus ensuring low frequency stability was difficult because the inherent gain in the transistor rises rapidly at lower frequencies. Hence internal feedback in the transistor cause oscillation unless the gain is lowered. The stability of the preamplifier is highly dependent on the layout. Especially parasitic inductance between source and ground can cause high frequency instability. Other low frequency transistors are not as prone to oscillation at high frequency. However, none were

found that showed decent noise performance. Further, it is vital that the output and input are physically separated to not create a feedback path which cause instability.

The noise performance of the preamplifier is enhanced when cooled as expected. The relative SNR increase is approximately 8 % when using a room temperature coil. However, as coil designs move towards cryogenic operation the noise of the preamplifier becomes increasingly dominant. Thus, if the coil is also cooled the SNR increase from using a cryogenic preamplifier becomes higher.

It is likely that even better noise performance can be achieved by more appropriate matching. This requires the characterization of the four noise parameters in order to find the optimum noise match. Indeed it is simpler to simulate the optimal noise match. However, the transistor model is extrapolated from 2 GHz and downward and was not capable of simulation at 77 K. Especially the transistor model needs revision for lower frequency and lower temperature. The passive components are also not characterized at cryogenic temperatures. Thus allowing simulations at cryogenic temperatures are contingent on proper characterization of the components used for design. Hence better models for cryogenic design is in demand.

B.7 Conclusion

The preamplifier design was based on the ATF54143 enhancement mode pHEMT using a common source topology. Bipolar transistors should generally not be considered for cryogenic work. Indeed HBTs can be made to work at cryogenic temperatures but requires custom design. On the other hand field effect transistors are much more likely to work at cryogenic temperatures. The results show that at liquid nitrogen the noise is 13.7 K whereas the gain drops to 18 dB from 23 dB at room temperature. This is expected due to the freeze out of carriers and can be corrected by increasing the bias voltage at the transistor gate. The SNR is increased from 365 to 399 using the cryogenic preamplifier with a room temperature coil.

An auxiliary system consisting of voltage regulator, trigger and switch circuits were presented. The supply regulator was designed using a readily available LM317 and ensures a stable, filtered supply voltage for the preamplifier. The trigger and switch ensures that the preamplifier does not break during transmission by switcing off the supply voltage to the preamplifier.

Moving towards the ultimate limit of detection cryogenic probes are seeing the light of day. Hence the noise contribution from the preamplifiers becomes more important. This work described the pitfalls of preamplifier design and implementation for

cryogenic operation, including necessary auxiliary systems.

References

[1] S. E. Day, M. I. Kettunen, F. A. Gallagher, D.-E. Hu, M. Lerche, J. Wolber, K. Golman, J. H. Ardenkjaer-Larsen, and K. M. Brindle, "Detecting tumor response to treatment using hyperpolarized 13C magnetic resonance imaging and spectroscopy," *Nat. Med.*, vol. 13, no. 11, pp. 1382–1387, nov 2007.

[2] S. J. Nelson, J. Kurhanewicz, D. B. Vigneron, P. E. Z. Larson, A. L. Harzstark, M. Ferrone, M. van Criekinge, J. W. Chang, R. Bok, I. Park, G. Reed, L. Carvajal, E. J. Small, P. Munster, V. K. Weinberg, J. H. Ardenkjaer-Larsen, A. P. Chen, R. E. Hurd, L.-I. Odegardstuen, F. J. Robb, J. Tropp, and J. A. Murray, "Metabolic imaging of patients with prostate cancer using hyperpolarized [1-13C]pyruvate." *Sci. Transl. Med.*, vol. 5, no. 198, pp. 1–22, aug 2013.

[3] D. Erdogmus, E. G. Larsson, R. Yan, J. C. Principe, and R. Fitzsimmons, "Measuring the signal-to-noise ratio in magnetic resonance imaging: a caveat," *Signal Processing*, vol. 84, pp. 1035–1040, 2004.

[4] R. E. Hurd, Y.-F. Yen, A. Chen, and J. H. Ardenkjaer-Larsen, "Hyperpolarized 13C metabolic imaging using dissolution dynamic nuclear polarization." *J. Magn. Reson. Imaging*, vol. 36, no. 6, pp. 1314–1328, dec 2012.

[5] E. Y. Chekmenev, "MRI Hyperpolarization and Molecular Imaging," *Newsl. SNMMI*, vol. 7, no. 3, pp. 2–4, 2013.

[6] C.-N. Chen and D. I. Hoult, *Biomedical Magnetic Resonance Technology*, 1st ed. Institute of Physics Publishing, 1989.

[7] D. G. Nishimura, *Principles of Magnetic Resonance Imaging*, 1st ed. lulu.com, 2010.

[8] H. Kovacs, D. Moskau, and M. Spraul, "Cryogenically cooled probes - a leap in NMR technology," *Prog. Nucl. Magn. Reson. Spectrosc.*, vol. 46, pp. 131–155, 2005.

[9] L. Darrasse and J. Ginefri, "Perspectives with cryogenic RF probes in biomedical MRI," *Biochimie*, vol. 85, pp. 915–937, 2003.

[10] Bruker MRI CryoProbe. [Online]. Available: https://www.bruker.com/products/mr/preclinical-mri/mri-cryoprobes.html

[11] W. Kwok, Z. You, and J. Zhong, "Cryogenically cooled phased array rf receiver coil for magnetic resonance imaging," 2003, uS Patent App. 10/405,633.

[12] C.-l. Lim, P. Serano, and J. L. Ackerman, "Pre-amplifiers for a 15-Tesla magnetic resonance imager," in *IEEE Int. RF Microw. Conf.*, 2013, pp. 295–299.

[13] S. H. Yadav, "Design of Low Noise Amplifier For MRI Scanner using Cascode Technology," *Int. J. Innov. Res. Comput. Commun. Eng.*, pp. 1504–1510, 2017.

[14] F. D. Doty, G. Entzminger, J. Kulkarni, K. Pamarthy, and J. P. Staab, "Radio frequency coil technology for small-animal MRI," *NMR Biomed.*, vol. 20, no. 3, pp. 304–325, 2007.

[15] *WMA32C: 32.19 MHz Low Noise Low Impedance Preamplifier*, WanTcom Inc., 2013, rev. B.

[16] Teledyne e2v (UK) Ltd. [Online]. Available: http://www.e2v.com/

[17] Hi-Q.A. Inc., Datasheet H1021531. [Online]. Available: http://www.hiqa.com/H1021531-DataSheet.pdf

[18] M. W. Pospieszalski, "Extremely low-noise amplification with cryogenic FETs and HFETs: 1970-2004," *IEEE Microw. Mag.*, vol. 6, no. 3, pp. 62–75, 2005.

[19] J. J. Bautista, "Cryogenic, Low-Noise High Electron Mobility Transistor Amplifiers for the Deep Space Network," Tech. Rep., 1993.

[20] U. Kleine, J. Bieger, and H. Seifert, "A Low-Noise CMOS Preamplifier Operating at 4.2 K," *IEEE J. Solid-State Circuits*, vol. 29, no. 8, pp. 921–926, 1994.

[21] R. J. Prance, A. P. Long, T. D. Clark, and F. Goodall, "UHF ultra low noise cryogenic FET preamplifier," *J. Phys. E.*, vol. 15, pp. 101–104, 1982.

[22] A. T. Lee, "A low-power-dissipation broadband cryogenic preamplifier utilizing GaAs MESFETs in parallel," *Rev. Sci. Instrum.*, vol. 64, pp. 2373–2378, 1993.

[23] S. Montazeri, W.-t. Wong, A. H. Coskun, and J. C. Bardin, "Ultra-Low-Power Cryogenic SiGe Low-Noise Amplifiers: Theory and Demonstration," *IEEE Trans. Microw. Theory Tech.*, vol. 64, no. 1, pp. 178–187, 2016.

[24] J. Koivuniemi and M. Krusius, "Noise temperature of cryogenic FET amplier with high-Q resonator," *Phys. B*, vol. 284-288, pp. 2149–2150, 2000.

[25] P. Styles and N. F. Soffe, "A High-Resolution NMR Probe in Which the Coil and Preamplifier Are Cooled with Liquid Helium," *J. Magn. Reson.*, vol. 60, pp. 397–404, 1984.

[26] M. G. Richards, A. R. Andrews, C. P. Lusher, and J. Schratter, "Cryogenic GaAs FET amplifiers and their use in NMR detection," *Rev. Sci. Instrum.*, vol. 57, pp. 404–409, 1986.

[27] G. Fontana, R. Mezzena, S. Vitale, and M. Cerdonio, "Improved Sensitivity of Planar Microwave Biased RF-SQUIDs using a Cryogenic HEMT Preamplifier," *IEEE Trans. Appl. Supercond.*, vol. 3, no. 1, pp. 1820–1823, 1993.

[28] R. Mathur, R. W. Knepper, and P. B. O'Connor, "A Low-Noise Broadband Cryogenic Preamplifier Operated in a High-Field Superconducting Magnet," *IEEE Trans. Appl. Supercond.*, vol. 18, no. 4, pp. 1781–1789, 2008.

[29] J. G. Heteren, N. Fenzi, T. W. James, and L. C. Bourne, "Thin Film High Temperature Superconductor RF Coil and Cryogenic Preamplifier for Low Field MRI," in *IEEE Nucl. Sci. Symp. Med. Imaging Conf.*, 1993, pp. 1708–1712.

[30] F. Resmer, H. C. Seton, and J. M. S. Hutchison, "Cryogenic receive coil and low noise preamplifier for MRI at 0.01 T," *J. Magn. Reson.*, vol. 203, pp. 57–65, 2010.

[31] J. D. Sanchez-heredia, E. Søvsø, S. Hansen, C. Laustsen, V. Zhurbenko, and J. H. Ardenkjær-larsen, "Low-Noise Active Decoupling Circuit and its Application to 13C Cryogenic RF Coils at 3 T," *Tomography*, vol. 3, no. 1, pp. 60–66, 2017.

[32] *LM317 3-Terminal Adjustable Regulator (SLVS044X)*, Texas Instruments, 2016.

[33] C. Hu, *Modern Semiconductor Devices for Integrated Circuits*. Prentice Hall, 2010. [Online]. Available: https://people.eecs.berkeley.edu/~hu/

[34] R. Pierret, *Semiconductor Device Fundamentals*. Addison-Wesley, 1996.

[35] ——, *Advanced Semiconductor Fundamentals*, 2nd ed. Pearson, 2003.

[36] B. Lengeler, "Semiconductor devices suitable for use in cryogenic environments," *Cryogenics*, vol. 14, pp. 439–447, 1974.

[37] J. D. Cressler, S. Member, J. H. Comfort, A. Member, E. F. Crabbc, G. L. Patton, S. Member, J. M. C. Stork, S. Member, J. Y. Sun, S. Member, and B. S. Meyerson, "On the Profile Design and Optimization of Epitaxial Si- and SiGe-Base Bipolar Technology for 77 K Applications - Part I: Transistor DC Design Considerations," *IEEE Trans. Electron Devices*, vol. 40, no. 3, pp. 525–541, 1993.

[38] J. D. Cressler, S. Member, E. F. Crabbc, J. H. Comfort, A. Member, J. M. C. Stork, S. Member, J. Y. Sun, and S. Member, "On the Profile Design and Optimization of Epitaxial Si- and SiGe-Base Bipolar Technology for 77 K Applications - Part II: Circuit Performance Issues," *IEEE Trans. Electron Devices*, vol. 40, no. 3, pp. 542–556, 1993.

[39] J. Cressler, "Operation of SiGe bipolar technology at cryogenic temperatures," *J. Phys.*, vol. 4, pp. C6–101–C6–110, 1994.

[40] E. F. Crabbe, G. L. Patton, J. M. C. Stork, J. H. Comfort, B. S. Meyerson, and J. Y. C. Sun, "Low temperature operation of Si and SiGe bipolar transistors," in *International Technical Digest on Electron Devices*, Dec 1990, pp. 17–20.

[41] E. F. Crabbe, D. L. Harame, B. S. Meyerson, J. M. C. Stork, and J. Y. C. Sun, "Low-temperature operation of sige p-n-p hbts," *IEEE Trans. Electron Devices*, vol. 39, no. 11,

pp. 2638–2639, Nov 1992.

[42] S. Weinreb, J. C. Bardin, and H. Mani, "Design of Cryogenic SiGe Low-Noise Amplifiers," *IEEE Trans. MTT*, vol. 55, no. 11, pp. 2306–2312, 2007.

[43] M. Pospieszalski, S. Weinreb, and R. Norrod, "FET's and HEMT's at Cryogenic Temperatures- Their Properties and Use in Low-Noise," *IEEE Trans. MTT*, vol. 36, no. 3, pp. 552–560, 1988.

[44] H. Meschede, J. Albers, R. Reuter, J. Kraus, D. Peters, W. Brockerhoff, and F. J. Tegude, "Rf investigations on hemt's at cryogenic temperatures down to 20 k using an on-wafer microwave measurement setup," in *European Microwave Conference*, vol. 1, Sept 1992, pp. 151–156.

[45] D. H. Johansen, J. D. Sánchez-Heredia, V. Zhurbenko, and J. H. Ardenkjær-Larsen, "Practical Aspects of Preamplifier Designs for 13C Imaging," in *Proc. Intl. Soc. Mag. Reson. Med. 25*, 2017.

[46] M. L. Edwards and J. H. Sinsky, "A new criterion for linear 2-port stability using a single geometrically derived parameter," *IEEE Trans. MTT*, vol. 40, no. 12, pp. 2303–2311, Dec 1992.

[47] J. Rollett, "Stability and Power-Gain Invariants of Linear Twoports," *IRE Transactions on Circuit Theory*, vol. 9, no. 1, pp. 29–32, March 1962.

[48] F. Teyssandier and D. Prêle, "Commercially Available Capacitors at Cryogenic Temperatures," in *WOLTE9*, Jun. 2010.

[49] R. D. Norrod, "Cryogenic Measurements of Surface Mount Multi-layer Ceramic Chip Capacitors," National Radio Astronomy Observatory, Electronics Division, Green Bank, West Virginia, Tech. Rep. 214, March 2010.

[50] R. Behin, J. Bishop, and R. M. Henkelman, "Dynamic range requirements for MRI," in *Proc. Intl. Soc. Mag. Reson. Med. 13*, 2005.

[51] ——, "Dynamic range requirements for MRI," *Concepts in Magnetic Resonance Part B: Magnetic Resonance Engineering*, vol. 26B, no. 1, pp. 28–35, 2005.

Paper C

PIN Diode Driver for NMR and MRI

D. H. Johansen, M. M. Albannay, J. R. Petersen, V. Zhurbenko, and J.H. Ardenkjær-Larsen

Journal of Magnetic Resonance, vol. 300, pp. 114-119, Mar. 2019.

The layout has been revised.

Abstract

Designing custom coils for magnetic resonance systems, such as nuclear magnetic resonance (NMR) spectrometers and magnetic resonance imaging (MRI) scanners, often entails using non-standard configurations of the transmit-receive (T/R) switch and Q-spoiling circuits. The built-in drivers of commercial NMR and MRI systems are, typically, only reconfigurable within a narrow application range (if at all). Thus, the built-in driver may not be able to properly control the custom T/R switches and Q-spoiling circuits when using custom built coils. We present a PIN diode driver which functions in both an MRI scanner and NMR spectrometer. The PIN diode driver is based on readily available discrete components and achieves switching times for the reverse and forward bias states (transmit on and off) of 2 μs and 0.4 μs respectively. Hence, this work enables a higher degree of customization of the RF switching circuits in an MR system and is potentially of interest for designers of custom coils for both NMR spectrometers and MRI scanners.

C.1 Introduction

In a magnetic resonance (MR) system it is vital to have reliable switching between transmit and receive states of the radio frequency (RF) front-end. The majority of such circuits for switching in an MR system are based on positive-intrinsic-negative (PIN) diodes [1–4]. Micro-electromechanical systems (MEMS) [5] and transistor [6] based switches are, however, slowly emerging as an alternative. The two most commonly used applications for PIN diodes are transmit-receive (T/R) switches and Q-spoiling circuits (also referred to as active decoupling or active detuning circuits). T/R switches and Q-spoiling circuits have been discussed in depth in [1, 7]. However, the treatment of PIN diode driver circuits (just *driver* moving forward) for MR systems have largely escaped scrutiny, despite the fact that drivers are present in all nuclear magnetic resonance (NMR) spectrometers and magnetic resonance imaging (MRI) scanners. Even though drivers are readily available in different commercial systems, when designing custom coils, a higher degree of flexibility in controlling, for example, the T/R switch and Q-spoiling circuits is often imperative for optimal performance. This work discusses the requirements for a driver in an MR system and presents a design capable of μs switching for both forward and reverse bias.

A PIN diode is made by sandwiching an insulating material between a P- and N-doped semiconductor. At RF and microwave frequencies a PIN diode acts as a non-linear

current-controlled resistor [8]. When forward biased a PIN diode achieves resistances in the order of 0.1-0.5 Ω (depending on the forward current) with a parasitic parallel capacitance of approximately 0.1-2 pF (dictated by the size of the PIN diode). In reverse bias, the resistance of the PIN diode increases to several kΩ. The exact reverse bias resistance is highly dependent on the reverse voltage. At 0 V reverse bias the resistance is usually in the range of 5-10 kΩ [9]. The primary problem when having to switch PIN diodes is an inherent non-linear charge storage characteristic resulting in having to source or sink a large current when transitioning from forward to reverse bias or vice-versa.

Drivers are available commercially for cellular applications where the current sourcing capability is limited at 100 mA with a switching speed of up to 1650 ns [10]. [11, 12] describe an implementation, which is capable of delivering peak currents in excess of 1 A at switching times of 15 ns. In [13], a driver based on operational amplifier (opamp) technology is presented showing switching times in the order of 200 ns. Forlani and Fresia [14] describe a driver capable of delivering 10 mA to a PIN diode with a switching time of 1.6 ns. Harvey [15] presents a design capable of delivering 120 mA at a switching time of 6 ns. van Niekerk and van der Walt [16] show a design with 200 mA current sourcing. The switching time is up to 7 μs. In [17] the presented driver switches in 3 μs with a current of 30 mA. For MRI, a design is presented by [18]. The design is based on [19] and is capable of switching in approximately 4 us. Brunner et al. [20] presents a complete differential T/R switch, including a differential driver for NMR and MRI. The driver is based on the opamp design in [13] and is capable of sourcing up to 1.8 A with a switch time of approximately 700 ns.

Two key issues with the currently available drivers are: 1) The drivers require a specific series resistor for a given output voltage (which determines the current through the PIN diode). Since the resistor determines the output voltage, the sourcing current is vulnerable to changes in the knee voltage of the PIN diode. For instance, given a certain Q-spoiling switch employing multiple PIN diodes in series, the resistance regulating the biasing current needs to be recalculated and changed in the driver. 2) Low and/or unclear current sourcing and sinking capabilities.

In this work, the two problems described above are addressed by designing a driver, which features a reconfigurable regulated forward bias current between 65 mA and 1.4 A, with a reverse bias switching time of 0.4 μs.

C.2 Methods

For the driver to work in both an NMR spectrometer and MRI scanner it is required that the driver can trigger on both a voltage-to-voltage and current-to-voltage input (transmit on-to-off). The voltage-voltage input is typically supplied from a microprocessor (e.g. 5 V and 0 V for the transmit on and off state respectively) and the current-voltage input is the Q-spoiling signal from the MRI scanner (e.g. 100 mA current forward and -5 V reverse bias). When the input to the driver transitions from low to high, the output of the driver needs to transition from a reverse bias of -5 V to a forward bias between 100-500 mA and vice versa. Even though the driver is applicable to both NMR and MRI systems, it is primarily designed for an MRI system where a single positive supply of 10 V is available. We target switching times from forward to reverse bias in under 1 μs and from reverse to forward bias below 10 μs.

C.2.1 Driver Circuit

The schematic of the driver is shown in Fig. C.1. The first part of the driver is a buffer ensuring better input jitter stability. The optional diodes are required when triggering the forward bias state of the driver using a current rather than a voltage (required when the Q-spoiling signal from the scanner has to trigger the driver). The buffer triggers when Vin transitions between approximately 0.25 V and 0.5 V. The positive level shifter inverts the output of the buffer and controls the positive field effect transistor (FET) driver which controls Q11. Q11 is an IRLIB9343 P-channel metal oxide semiconductor FET (MOSFET) and is used as a high side switch. The negative level shifter likewise inverts the signal from the buffer and controls the negative FET driver, which toggles Q14. Q14 is an IRF530 N-channel MOSFET that is operated as a low side switch. To ensure that the sourcing current of the driver is independent of the load connected to Vout, a discrete current limiter is used.

Buffer

The buffer consists of a Schmitt trigger ensuring that the PIN driver does not flicker if noise is present on Vin. It is a standard non-inverting topology using the LT1720 comparator (U1A), which is a rail-to-rail and single supply OpAmp. When Vin transitions above an upper threshold voltage V_{h} the buffer output $V_{\mathrm{oh}} = \mathrm{Vcc}$. Vice versa, when Vin transitions below a lower threshold V_{l}, $V_{\mathrm{ol}} = 0$. R1, R2, R3, and R4

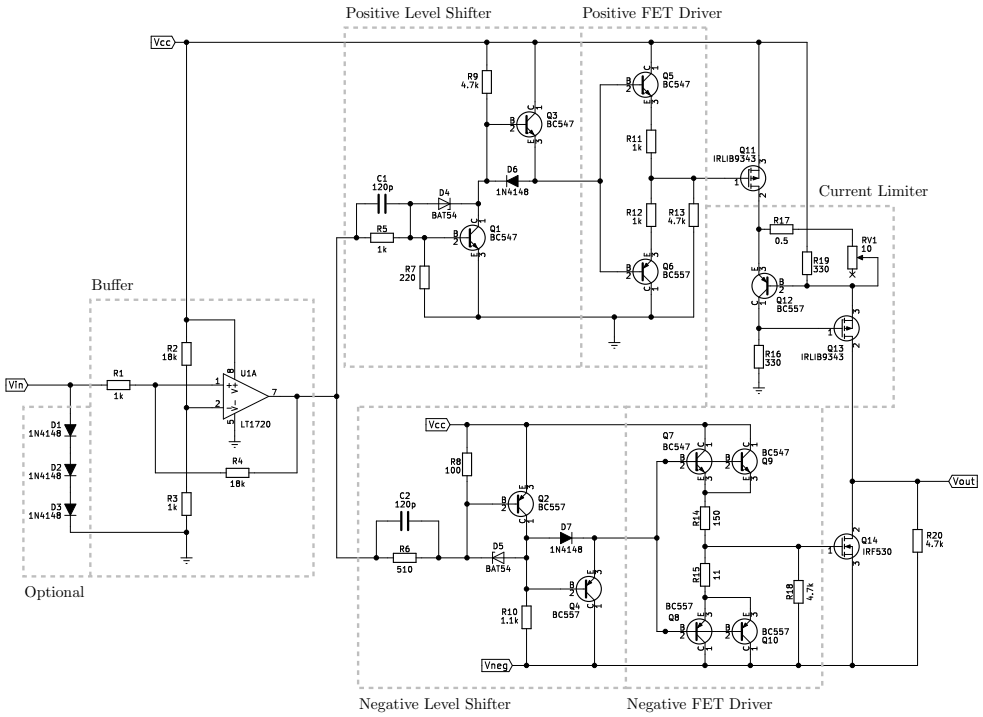

Figure C.1: Schematic of the PIN diode driver.

are found by solving [21]

$$R1 = \frac{R_4 \left(V_\mathrm{h} - V_\mathrm{l}\right)}{V_\mathrm{oh} - V_\mathrm{ol}}, \tag{C.1}$$

$$V_\mathrm{ref} = \frac{V_\mathrm{h} V_\mathrm{ol} - V_\mathrm{l} V_\mathrm{oh}}{V_\mathrm{h} - V_\mathrm{l} - V_\mathrm{oh} + V_\mathrm{ol}}, \tag{C.2}$$

where V_ref is the voltage at pin 2 of U1A. V_ref is defined by the voltage division between R2 and R3. Hence, the threshold voltage are approximately $V_\mathrm{h} = 0.5$ V and $V_\mathrm{l} = 0.25$ V.

Level Shifters

The level shifters convert the output of the buffer (pin 7 of U1A) from $\{0, \mathrm{Vcc}\}$ V to $\{\mathrm{Vcc}, 0\}$ V or $\{\mathrm{Vcc}, \mathrm{Vneg}\}$ V for the positive and negative level shifter respectively. Hence, the level shifters also work as inverters.

When the buffer output voltage transitions low, current runs through the base of Q2 and R6. In turn, the voltage at the base of Q4 rises, forward biasing D5, and

subsequently dividing the current through R6 between D5, R8, and the base of Q2. Because D5 is a Schottky diode, having a lower knee voltage (0.4 V) than the transistor (0.7 V), it defines the operating point of Q2 and thus ensures that Q2 is not in saturation. Hence, D5 ensures faster switching because Q2 is not in saturation. Further, D5 also mitigates the variance of the conduction voltage of Q2 and thus ensures a uniform performance of the level shifter across multiple devices. D7 protects Q4 by ensuring that the base emitter voltage does not exceed the reverse knee voltage of Q4 (5 V). When the output of the buffer goes high, C2 discharges into the base of Q2 and D5, Q2 is closed (swiftly due to C2), R10 pulls the base of Q4 to Vneg, and Q4 thus opens and pulls down the output of the negative level shifter to Vneg minus the base emitter voltage of Q4 (0.7 V).

The positive level shifter works the same as the negative level shifter but is 'flipped'. When the output of the buffer is high, C1 discharges primarily into the base of Q1 turning it on quickly. Current thus flows through R5 and the base of Q1, opening Q1, pulling down the base of Q3, and pulling down the output of the positive level shifter to ground. When the buffer output drops to zero Q1 is turned off, R9 pulls the base of Q3 to Vcc, Q3 is then turned on and the output of the positive level shifter rises to Vcc minus the base emitter voltage of Q3.

FET Drivers

The FET drivers are standard BJT push-pull emitter followers based on the N-type BC547 and P-type BC557 transistors. In the positive FET driver, R11 limits the in-rush current to the gate of Q11 and thus controls the switch off time of Q11. R12 limits the out-rush current from the gate of Q11 determining the turn on time of Q11. In the negative FET driver, R15 determines the out-rush current from the gate of Q14 and hence the turn off time of Q14. R14 limits the in-rush current to the gate of Q14 and hence the turn on time of Q14. Two parallel transistors is utilized on the high (Q7 and Q9) and low (Q8 and Q10) side of the negative FET driver because the peak currents when switching a physically large FET driven hard into saturation can exceed the maximum safe operating current of the BJ547 and BJ557 transistors.

Current Limiter

If R19 is excluded, the current limiter is fairly well-known and not very fast. As the voltage on the drain of Q11 rises the source voltage of Q13 also rises and thus turns on Q13, because the gate of Q13 is grounded via R16. As Q13 turns on and draws current through R17 and RV1 the emitter base voltage of Q12 approaches

the conduction voltage of Q12. As Q12 starts to conduct, current in R16 increases, increasing the gate voltage of Q13 and again decreasing the current in Q13. Hence, the regulated current output from the source of Q13 is defined by Ohm's law as

$$I_{\text{out}} = \frac{V_{\text{eb}}^{(\text{Q12})}}{\text{R17} + \text{RV1}}. \tag{C.3}$$

The BC557 has an approximate conduction voltage of 0.7 V and thus the minimum and maximum current is 67 mA and 1.4 A respectively. R19 is added to prevent Q13 from going out of conduction (by adding a small quiescent current of approximately 10 mA) and thus decrease the turn on time of the current limiter.

C.2.2 Power Supply

The driver circuit requires three voltages: Vcc, Vneg, and ground. The schematic in Fig. C.2 shows the power supply used for the driver. To generate Vcc, Vsup is regulated to 5 V using an LM7805 linear regulator (U3). The minimum and maximum input voltage to U3 is 7 V and 25 V respectively. Because the driver is designed to operate on a single supply from an MRI scanner an LTC3261 charge pump (U2) is used. U2 converts Vsup to -Vsup on VI of U4 and operates from a Vsup ranging from 4.5 V to 32 V with a maximum of 100 mA. The negative voltage from U2 is regulated to -5 V using an LM7905 linear regulator (U4) which operates with an input voltage from -7 V to -25 V.

C.2.3 Implementation

The driver and power supply is implemented on a double sided FR-4 substrate with a thickness of 1.5 mm, relative permittivity of approximately 4.2, and copper thickness of 35 um. The layout is made in KiCad (files available online) and manufactured using an in-house process. Our in-house process does not feature plated through holes. Vias are made using 0.6 mm diameter copper rivets. The complete driver is seen in Fig. C.3.

C.2.4 Bench Characterization

The bench characterization consists of measuring the on and off switching times of the driver when loaded with a number of PIN diodes at different forward bias currents.

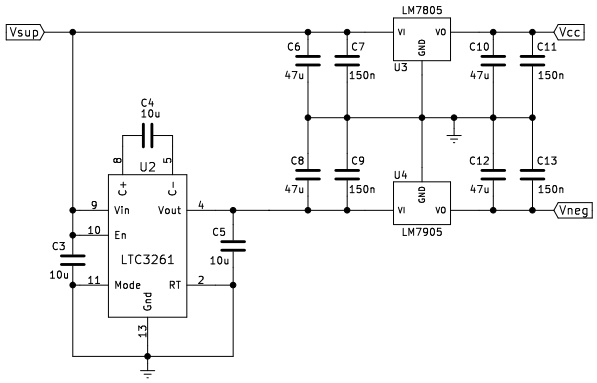

Figure C.2: Schematic of the power supply for the PIN diode driver.

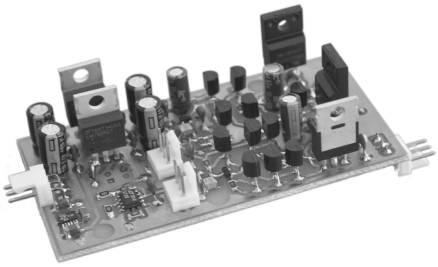

Figure C.3: Picture of the PIN diode driver.

This is accomplished using an arbitrary waveform generator to trigger the driver and an oscilloscope featuring at least two channels. One channel of the oscilloscope is connected to Vin along with the output of the arbitrary waveform generator. The second channel of the oscilloscope is connected to Vout. It is vital that the grounding lines of the arbitrary waveform generator and the oscilloscope channels are kept as short as possible to prevent ringing.

C.2.5 Imaging and Spectroscopy Experiments

Imaging of ^{13}C was conducted on a 3 T clinical scanner (GE Healthcare MR750). A cylindrical phantom filled with ethylene glycol mixed with 17 g/L NaCl was used (to provide loading). The length of the sample is 10 cm and it has a diameter of 3 cm. A chemical shift imaging (CSI) sequence was used with a repetition time of 250 ms, slice thickness of 4 cm, and field-of-view (FOV) of 14-by-14 cm in the axial plane. The transmit coil is a clamshell type from RAPID Biomedical. The receive coil is a self-made surface coil which is rectangular with a length and width of 6 and 8 cm respectively. The edges have been metered at a length of 1 cm. The unloaded

and loaded Q-factors are 381 and 172, respectively. Hence, the unloaded to loaded Q-factor is approximately 2.2.

Solid-state dynamic nuclear polarization (DNP) NMR experiments were conducted in a 6.7 T polarizer magnet using a Varian DirectDrive 400 spectrometer. The spectrometer's T/R switch is equipped with three MA4P404-28 PIN diodes biased between +5V and -15V (with the built-in driver) during transmission and reception mode, respectively. A current of 100 mA biases each diode whilst pulsing thereby minimizing the insertion loss to the sample coil and maximizing receiver preamplifier isolation. Centered in an RF coil is a 50 μL sample of 14 M [1-^{13}C]pyruvic acid containing 30 mM of the trityl radical AH111501. The RF coil exhibits an unloaded Q-factor of approximately 45. Due to very low sample loading ($\tan\delta < 0.0002$), the unloaded to loaded Q-factor is approximately 1. The sample was cooled in a helium bath to 1.4 K and irradiated with 187.96 GHz microwaves. The microwave source is based on an actively multiplied Gunn diode oscillator from Quinstar Technology and a 200X2R4 frequency doubler from VDI. Microwave irradiation is seized after 0.5 h to acquire a free induction decay (FID). A total of 20 FIDs were acquired using both the Varian and self-built driver. The data is acquired using a spectral bandwidth of 5 MHz, a flip angle of 0.36 degrees, and 2048 number of points.

C.3 Results

Fig. C.4 shows the measured switching times of the driver on the bench utilizing different forward bias currents and number of PIN diodes in series. Switching the driver to forward bias, when a single PIN diode is connected to the output, when sourcing 100 mA, 250 mA, and 500 mA results in a steady state after approximately 2 μs (Fig. C.4a). Switching the driver to reverse bias with a single PIN diode connected to the output, for the three sourcing currents mentioned above, results in a steady state after approximately 0.4 μs which is achieved at 500 mA (Fig. C.4b). At 100 mA the reverse bias steady state is reached in approximately 0.28 μs.

The forward bias switching time when sourcing 100 mA, but adding PIN diodes in series, is seen in Fig. C.4c. Up to four series PIN diodes has been added resulting in steady state switch on times of approximately 1.3 μs, 1.5 μs, 1.7 μs, and 2.1 μs when using 1, 2, 3, and 4 series connected PIN diodes on the output of the driver respectively. As expected, the steady state voltage rises with additive knee voltages of the PIN diodes: 0.7 V, 1.4 V, 2.1 V, and 2.8 V for 1, 2, 3, and 4 series connected PIN diodes. As the overshoot voltage approaches Vcc the linear increase in switching time breaks down and the switching time increases. The reverse bias switching time

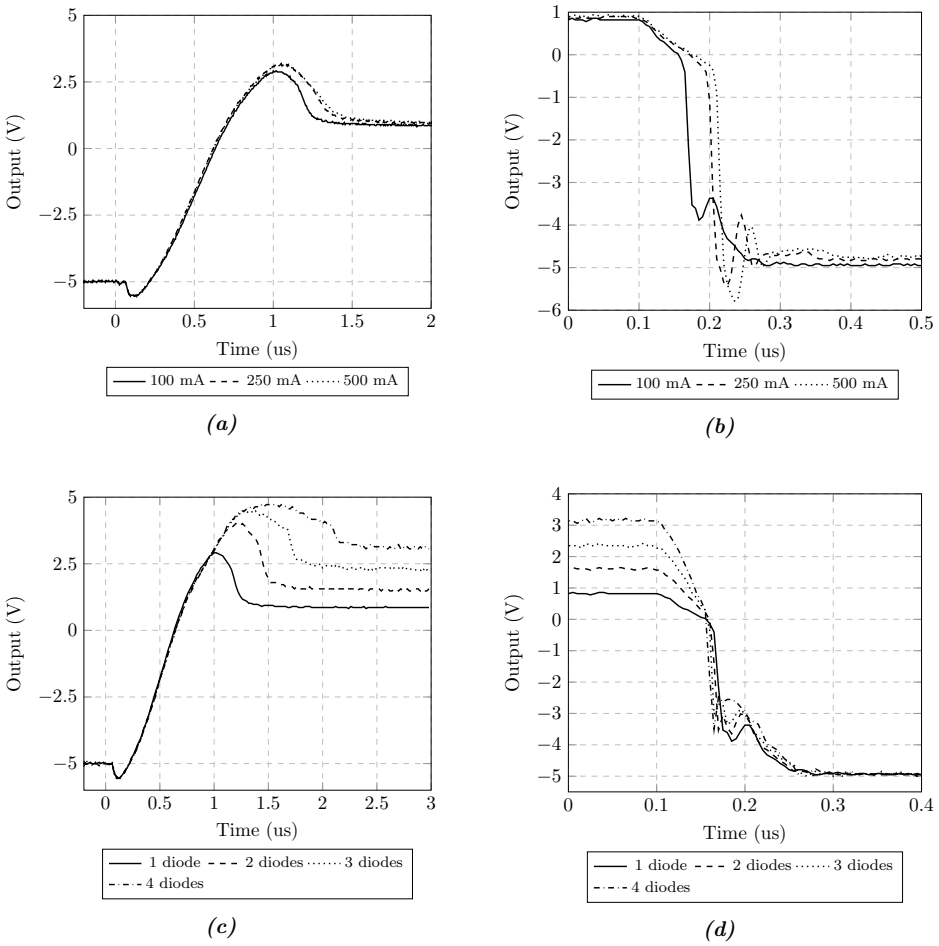

Figure C.4: Bench measurements showing the switch on and off timing of the PIN diode driver. (a) shows the switch on timing. (b) shows the switch off timing.

when using multiple series diodes is seen in Fig. C.4d. It is found that the reverse bias switching time is independent on the number of series connected PIN diodes (at least up to 4) showing an almost constant reverse bias switching time of approximately 0.27 μs.

Imaging results are seen in Fig. C.5. Using the scanner's built-in driver an SNR of approximately 42 was measured. Using the driver presented here an SNR of approximately 43 was measured. Hence, there is no significant difference between the two measurements.

The first 10 μs of the measured FID using the spectrometer is shown in Fig. C.6. No significant difference between the two measurements are observed, exhibiting an

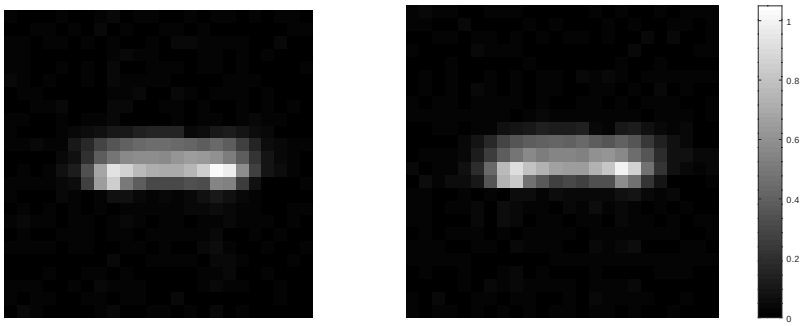

(a) *(b)*

Figure C.5: Scanner measurement showing an image of the cylindrical phantom with a) the scanner's built-in driver and b) the driver presented in this work.

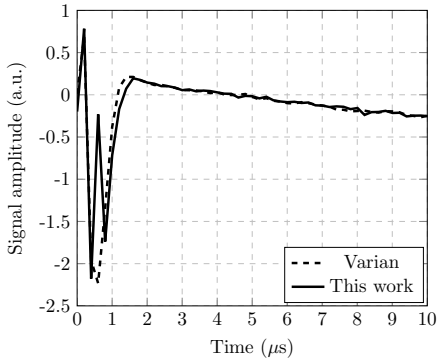

Figure C.6: Measured FID (first 10 μs) using the built-in PIN driver of the Varian spectrometer and the one presented in this work.

approximate switching time of 1.5 μs. The SNR is 1256 and 1331 using the Varian and self-built driver, respectively. This amounts to an approximately 6 % increase when using the self-built driver.

C.4 Discussion

It was expected that the imaging experiments should show no significant difference in SNR when using the built-in or self-built driver. This observation is only true when using the CSI sequence, or other sequences with similar timing requirements. To extend the usage of the driver to more timing critical applications, the driver was also applied to a solid-state spectroscopy experiment. Here, no significant SNR difference was observed either. Hence, even though the self-built driver does not supply a -

15 V negative supply compared to the Varian, similar SNR values are achieved. This indicates that the self-built driver is indeed as good as both the built-in driver in the MRI scanner and the NMR spectrometer. The driver presented in this work does not enable e.g. zero echo time imaging, as this would, likely, require a complete redesign of the T/R switch. The primary objective of this work was, however, to enable a higher degree of flexibility in utilizing custom T/R switches and Q-spoiling circuits.

The switching time is in this work defined using the MA4P1250NM PIN diode connected directly to the output of the driver. Hence, required circuitry of a T/R switch or Q-spoiling circuit such as feeding inductor(s) and decoupling capacitor(s) are not included in the switching time characterized on the bench. We believe that the switching time, when characterized on the bench using a PIN diode while omitting the use of other circuitry, shows the capability of the driver to handle the non-linear current sourcing and sinking of the PIN diode. Even though the switching time is not truly characterized only by the PIN diode it does represent a best case scenario. It is important to recognize that by omitting the use of feed inductors and decoupling capacitors on the bench, also eliminates ringing and the potential use of a snubber circuit. A snubber circuit typically consists of a series resistor, shunt capacitor filter which filters the ringing above certain frequencies. It also slows down the switching time of the driver. The snubber circuit is omitted in this work, but is thoroughly described in [22], and can easily be added to the driver.

The forward bias switching time of the driver can be lowered by further increasing the supply voltage to the positive level shifter, positive FET driver, and Q11. When the driver switches to forward bias, due to the current limiter having a finite regulation time, the output overshoots. This overshoot can be used actively in driving the non-linear current sourcing of the PIN diode making it switch faster. The trade-off is a higher steady state power consumption. Q13 will dissipate the majority of the power since this is what regulates the voltage resulting in a given current. Hence, depending on the increase in voltage supply, Q13 may need additional cooling and/or swapped for another transistor entirely.

Decreasing the reverse bias switching time, which is perhaps the most critical, might be achieved by using dedicated logic level transistors which are usually faster than the multi-purpose transistors used in this work. The main issue with logic level transistors is their lower power handling capabilities. Hence, even though the level shifters and FET drivers were updated with logic level transistors, it might not be possible to drive the rather high amount of current when having to switch high power MOSFETs away from deep saturation.

Another strategy for decreasing the reverse bias switching time is to use a lower

negative voltage supply for the negative level shifter, negative FET driver, and Q14. This also has the advantage of increasing the resistance of the PIN diode. Now, even though a higher negative voltage may help reduce the reverse bias switching time, it also depends on the slew rate of the driver itself seeing this is finite. Hence, depending on the PIN diodes non-linear current sinking, it could be advantageous to increase the negative supply voltage. However, it should be determined on a case by case basis. The GE scanner, for which this driver was primarily designed, uses a -5 V reverse bias and thus is what is used for this driver.

Now, increasing the positive and negative supply voltages might look straight forward. However, it is highly dependent on the maximal drain-source and base-emitter voltages of the transistors. If these maximum ratings are exceeded either other transistors must be utilized or a stacked transistor design is required. The stacked transistor design is not presented in this work since it is well described in [23].

Malfunction detection has not been implemented. By using a differential opamp configuration over the static resistor in the current limiter (R17) to detect the voltage, the current is easily calculated using Ohm's law. The problem with this approach occurs if Q14 or R20 breaks into a short. The current then flows through Q14 and/or R20 rather than into the PIN diode. The safest approach is to add a small series resistor in the output and thus detect the voltage across, again using a differential opamp configuration.

The standard components used to implement the driver are magnetic. This is of course not ideal. Usually, the culprit is the package of which the leads have a layer of nickel deposited. If it is possible to acquire the dies before packaging, custom packing/direct bonding to the printed circuit board (PCB) might solve the problem. However, it would be immensely expensive and the lead time would be very long. As such, we make sure that the driver is placed at least 0.5 m away from the region of interest in the MRI scanner. No shimming problems were observed.

Finally, the driver presented in this work is single ended. Brunner et al. [20] showed that if sub-*u*s switching of a high power T/R switch is needed, differential operation is required. By changing the buffer into an inverting Schmitt trigger and using the presented driver in conjunction, it is possible to operate differentially. It does, however, require twice the amount of components. Given that the drivers are placed outside the bore of the scanner this should not pose a problem. Additionally, since the driver is made using readily available components, the cost is in the range of 30-50 € per piece. Thus, the added cost of operating differentially is fairly low, even though the relative price doubles.

C.5 Conclusion

A PIN diode driver using readily available discrete components featuring forward and reverse bias switching times of 2 μs and 0.4 μs, respectively, has been presented. When the driver is in forward bias, a current limited voltage is supplied to either a T/R switch or Q-spoiling circuit. In reverse bias, -5 V is supplied to the PIN diodes. The driver was tested in both an MRI scanner (for controlling a Q-spoiling switch on a receive surface coil) and NMR spectrometer (to control a T/R switch). The driver presented in this work had similar performance to the commercial solutions. Hence, a complete PIN diode driver has thus been presented which, to the best knowledge of the authors, have thus far been omitted in the MR community. Further, this paper takes a step towards 'build your own scanner/spectrometer'. Finally, utilizing a self-built driver eases the design of custom T/R switches and Q-spoiling circuits since the built-in driver of the NMR spectrometer or MRI scanner is no longer a limiting factor.

References

[1] J. D. Sanchez-heredia, E. Søvsø, S. Hansen, C. Laustsen, V. Zhurbenko, and J. H. Ardenkjær-larsen, "Low-Noise Active Decoupling Circuit and its Application to 13C Cryogenic RF Coils at 3 T," *Tomography*, vol. 3, no. 1, pp. 60–66, 2017.

[2] R. H. Caverly, "PIN diode-based transmit-receive switch for 7 T MRI," in *IEEE Topical Conference on Biomedical Wireless Technologies, Networks, and Sensing Systems (BioWireleSS)*, Jan 2016, pp. 100–102.

[3] R. H. Caverly and S. Benbrook, "Control Device Thermal Modeling in MRI Receive Coil Q-Spoiling Circuits," *IEEE Journal of Electromagnetics, RF and Microwaves in Medicine and Biology*, vol. 1, no. 2, pp. 52–58, Dec 2017.

[4] ——, "Thermal modeling of Q-spoil switching elements for MRI coils," in *IEEE MTT-S International Microwave Bio Conference (IMBIOC)*, May 2017, pp. 1–3.

[5] A. Maunder, M. Rao, F. Robb, and J. M. Wild, "Comparison of MEMS switches and PIN diodes for switched dual tuned RF coils," *Magnetic Resonance in Medicine*, vol. 80, no. 4, pp. 1746–1753, 2018.

[6] M. Twieg, M. A. de Rooij, and M. A. Griswold, "Active Detuning of MRI Receive Coils with GaN FETs," *IEEE Trans. on Microw. Theory and Techn.*, vol. 63, no. 12, pp. 4169–4177, Dec 2015.

[7] B. Thapa, J. Kaggie, N. Sapkota, D. Frank, and E.-K. Jeong, "Design and Development of a General-Purpose Transmit/Receive (T/R) Switch for 3T MRI," *Concepts in Magnetic Resonance Part B: Magnetic Resonance Engineering*, vol. 46B, no. 2, pp. 56–65, 2016.

[8] R. H. Caverly and X. Ma, "Nonlinear stored charge vs d.c. bias-current relationship under high-level injection in pin diodes," *Solid State Electron.*, vol. 32, no. 4, pp. 329–332, 1989.

[9] *MA4P MELF & HIPAX Series*, MACOM Technology Solutions Inc., Rev. 16.

[10] Skyworks, "Driver Circuit for High-Power PIN Diode Switches," Skyworks Solutions, Inc., Tech. Rep., 2016.
[11] National Semiconductor, "P-I-N diode drivers," Electronic Engineering, Tech. Rep., 1972.
[12] ——, "PIN Diode Drivers," Application Note 49, Tech. Rep., 1986.
[13] J. Ardizzoni, "Driving PIN Diodes: The Op-Amp Alternative," *Analog Dialogue*, vol. 44, no. 1, pp. 11–15, May 2010.
[14] G. Forlani and F. Fresia, "Driving PIN Diodes: The Op-Amp Alternative," *CSELT Rapporti tecnici*, vol. 10, no. 5, pp. 317–320, Oct 1982.
[15] B. Harvey, "A high-voltage ATE pin driver," in *Proc. of the Bipolar/BiCMOS Circuits and Tech. Meeting*, Oct 1992, pp. 234–237.
[16] C. van Niekerk and P. W. van der Walt, "High speed high voltage PIN diode driver," in *IEEE Intern. Symp. on Industrial Electronics*, vol. 1, July 1998, pp. 167–170.
[17] T. P. Ryan and W. Miller, "Design and performance of a high speed driver circuit for PIN diode switches used in microwave hyperthermia," *J. Biomed. Eng.*, vol. 11, no. 2, pp. 130–132, 1989.
[18] Y. Xiao, Z. Zhao, Z. Qian, and H. Zhou, "A High Isolation Switching Unit for MRI System," in *Procedia Eng.*, vol. 7. Elsevier Inc., 2010, pp. 265–269.
[19] C. Brorsson, "Pin diode drive circuits optimized for fast switching," Master's thesis, Chalmers, 2011.
[20] D. O. Brunner, L. Furrer, M. Weiger, W. Baumberger, T. Schmid, J. Reber, B. E. Dietrich, B. J. Wilm, R. Froidevaux, and K. P. Pruessmann, "Symmetrically biased T/R switches for NMR and MRI with microsecond dead time," *J. Magn. Reson.*, vol. 263, pp. 147–155, 2016.
[21] D. H. Johansen, J. D. Sanchez-Heredia, J. R. Petersen, T. K. Johansen, V. Zhurbenko, and J. H. Ardenkjær-Larsen, "Cryogenic Preamplifiers for Magnetic Resonance Imaging," *IEEE Trans. on Biomedical Circ. and Syst.*, vol. 12, no. 1, pp. 202–210, Feb 2018.
[22] W. McMurray, "Selection of Snubbers and Clamps to Optimize the Design of Transistor Switching Converters," *IEEE Trans. on Industry Applications*, vol. 16, no. 4, pp. 513–523, July 1980.
[23] R. J. Baker and B. P. Johnson, "Stacking power MOSFETs for use in high speed instrumentation," *Review of Scientific Instruments*, vol. 63, no. 12, pp. 5799–5801, 1992.

Paper D

Towards New Vistas in Preamplifier Design for MRI

D. H. Johansen, J. D. Sanches-Heredia, V. Zhurbenko, and J.H. Ardenkjær-Larsen

The European Microwave Conference (EuMC), pp. 1159-1162, 2017
The European Microwave Integrated Circuits Conference (EuMIC), pp. 419-422 2017

The layout has been revised.

Abstract

High signal to noise ratio (SNR) in magnetic resonance imaging is vital for ensuring accurate diagnosis and treatment. Arrays of surface coils for receive only purposes is a well established way to increase SNR. However, due to crosstalk between the array elements, the SNR can be severely degraded. For that reason, arrays often do not exploit their full potential. By using a series decoupling network with non-conventional matching and preamplifier impedances the decoupling between elements can be increased significantly. In the presented design example, almost 6 dB additional decoupling can be achieved with no impairment of preamplifier noise figure. The decoupling changes as a function of both coil and preamplifier performance. Thus, the fundamental trade-off between noise and decoupling is discussed. This work embarks on the path towards new vistas in design of preamplifiers for surface coil arrays for magnetic resonance imaging.

D.1 Introduction

Magnetic Resonance Imaging (MRI) is a non-invasive, non-ionizing method that produces high resolution images of anatomy and physiology, while also being able to investigate metabolism by use of spectroscopy. This makes it a powerful tool for diagnostic of diseases like cancer and injuries such as broken limbs. Evaluating images is inherently a subjective task where the signal to noise ratio (SNR) is one of the prevalent measures of quality [1]. The SNR of the nuclear magnetic resonance experiment is limited. A low SNR impairs both imaging and acquisition speed, in turn increasing cost [1]. This work investigates the fundamental trade-off between noise and decoupling when an array of surface coils is utilized.

In its most basic form MRI polarizes nuclear spins (typically protons, ^{1}H) within the patient in a strong static magnetic field called the main field. Now, the proton spins are tilted by applying an RF pulse orthogonally to the main field, at the Larmor frequency (precession frequency). When the RF pulse is switched off the proton spins return to equilibrium (relaxation). The precession and relaxation is recorded typically by Faraday induction. [2]

Several approaches can be used to increase SNR, including increasing the main field strength, longer scanning time by averaging and/or increasing the Q-factor of the receiving coil [3]. This work is focused on an approach using arrays of surface coils.

The key challenge in arrays is the parasitic coupling between elements. The coupling

between elements cause a two fold impairment. 1) Degradation of the Q-factor of the individual coils [4]. Unless meticulously designed, more noise arises from the coupling between elements in an array than the loading of a volume coil by a patient. Hence, using surface coil arrays becomes void. 2) In the realm of parallel imaging coupling causes information correlation and thus limits the usefulness of parallel imaging [5]. Information correlation is meant in the sense that if two coils were perfectly coupled they would show the exact same image at all times.

This work focuses on preamplifier decoupling by extending the seminal work by Roemer et al. [4]. Specifically, how to choose the matching impedance in order to maintain proper noise matching of the preamplifier while maximizing the decoupling. Roemer et al. describes the series decoupling network where matching and minimizing the current in the coil is achieved simultaneously. Roemer et al., however, only demonstrated the decoupling in the 50 Ω case. In this work, the fundamental trade-off between noise and decoupling is described when preamplifier decoupling is utilized. Further, it is shown that transforming the coil impedance to a complex impedance, rather than 50 Ω, leads to an increased decoupling while conserving the noise figure of the preamplifier.

The article is structured as follows. The first section reviews methods for coil decoupling. The second section derives the formulas describing the decoupling circuit. The third section describes the results and some practicalities in building and tuning the decoupling circuit. Lastly, conclusions are drawn.

D.2 Coupled Surface Coils

Fig. D.1 shows a system of two coils each attached with a matching circuit and preamplifier. The impedance of the coil is described by Z_{C}. The impedance seen by the coil is Z_{L}, the matching impedance seen by the preamplifier is Z_{M} and the preamplifier impedance is Z_{P}. The coupling between the two coils is described by $j\omega M$ where M is the mutual inductance and ω is the angular frequency. The current in the first coil i_1 when $i_0 \neq 0$ is

$$i_1 = \frac{j\omega M}{Z_{\mathrm{C}} + Z_{\mathrm{L}}} i_0 = \frac{j\omega k\sqrt{L_0 L_1}}{Z_{\mathrm{C}} + Z_{\mathrm{L}}} i_0, \tag{D.1}$$

where $0 \leq k \leq 1$ is the coupling factor and L is the inductance of the coils. Decoupling is, in most cases, achieved by using one or a combination of the following techniques.

1. **Critical overlapping:** When two surface coils are separated by a given dis-

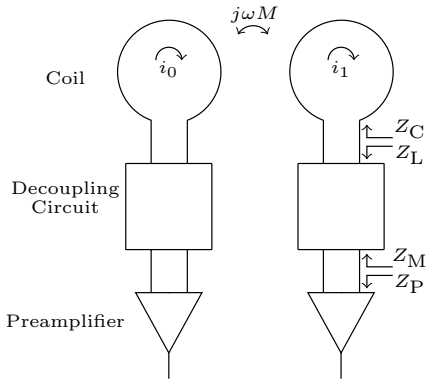

Figure D.1: System of two coupled surface coils.

tance a complete decoupling occurs [4]. This corresponds to $k = 0$. This is the most used method for nearest neighbour decoupling. However, it does not work for next nearest neighbours. Another aspect of critical overlapping is that in parallel imaging the overlap causes two coils to be correlated. This impairs the reconstruction in parallel imaging [5].

2. **Y-method:** Choosing Z_L such that the mutual inductance is cancelled out, full decoupling is achieved. Most often a capacitor is simply added between elements but more complicated methods can be employed [6–8]. The problem with this method is that the complexity, for a larger number of elements, grows quickly, and thus has not been used for much more than research purposes in MRI.

3. **Preamplifier decoupling:** By increasing Z_L the current i_1 is lowered, and hence decoupling is again accomplished. This is very simple, can be easily tuned in and works for all elements in an array.

The most used methods are critical overlapping and preamplifier decoupling [4, 9].

D.3 Decoupling Circuit

The general solution for the series decoupling circuit in Fig. D.2 is presented when the matching and preamplifier impedances are both complex. Also, the matching impedance is discussed in terms of the noise parameters of the preamplifier.

D.3.1 Series Decoupling Network

The series decoupling network described by Roemer et al. is seen in Fig. D.2. Roemer et al. derives the impedance for a real matching and preamplifier impedance leading to a simpler interpretation of the network than is merited for complex impedances. The series connection of the coil and C_1 is

$$Z_1 = R_1 + j\left(X_{L_1} - X_{C_1}\right). \tag{D.2}$$

The admittance Y_2 is

$$Y_2 = G_2 + jB_2 = \frac{1}{Z_2} = \frac{1}{Z_1} + jB_{C_2}, \tag{D.3}$$

where G_2 and B_2 is the conductance and susceptance of Y_2 respectively and B_{C_2} is the susceptance of $X_{C_2} = \frac{1}{B_{C_2}}$. Separating in real and imaginary components yield,

$$G_2 = \frac{R_1}{R_1^2 + \left(X_{L_1} - X_{C_1}\right)^2}, \tag{D.4}$$

$$B_2 = \frac{X_{L_1} - X_{C_1}}{R_1^2 + \left(X_{L_1} - X_{C_1}\right)^2} + B_{C_2}. \tag{D.5}$$

The matching impedance is determined by

$$Z_{\mathrm{M}} = R_{\mathrm{M}} + jX_{\mathrm{M}} = Z_2 + jX_{L_2}. \tag{D.6}$$

Separating into real and imaginary components yield

$$R_{\mathrm{M}} = \frac{G_2}{G_2^2 + jB_2^2}, \tag{D.7}$$

$$X_{\mathrm{M}} = X_{L_2} - \frac{B_2}{G_2^2 + jB_2^2}. \tag{D.8}$$

By ensuring resonance of C_2 and L_2, ideally $Z_{\mathrm{L}} = \infty$. The required condition is

$$X_{L_2} + X_{\mathrm{P}} = X_{C_2}. \tag{D.9}$$

Thus Eqs. D.7, D.8 and D.9 form a system of three equations with three unknowns and is solved by combining Eqs. D.5, D.4, D.7, D.8 and D.9. The solution is

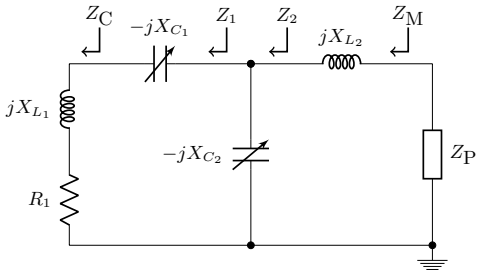

Figure D.2: Circuit diagram of the series decoupling network as proposed by Roemer et al [4].

$$A = \frac{\sqrt{R_1 R_M \left(R_M^2 + X_M^2 + 2X_M X_P + X_P^2\right)}}{R_M} \tag{D.10}$$

$$X_{C_1} = \frac{R_1 \left(X_M + X_P\right)}{R_M} + X_{L_1} \mp A \tag{D.11}$$

$$X_{L_2} = -X_P \pm A, \tag{D.12}$$

Positive results imply that C_1, C_2 are capacitors and L_2 is an inductor. If negative, the capacitors become inductors and vice versa. Interpreting the solution in the Smith Chart Fig. D.3 clarifies. Given an inductance with some resistance the first point is (a). Adding a large series capacitor C_1 the reactance is moved only slightly to (b). By a parallel capacitor C_2 the impedance is transformed in a constant conductance circle into (c). From here, C_2 is resonated with L_2 transforming into 50 Ω at (d). Another solution is to have a small C_1 transforming the impedance into the capacitive area of the Smith Chart, point (e). From here a parallel inductor is needed to transform to point (f). Finally, a series capacitor resonates the inductor and transforms to (d). Hence two solutions are indeed possible.

Table D.1: Preamplifier properties.

$F_{\min}$	1.076
R_n	11.60 Ω
Y_n	0.00583-j 0.00988 Ω
Z_P	5.42-j 57.11 Ω

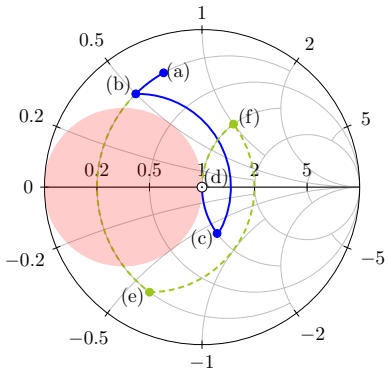

Figure D.3: Smith Chart illustrating the two solutions of the series decoupling network.

D.3.2 Matching and Preamplifier Impedances

In Table D.1 the properties of a 300 MHz preamplifier are listed. The preamplifier is based on [10] but matched for 300 MHz instead of 32 MHz. This operating frequency corresponds to a main field strength of 7 T. The noise figure as a function of the matching admittance is

$$F = F_{\min} + \frac{R_{\mathrm{n}}}{G_{\mathrm{M}}}|Y_{\mathrm{M}} - Y_{\mathrm{n}}|^2 \tag{D.13}$$

where F is the noise figure at the given matching admittance $Y_{\mathrm{M}} = G_{\mathrm{M}} + jB_{\mathrm{M}} = \frac{1}{Z_{\mathrm{M}}}$, $F_{\min}$ is the minimal noise figure at the optimal noise admittance Y_{n}, and R_{n} is the noise resistance. Choosing $Y_{\mathrm{M}} \neq Y_{\mathrm{n}}$ yields a system of noise figure circles which can be visualized using a Smith Chart. Fig. D.4 shows a circle in which the 50 Ω impedance is located (on this circle all impedances yield the same noise figure, however, they do not yield the same decoupling). The optimal noise match is shown as a cross. The current i_1 is plotted relative to i_1 at 50 Ω in Fig. D.5 as a function of the angle of the noise figure circle. Each angle corresponds to a complex impedance. At 50 Ω matching impedance the current is normalized to 0 dB. The minimum current occurs at a matching impedance of $55 + j153$ Ω. Here a 5.6 dB additional decoupling is achievable.

The gain of the preamplifier has not been discussed in much detail. The required gain for a preamplifier is defined by a particular MRI system configuration and corresponding noise budget. Whatever the gain requirement is, the gain circles can be plotted in the same Smith Chart as the decoupling and noise figure circles. Their unity then defines the trade-off that can be made within the wanted requirements.

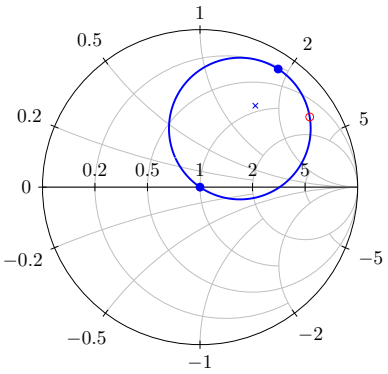

Figure D.4: Noise figure circle passing through 50 Ω. Cross indicates optimal noise match, red open circle is the optimal decoupling. Anything between the closed circles on the optimal decoupling side indicate an increased decoupling.

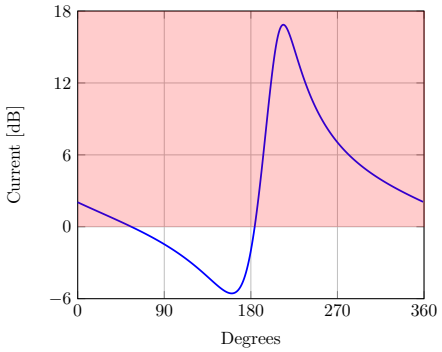

Figure D.5: Current i_1 is relative to i_1 at 50 Ω as a function of the angle of the noise figure circles corresponding to a unique impedance for each angle.

Further work could look into integrating a measure of SNR as a function of gain, noise figure and decoupling into the Smith Chart.

D.4 Results

The implemented decoupling circuit is found in Fig. D.6 which is designed for 300 MHz. The coil is 5 cm in diameter using copper wire with a 3.2 mm thickness, mounted on plexiglass as seen in Fig. D.7.

A number of practical aspects complicate the implementation of the matching circuit. Active decoupling (protection) is required to not impair the homogeneity of the

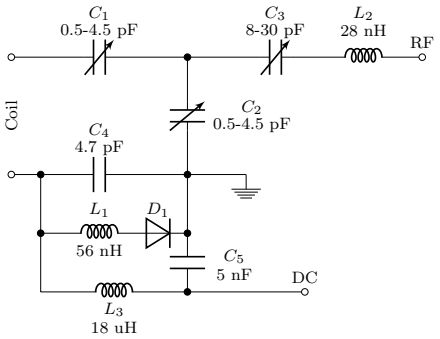

Figure D.6: Final decoupling circuit including tunable components and active decoupling.

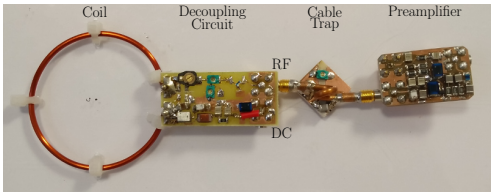

Figure D.7: Setup with the coil, decoupling circuit, cable trap and preamplifier.

transmitting coil and to prevent damaging the preamplifier. It works, in this case, by adding a parallel resonant circuit consisting of C_4 and L_1 in series with the coil to block the current at the frequency of interest. The inductor is switched on by the PIN diode D_1 which is activated by a DC signal fed through L_3. C_5 filters the DC path to avoid noise injection.

Capacitors C_1, C_2 and C_3 enable fine tuning of both the match and the decoupling. An issue with the series decoupling network is that matching and decoupling are correlated. This causes the procedure for tuning of the circuit to become tedious. First, the impedance is tuned using a network analyzer connected at the cable trap, see Fig. D.7. Then, the decoupling is measured using the principle of reciprocity detailed in [11–13] with the preamplifier connected. This procedure is repeated until both matching and decoupling has been achieved. Further, a cable trap has been devised in order to block common mode current from flowing on the shield of the coaxial wire. The cable trap adds an inductance of approximately 10 nH between the decoupling circuit and the preamplifier.

The matching impedance was chosen at 50 Ω and the decoupling compared relative to this. The matching impedance for the comparison is $60.5 + j139$ Ω showing a relative increase in decoupling by 2.3 dB. Theoretically the decoupling should be 3.3 dB.

The theoretical decoupling is not observed because of two aspects, 1) measurement uncertainty because the measurement is at the edge of the equipments range, 2) losses and tolerances of the components are not taken into account in the model. The optimal impedance for decoupling is not reached because the matching and decoupling is tuned using the same components. Hence, when the decoupling is optimal, the matching is skewed and vice-versa. This highlights the practical difficulty in tuning the series decoupling network to the optimum state.

D.5 Conclusions

Formulas for the series decoupling network for arbitrary matching and preamplifier impedances have been derived. This is used to show that matching to a different impedance than 50 Ω achieves additional decoupling of surface coil elements while preserving the noise figure of the preamplifier. The work shows that for a given preamplifier, which was not designed for the purpose of decoupling, the optimal matching in terms of decoupling is indeed different from 50 Ω. Simulations show a potential of 5.6 dB additional decoupling for the described setup. Measurements confirm the simulations by showing a 2.3 dB increase in decoupling. However, this was not at the optimal matching impedance. The optimal matching impedance was not achieved due to the practical difficulties in tuning the series decoupling circuit.

Having showed a proof-of-concept, the fundamental trade-off between noise, decoupling and gain of preamplifiers for MRI can now be examined in detail analytically. We are now looking towards better integration and co-design of preamplifiers and decoupling circuits.

References

[1] D. Erdogmus, E. G. Larsson, R. Yan, J. C. Principe, and R. Fitzsimmons, “Measuring the signal-to-noise ratio in magnetic resonance imaging: a caveat,” *Signal Processing*, vol. 84, pp. 1035–1040, 2004.

[2] C.-N. Chen and D. I. Hoult, *Biomedical Magnetic Resonance Technology*, 1st ed. Institute of Physics Publishing, 1989.

[3] D. G. Nishimura, *Principles of Magnetic Resonance Imaging*, 1st ed. lulu.com, 2010.

[4] P. B. Roemer, W. A. Edelstein, and C. E. Hayes, “The NMR Phased Array,” *Soc. Magn. Reson. Med.*, vol. 225, pp. 192–225, 1990.

[5] K. P. Pruessmann, M. Weiger, M. B. Scheidegger, and P. Boesiger, “SENSE sensitivity encoding for fast MRI.pdf,” *Soc. Magn. Reson. Med.*, vol. 42, no. 5, pp. 952–962, 1999.

[6] J. B. Andersen and H. H. Rasmussen, “Decoupling and Descattering Networks for Antennas,” *IEEE Trans. Antennas Propag.*, vol. 24, no. 6, pp. 841–846, 1976.

[7] J. Weber, C. Volmer, K. Blau, R. Stephan, and M. A. Hein, “Miniaturized antenna

arrays using decoupling networks with realistic elements," *IEEE Trans. Microw. Theory Tech.*, vol. 54, no. 6, pp. 2733–2740, 2006.

[8] J. C. Coetzee and Y. Yu, "Design of decoupling networks for circulant symmetric antenna arrays," *IEEE Antennas Wirel. Propag. Lett.*, vol. 8, no. 2, pp. 291–294, 2009.

[9] A. Reykowski, S. M. Wright, and J. R. Porter, "Design of Matching Networks for Low Noise Preamplifiers," *Magn. Reson. Med.*, vol. 33, no. 6, pp. 848–852, 1995.

[10] D. Johansen, J. Sánchez-Heredia, V. Zhurbenko, and J. Ardenkjær-Larsen, "Practical Aspects of Preamplifier Designs for 13C Imaging," in *ISMRM 25th*, 2017.

[11] D. Hoult and R. Richards, "The signal-to-noise ratio of the nuclear magnetic resonance experiment," *J. Magn. Reson.*, vol. 24, no. 1, pp. 71–85, 1976.

[12] D. I. Hoult and P. C. Lauterbur, "The sensitivity of the zeugmatographic experiment involving human samples," *J. Magn. Reson.*, vol. 34, no. 2, pp. 425–433, 1979.

[13] D. I. Hoult, "The principle of reciprocity in signal strength calculations—A mathematical guide," *Concepts Magn. Reson.*, vol. 12, no. 4, pp. 173–187, 2000.

Paper E

Practical Aspects of Preamplifier Designs for ^{13}C Imaging

D. H. Johansen, J. D. Sanches-Heredia, V. Zhurbenko, and J.H. Ardenkjær-Larsen

Proceedings of the International Society of Magnetic Resonance in Medicine (ISMRM), no. 4299, 2017

The layout has been revised.

Abstract

This abstract presents two preamplifier designs for ^{13}C imaging optimized either for single or array coil usage. For single coil usage the preamplifier is designed to minimize noise yielding a noise figure of 0.25 dB. For array coils coupling between elements is a problem when the input impedance of the preamplifier is high. Hence the main contribution of this work is a low resistance, inductive input impedance preamplifier yielding better decoupling for array coils, while maintaining acceptable gain (20 dB) and noise figure (0.75 dB).

E.1 Purpose

Non-magnetic preamplifiers for 3T ^{13}C MRI is a sparse commodity that is, to the authors knowledge, only available from one vendor, WanTcom [1]. This abstract presents two 3T ^{13}C MRI preamplifier designs operating at 32.1 MHz. Design 1 is optimized for the noise figure (NF) and intended for single coil usage. Design 2 optimizes input impedance for array coils using preamplifier decoupling [2] which is especially useful when utilizing hyperpolarization [3]. Further, this work elaborates on the practical aspects of preamplifier design describing the vital aspects for matching, stability, NF and gain.

E.2 Methods

The important aspect in designing a preamplifier is choosing a proper device for amplifier realization. For practical considerations, in order to simplify the voltage supply, a positive controlled bias transistor is preferable. This leaves two options: either a bipolar or enhancement mode field effect transistor (FET). Bipolar transistors suffer from an inherently higher 1/f-noise which impairs the achievable noise for a ^{13}C preamplifier. Among FETs an enhancement mode pseudomorphic high electron mobility transistor (pHEMT) from Avago (ATF54143 [4]) has low NF and is chosen in this work.

Another important aspect is to determine an unconditionally stable topology. These considerations have led to the common-source topology shown in Fig. E.1. A common-gate topology was investigated as well, but was extremely difficult to stabilize. Source degeneration (adding an inductor between source and ground of the transistor) was attempted but showed instability and was discarded.

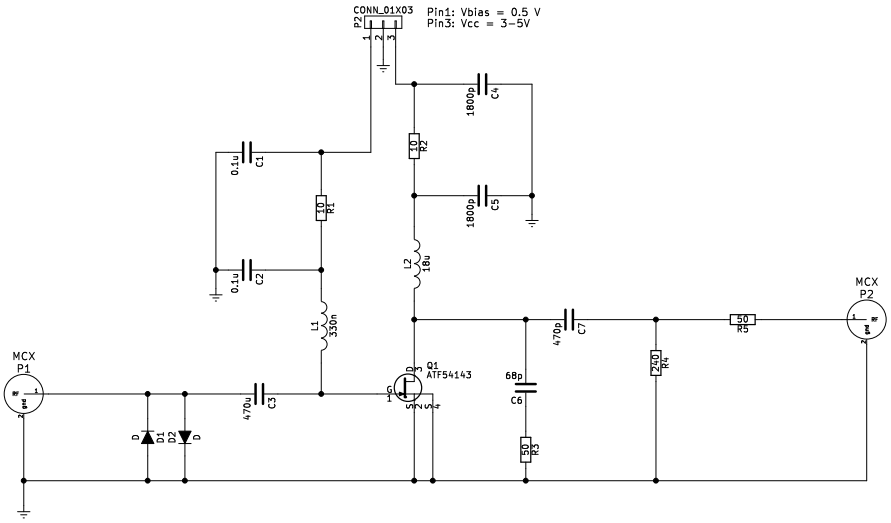

Figure E.1: Schematic of the preamplifier. To ensure stability the biasing network consisting of L1, C2, R1 and C1 is paramount. L1 and C2 forms a low frequency short circuit to ground on the input. C1 and R1 forms a filter ensuring that no amplification path is present in the supply path. On the output R3 and C6 forms a low pass filter ensuring high frequency stability. The network formed by R4, R5 and the load (assumed 50 ohms) is a dampening circuit that decreases the gain to further ensure stability.

Preamplifier	Noise figure [dB]	Gain [dB]	Impedance [Ohm]	SNR
WMA32C	0.7	28	3	425
Optimal NF	0.25	23	1-j24	—
Optimal impedance	0.75	20	0.4+j67	424

Table E.1: Measured noise Figure, gain and input impedance of the two designs and the WMA32C.

In order to optimize the NF a variable series and shunt 1.5-40 pF capacitor was added externally and tuned for optimal noise performance. The optimal impedance preamplifier is designed for a low resistance and inductive input impedance. The schematic for the optimal impedance design is seen in Fig. E.1. C3 is a DC block ensuring that the high input impedance of the transistor is shunted by L1. Hence L1 transforms the high input impedance transistor into a low resistance, inductive preamplifier. The layout for the optimal impedance design is found in Fig. E.2.

The optimal impedance design and WanTcom WMA32C have been equipped with identical loop coils and measured in a GE Signa HDx 3T clinical scanner [5]. Fig. E.3 shows the single coil setup with decoupling network and the optimal impedance preamplifier. The imaging sequence was a CSI with an FOV of 120x120x50 mm^3,

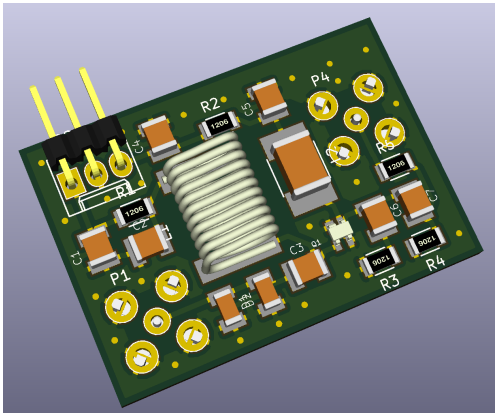

Figure E.2: Layout. It is very important during layout to minimize the inductance from source to ground or the preamplifier will become unstable.

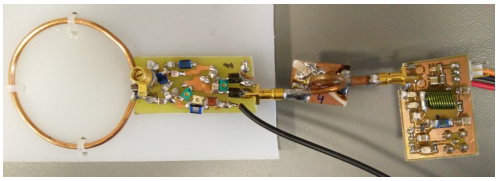

Figure E.3: From the left is seen the coil, with a diameter of 5 cm. Next is the decoupling network and finally the optimal impedance preamplifier without copper shield.

duration of 19 s and 16x16 points, and the phantom was a 1 M ^{13}C-bicarbonate phantom.

E.3 Results

The measured NF, gain and input impedance is found in Table E.1 for both designs and the WMA32C. Measured SNR is seen in Fig. E.4. Notice that in design 2 the gain drops by 8 dB and NF rises 0.05 dB compared to the WMA32C. However, measured SNR remains unimpaired. In terms of performance of the optimized impedance design in an array please refer to another ISMRM abstract by J. D. Sanchez-Heredia et al.

E.4 Discussion

The results indicate that preamplifier noise is not the dominant noise contribution for a loop coil of 5 cm diameter. This makes it possible to optimize the preamplifiers

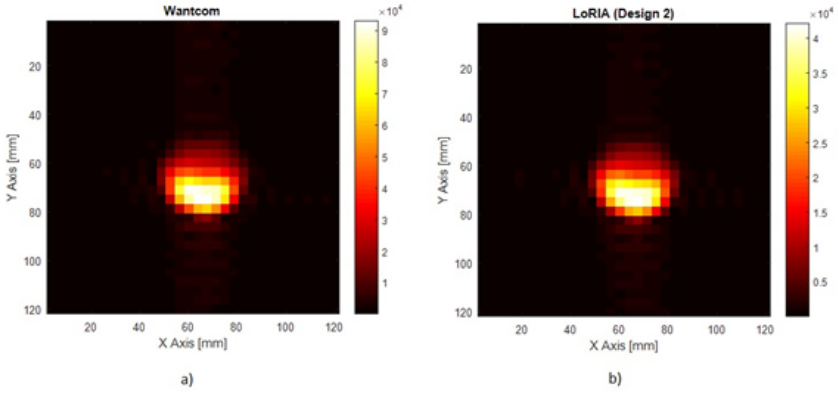

Figure E.4: Measured image of a) the WanTcom (SNR=425) and b) the optimized impedance design (SNR=424).

impedance yielding better array decoupling while not impairing the single coil's SNR by trading-off gain and NF. Indeed the exact trade-off between NF, gain, impedance and SNR is unclear but this abstract indicates that the trade-off made here is acceptable.

In terms of the preamplifier designs it may be possible to select another transistor having better low frequency stability. Due to the transistor gain increasing significantly at lower frequencies extra dampening of gain is required. Perhaps another transistor with a worse NF rating may be better at 32 MHz if the extra stability measures were not needed. Also, the output is not matched to 50 ohms though the dampening circuit formed by R4, R5 and the load does yield a match of 2.2:1 VSWR. Hence better performance can be achieved.

Finally, the size of L1 can cause unwanted coupling between the preamplifiers in an array. Hence shielding of the preamplifier is needed.

E.5 Conclusion

Two preamplifier designs have been proposed for 3T ^{13}C imaging optimizing either noise figure or the input impedance. The first design showed a noise figure of 0.25 dB making it, the the knowledge of the authors, best in class. However, when considering hyperpolarized ^{13}C imaging an array is usually preferred. Thus the second design optimized the input impedance to 0.4+j67 Ω with a NF of 0.75 dB and gain of 20 dB. In another abstract, this has proven to yield a significantly better decoupling and thus higher SNR of an array when compared with the WMA32C preamplifier

References

[1] *WMA32C: 32.19 MHz Low Noise Low Impedance Preamplifier*, WanTcom Inc., 2013, rev. B.

[2] P. B. Roemer, W. A. Edelstein, and C. E. Hayes, "The NMR Phased Array," *Soc. Magn. Reson. Med.*, vol. 225, pp. 192–225, 1990.

[3] R. F. Lee, G. Johnson, R. I. Grossman, B. Stoeckel, R. Trampel, and G. McGuinness, "Advantages of parallel imaging in conjunction with hyperpolarized helium - a new approach to mri of the lung," *Magnetic Resonance in Medicine*, vol. 55, no. 5, pp. 1132–1141, 2006.

[4] *ATF-581Ł3: Low Noise Enhancement Mode Pseudomorphic HEMT in a Surface Mount Plastic Package (Data Sheet)*, Avago Technologies, 2012.

[5] J. D. Sanchez-heredia, E. Søvsø, S. Hansen, C. Laustsen, V. Zhurbenko, and J. H. Ardenkjær-larsen, "Low-Noise Active Decoupling Circuit and its Application to 13C Cryogenic RF Coils at 3 T," *Tomography*, vol. 3, no. 1, pp. 60–66, 2017.

Paper F

Ideal Coil Decoupling in Receive Arrays using Negative Resistance Preamplifiers

D. H. Johansen, J. D. Sanches-Heredia, V. Zhurbenko, and J.H. Ardenkjær-Larsen

Proceedings of the International Society of Magnetic Resonance in Medicine (ISMRM), no. 1711, 2018

The layout has been revised.

Abstract

This work presents the method of achieving ideal decoupling between elements in a receive coil array. Generally, preamplifier decoupling is limited by nonidealities of the implemented components. It is shown analytically and numerically, that for the ideal (lossless) matching circuits the input resistance of the preamplifier should be zero, while for the realistic lossy case a small negative resistance can be used to achieve ideal decoupling. Here we use a negative input resistance preamplifier (NIRP) to compensate for the loss of the circuit. The analysis is verified experimentally showing a decoupling of -62 dB when a NIRP with an input resistance of -0.023 Ω is used.

F.1 Introduction

Decoupling between individual coils in an MRI receive coil array is vital for two reasons; 1) SNR degradation from noise coupling (in the diagonal elements of the noise correlation matrix) and 2) frequency detuning of array elements. Roemer et al. showed that ideal preamplifier decoupling is achieved when the input resistance of the preamplifier is zero, given a lossless matching circuit [1]. However, matching circuits are lossy, especially when active transmit detuning is integrated. In this work, we show that when the matching circuit is lossy, for optimal preamplifier decoupling, a negative input resistance preamplifier (NIRP) is required. To confirm the method, we present decoupling measurements using an NIRP.

F.2 Methods

The coupling between elements in a receive coil array is primarily determined by the amount of current one coil can induce in another. Hence, increasing the impedance seen by the coils, while being noise matched to the preamplifier, ensures decoupling between elements.

The principle of decoupling achieved by the matching circuits, described by Roemer et al. [1] and Reykowski et al. [2], is that a parallel resonance is created with an inductor such that a high impedance is presented to the coil. Hence impeding the current on the coil. An example of the parallel matching circuit is shown in Figure F.1, where decoupling is achieved when C1 resonates with the equivalent impedance of C2, C3, Lp and Rp thus forming a parallel resonance. In the lossless case, this parallel resonance exhibits an infinite Q-factor when the preamplifier has a zero input

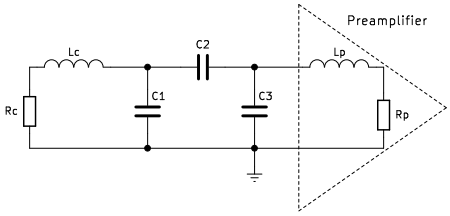

Figure F.1: Basic parallel matching circuit where Rc and Lc is the coil. The capacitors C1, C2 and C3 perform decoupling and matching. The preamplifier has an inductive (Lp) and resistive (Rp) input impedance.

resistance. Given that the resistance of the preamplifier is increased the Q-factor of the parallel resonance is lowered, the equivalent impedance is also lowered, more current is able to flow in the coil and thus a worse decoupling entails. In the case of a lossy matching circuit a zero resistance preamplifier does not yield an infinite Q-factor of the parallel resonance. To achieve the ideal decoupling the loss of the matching circuit can be compensated. The loss compensation is realized by an NIRP with a specific negative resistance such that the impedance seen by the coil is, theoretically, infinite.

The decoupling is measured using a system of two small loop coils of 1 cm diameter separated by a distance of 4 cm connected to a vector network analyzer as seen in Figure F.2. A parallel matching circuit, including active transmitter detuning, is used as presented by Sanchez-Heredia et al. [3]. The coil is an 8 cm loop coil with an unloaded Q-factor of approximately 350 at 32.13 MHz, corresponding to the

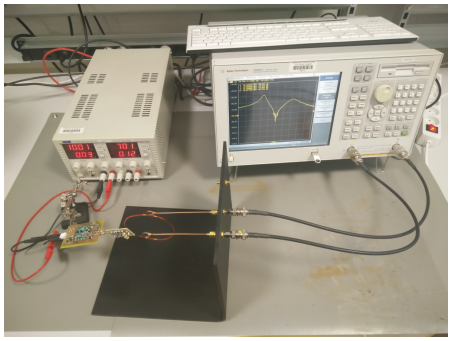

Figure F.2: Measurement setup. In the back to the right is the power supply for the preamplifier, in the back to the left is the network analyzer. In the front, from left to right, is the preamplifier which is connected to the matching circuit and coil. The coil is placed between the two loop probes which are connected to the two ports of the network analyzer.

frequency of 13C at 3T. The NIRP is a custom design (based on the design presented by Johansen et al. [4]) where the input impedance can be tuned while the noise figure remains constant at approximately 0.5 dB.

F.3 Results

Figure F.3 shows the simulated decoupling as a function of the input resistance of the preamplifier. It is seen that the optimal resistance is zero for the lossless case as expected. For the lossy case the optimal resistance is negative. For higher resistances the decoupling converges for the two cases. The measured decoupling as a function of frequency is plotted in Figure F.4 for four different resistances of the preamplifier. As expected, the optimal decoupling is found when a small negative input resistance (-0.023 Ω) of the preamplifier is used resulting in a decoupling of -62 dB at 32.13 MHz.

F.4 Discussion

The bandwidth of the decoupling is fairly narrow and the very high decoupling reported here is only at a single frequency. Since the bandwidth of the MRI experiment is in the range of 50-100 kHz this poses an issue. Theoretically it is possible to design a NIRP which exhibits an input impedance that yields a wider bandwidth. However, for this work, we have focussed on showing the principle of loss correction rather than increasing the bandwidth of the decoupling.

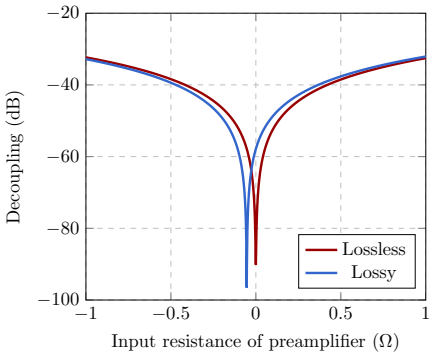

Figure F.3: Simulated decoupling as a function of the input resistance of the preamplifier. The reason for the apparent difference in decoupling between the lossless and lossy case is due to numerical accuracy.

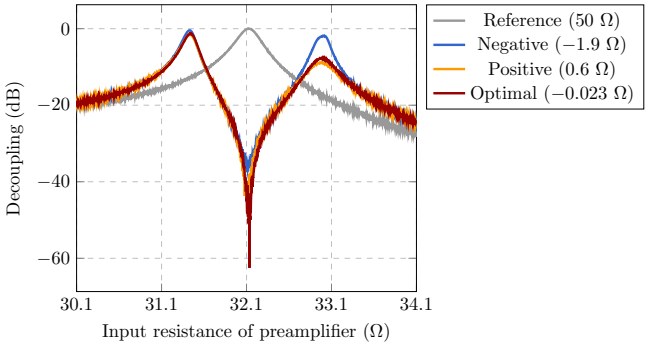

Figure F.4: Measured decoupling as a function of frequency. The decoupling at 32.13 MHz is -37 dB, -62 dB or -44 dB when a preamplifier input resistance of -1.9 Ω, -0.023 Ω or 0.6 Ω is used. The measurement is limited by the resolution of the network analyzer. As the reference is measured at -47 dB, the absolute measured decoupling in the optimal case is -109 dB. In order to increase the accuracy the power of the network analyzer can be increased, however this overdrives the preamplifier and yields incorrect results.

F.5 Conclusion

We have presented the concept of loss correction to achieve, in theory, a perfect element decoupling for receive coil arrays in MRI. The implication is that a negative input resistance preamplifier (NIRP) is required to reach the perfect decoupling. This is because the loss of the matching circuit must be compensated. Measurements confirm the hypothesis, showing an optimal decoupling of -62 dB with a preamplifier input resistance of -0.023 Ω. Further work involves demonstrating the decoupling during different load conditions.

References

[1] P. B. Roemer, W. A. Edelstein, and C. E. Hayes, "The NMR Phased Array," *Soc. Magn. Reson. Med.*, vol. 225, pp. 192–225, 1990.

[2] A. Reykowski, S. M. Wright, and J. R. Porter, "Design of Matching Networks for Low Noise Preamplifiers," *Magn. Reson. Med.*, vol. 33, no. 6, pp. 848–852, 1995.

[3] J. D. Sánchez-Heredia, E. Søvsø, S. Hansen, C. Laustsen, V. Zhurbenko, and J. H. Ardenkjær-Larsen, "Decoupling Scheme for a Cryogenic Rx-Only RF Coil for 13C Imaging at 3T," in *Proc. Intl. Soc. Mag. Reson. Med. 25*, 2017.

[4] D. H. Johansen, J. D. Sánchez-Heredia, V. Zhurbenko, and J. H. Ardenkjær-Larsen, "Practical Aspects of Preamplifier Designs for 13C Imaging," in *Proc. Intl. Soc. Mag. Reson. Med. 25*, 2017.

Paper G

Accurate Noise Figure Measurements for Highly Mismatched Preamplifiers

D. H. Johansen, J. D. Sanches-Heredia, V. Zhurbenko, and J.H. Ardenkjær-Larsen

Proceedings of the International Society of Magnetic Resonance in Medicine (ISMRM), no. 1692, 2018

The layout has been revised.

Abstract

A method reducing the uncertainty of noise figure measurements of highly mismatched preamplifiers is presented. In many cases when measuring the noise figure of preamplifiers for MRI receive arrays the uncertainty is approximately ±0.4 dB. Since the noise figure of the preamplifier is also in this range, a more accurate method is needed. Here we show an increase of 59 % in noise figure accuracy by adding an attenuator between the noise source and preamplifier.

G.1 Introduction

Characterizing the noise figure of highly mismatched preamplifiers for MRI receive arrays entails an inherent large estimated uncertainty of the experiment when using a standard 50 Ω measurement system [1]. Especially when the noise figure of the preamplifier is below 1 dB the measurement uncertainty becomes dominant [2–4]. This work presents a method for reducing the uncertainty of noise figure measurements when the preamplifier has an input reflection coefficient approaching unity with a noise figure below 1 dB. Further, the measurement errors from correctable error sources are measured to compare their practical significance in measuring noise figure.

G.2 Methods

Correctable bias when measuring noise figure includes e.g. temperature drift of the noise source, shielding of the preamplifier to prevent pickup of spurious signals and choosing a proper measurement bandwidth. The uncertainty when measuring noise figure is caused by the non-correctable thermal noise of components in the chain of the measurement device and general calibration errors of the noise meter [1].

A measurement uncertainty is normally given by the manufacturer of the noise meter [5]. The primary sources of uncertainty is the gain of the preamplifier, the preamplifier's inherent noise figure and the standing wave ratio at the input of the preamplifier. The measured noise figure is Gaussian distributed in the decibel scale, hence $F_{\text{meas}} \sim \mathcal{N}\left(\mu_{\text{meas}}, \sigma^2_{\text{meas}}\right)$. If an attenuator is added between the noise source and the preamplifier the standing wave ratio seen by the noise source is decreased. The calculated noise figure of the preamplifier in the cascaded setup is described in the

decibel scale by

$$F_{\mathrm{P}} = G_{\mathrm{A}} + F_{\mathrm{meas}}, \tag{G.1}$$

where $G_{\mathrm{A}} \sim \mathcal{N}\left(\mu_{\mathrm{A}}, \sigma_{\mathrm{A}}^2\right)$ is the available gain of the attenuator in dB which is Gaussian distributed. Hence the preamplifier's noise figure in the cascaded system is also described by a Gaussian distribution with mean, $\mu_{\mathrm{P}} = \mu_{\mathrm{meas}} + \mu_{\mathrm{A}}$, and variance $\sigma_{\mathrm{P}}^2 = \sigma_{\mathrm{meas}}^2 + \sigma_{\mathrm{A}}^2$. The uncertainty is usually described by the 95 % confidence interval given by $\sigma_{\mathrm{P}}^{95\%} = 2 \cdot \left(\sigma_{\mathrm{meas}}^2 + \sigma_{\mathrm{A}}^2\right)^{0.5}$ for the cascaded system.

The measurement setup is seen in Figure G.1. The noise figure measurements are performed on a Keysight PSA (E4440A) spectrum analyzer with noise figure extension and internal preamplifier using 256 averages. The noise source is a Keysight 346B. The S-parameters of the attenuator and preamplifier are measured using a Keysight ENA (E5062A) network analyzer calibrated using the Short-Open-Load-Through technique also using 256 averages. The external power supply is an Aim TTi EL302RT. The voltage regulator is based on an LM317 design [6]. A Rohde and Schwarz CMW-Z10 faraday cage is used to shield the preamplifier from spurious signals.

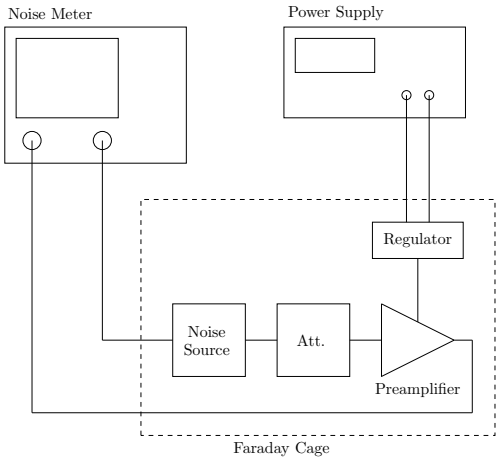

Figure G.1: Overview of the measurement setup. The noise meter (in this case a spectrum analyzer with noise figure extension) is connected to a noise source inside a faraday cage. The noise source is either connected to the attenuator as shown, or directly to the preamplifier. The power supply is either connected as shown to a voltage regulator inside the faraday cage, or directly to the preamplifier.

Scenarios				Measured F [dB]	Measured Gain [dB]	Calculated F [dB]	Calculated Gain [dB]	Uncertainty [dB]
BW	**Shield**	**Reg.**	**Att.**					
100 k	●	-	-	0.65	25.0	-	-	±0.385
100 k	●	●	-	0.55	25.0	-	-	±0.385
100 k	●	-	●	9.1	16.4	0.62	24.9	±0.157
100 k	●	●	●	9.0	16.4	0.52	24.9	±0.157
100 K	-	-	●	10.8	16.4	2.32	24.9	±0.157
100 K	-	-	-	2.0	25.0	-	-	±0.385
1 M	●	-	-	0.65	24.8	-	-	±0.385
1 M	●	●	-	0.45	24.8	-	-	±0.385
1 M	●	-	●	9.0	16.3	0.52	24.8	±0.157
1 M	●	●	●	9.0	16.3	0.52	24.8	±0.157
1 M	-	-	●	10.9	16.3	2.42	24.8	±0.157
1 M	-	-	-	2.0	24.9	-	-	±0.384

Table G.1: Measured noise figure and gain in different scenarios – bandwidth (BW), shielded box (Shield), regulated power supply (Reg.) and attenuator (Att.). The gain is measured to be between 24.8 and 25 dB depending on the measurement bandwidth. Using the voltage regulator lowers the noise figure by approximately 0.1 dB.

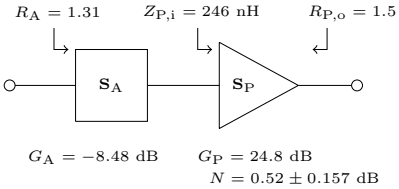

Figure G.2: Summarized measurement results. The standing wave ratio at the attenuator is 1.31 and the available gain is -8.48 dB. The input impedance of the preamplifier is measured at 246 nH. The output standing wave ratio of the preamplifier is 1.5. Finally the noise figure is measured at 0.52 ± 0.157 dB.

G.3 Results

Measurements and calculations are found in Table G.1 and Figure G.2. Measuring without the attenuator yields an uncertainty of ±0.385 [5], while the uncertainty of the uncorrected measurement with the attenuator is ±0.135. The available gain of the attenuator is measured at -8.483 ± 0.08 dB [7]. Thus yielding an uncertainty of ±0.157 when the attenuator is included.

G.4 Discussion

The gain of the preamplifier must be above approximately 10 dB in order to mitigate measurement uncertainty. It can be lower if an (additional) external preamplifier is used. Here, even though dropping the gain by 8.5 dB, the gain is still above the

critical point. This should be representative of most MRI preamplifiers.

Adding the attenuator decreases the mismatch between the preamplifier and noise source yielding a lower uncertainty. However, the uncertainty of the available gain of the attenuator is directly added to the estimated uncertainty. Hence, the applicability of this method is void if the decrease in estimated uncertainty from decreasing the mismatch is countered by the measurement uncertainty of the gain measurement of the attenuator. Generally, if we are concerned with highly mismatched preamplifiers the presented method is preferable.

An aspect concerning the method of noise figure acquisition, which is not covered in depth here, is the fact that the noise source switches between two known noise states to calculate the noise figure. These two noise states inherently change the impedance presented at the input of the preamplifier. The method presented here also mitigates this problem due to higher isolation

G.5 Conclusion

In this work we present a method for decreasing the uncertainty of noise figure measurements for highly mismatched preamplifiers. The described estimated uncertainty is achieved by adding a well-characterized attenuator between the preamplifier and the noise source. An example is shown, where the estimated uncertainty (95 % confidence interval) is lowered by 59 % (from ± 0.385 dB to ± 0.157 dB) for a 32 MHz preamplifier.

References

[1] Keysight, "Noise Figure Measurement Accuracy: The Y-Factor Method," Application Note, Tech. Rep., 2018.

[2] D. H. Johansen, J. D. Sánchez-Heredia, V. Zhurbenko, and J. H. Ardenkjær-Larsen, "Practical Aspects of Preamplifier Designs for 13C Imaging," in *Proc. Intl. Soc. Mag. Reson. Med. 25*, 2017.

[3] X. Cao, E. Fischer, J. G. Korvink, O. Gruschke, J. Hennig, and M. Zaitsev, "Design of a 3T preamplifier which is stability insensitive to coil loading," *J. Magn. Reson.*, vol. 265, pp. 215–223, 2016.

[4] J. Nordmeyer-Massner, N. D. Zanche, and K. Pruessmann, "Noise figure characterization of preamplifiers at NMR frequencies," *Journal of Magnetic Resonance*, vol. 210, no. 1, pp. 7–15, 2011.

[5] Noise Figure Uncertainty. [Online]. Available: http://rfmw.em.keysight.com/NFUcalc

[6] *LM317 3-Terminal Adjustable Regulator (SLVS044X)*, Texas Instruments, 2016.

[7] Vector Network Analyzer Uncertainty Calculator. [Online]. Available: www.keysight.com/find/na_calculator

Paper H

On the SNR of Cryogenic Receive Coils when using Room Temperature Preamplifiers

D. H. Johansen, J. D. Sanches-Heredia, V. Zhurbenko, and J.H. Ardenkjær-Larsen

Accepted for the *Proceedings of the International Society of Magnetic Resonance in Medicine (ISMRM), 2019*

Please note that while (H.5) is principally correct (if the noise figure is defined as an amplitude rather than power), Fig. H.2 and H.3 are incorrect, and are corrected in Chapter 3.

The layout has been revised.

Abstract

Significant increase of the signal-to-noise ratio (SNR) is possible by cooling receive coils to cryogenic temperatures, if they are not highly sample noise dominated. Conventionally, the noise of the preamplifier is excluded leading to an overestimation of the achievable SNR gain. In this work, we show that for the case of a small-animal birdcage coil for ^{13}C at 3 T cooled with liquid nitrogen to 77 K, the SNR is overestimated by approximately 40 % if the effect of the room temperature preamplifier is excluded. Hence, the preamplifier should either be included in the SNR gain estimation or cooled with the coil.

H.1 Introduction

In low-γ imaging, such as ^{13}C, ^{23}Na, and ^{14}N, the sample loading is lower compared to ^{1}H imaging. As a consequence, the electronic noise from coils and preamplifiers is dominating and has to be minimized to ensure efficient sample loading. Lowering electronic noise can be achieved by cooling copper coils with e.g. liquid nitrogen (LN) [1] or using high temperature superconductors (HTS) [2–4]. Many of the articles dealing with cryogenic coils assume that the preamplifier is the same for both the room temperature and cryogenic coil [5]. However, this may only be partially true because the noise figure of a preamplifier is defined in terms of the noise on the input, which depends on the temperature. Hence, even though the preamplifier is physically the same for the two cases, the noise figure changes in respect to the reference temperature. In this work, we present formulas for including the preamplifier noise based on noise figure simulations or measurements. Further, we show that, in many cases, excluding the noise added by the preamplifier yields too optimistic SNR gain estimates.

H.2 Theory

The SNR gain when comparing a room temperature coil with a cryogenic coil is often described by

$$\Psi_{\text{coil}} = \sqrt{\frac{T^{(\text{r})} \cdot {Q_{\text{u}}^{(\text{r})}}^{-1} + T^{(\text{r})} \cdot {Q_{\text{s}}^{(\text{r})}}^{-1}}{T^{(\text{c})} \cdot {Q_{\text{u}}^{(\text{c})}}^{-1} + T^{(\text{r})} \cdot {Q_{\text{s}}^{(\text{c})}}^{-1}}}, \tag{H.1}$$

where superscripted (r) and (c) refers to the room temperature and cryogenic coil, respectively. T is the temperature of the coil, Q_{u} is the unloaded Q-factor, and $Q_{\mathrm{s}}^{-1} = Q_{\mathrm{l}}^{-1} - Q_{\mathrm{u}}^{-1}$ where Q_{l}^{-1} is the loaded Q-factor. In (H.1) it is assumed that the preamplifier only adds a negligible amount of noise. However, if the preamplifier is used for both the room temperature and cryogenic coil, the noise figure (and thus the SNR impairment) increases as the reference temperature drops. This is because the noise figure is a relative measure. The usual reference is the equivalent noise generated by resistor at a temperature of $T_{\mathrm{ref}} = 290$ K (as per the IEEE definition). Hence, when the reference temperature changes the noise figure also changes. The equivalent noise temperature is defined as

$$T_{\mathrm{e}}^{(\mathrm{r})} = T_{\mathrm{ref}} \left(F^{(\mathrm{r})} - 1 \right), \tag{H.2}$$

where $F^{(\mathrm{r})}$ is the noise figure of the preamplifier measured at a given reference temperature T_{ref}. Hence as the reference temperature is decreased by cooling the coil, while the equivalent noise temperature of the preamplifier remains constant, the resulting cryogenic noise figure increases as described by

$$F^{(\mathrm{c})} = \frac{T_{\mathrm{e}}^{(\mathrm{r})}}{T^{(\mathrm{c})}} + 1. \tag{H.3}$$

Extending (H.1) with (H.2) and (H.3) yields

$$\Psi_{\mathrm{coil+preamp}} = \Psi_{\mathrm{coil}} \frac{F^{(\mathrm{r})}}{F^{(\mathrm{c})}} \tag{H.4}$$

$$= \sqrt{\frac{T^{(\mathrm{r})} \cdot {Q_{\mathrm{u}}^{(\mathrm{r})}}^{-1} + T^{(\mathrm{r})} \cdot {Q_{\mathrm{s}}^{(\mathrm{r})}}^{-1}}{T^{(\mathrm{c})} \cdot {Q_{\mathrm{u}}^{(\mathrm{c})}}^{-1} + T^{(\mathrm{r})} \cdot {Q_{\mathrm{s}}^{(\mathrm{c})}}^{-1}}} \cdot \frac{F^{(\mathrm{r})} T^{(\mathrm{c})}}{T_{\mathrm{ref}} \left(F^{(\mathrm{r})} - 1 \right) + T^{(\mathrm{c})}}. \tag{H.5}$$

H.3 Methods

For SNR comparisons, a room temperature and cryogenic eight-rung low-pass quadrature transmit-receive (T/R) birdcage coil was constructed. The birdcage coils are mounted on a fiberglass tube with an inner diameter of 50 mm and a thickness of 1.5 mm. The coils have a length of 100 mm and an inner diameter of 53 mm. The conductor is 2 mm diameter copper wire. A self-built RF front end consisting of a T/R switch, quadrature coupler, and preamplifier was used with a total noise figure of 1 dB (at reference temperature of 290 K) for the receive path. The cryostat is built using a styrofoam box where the cryogenic coil is completely submerged in LN. See

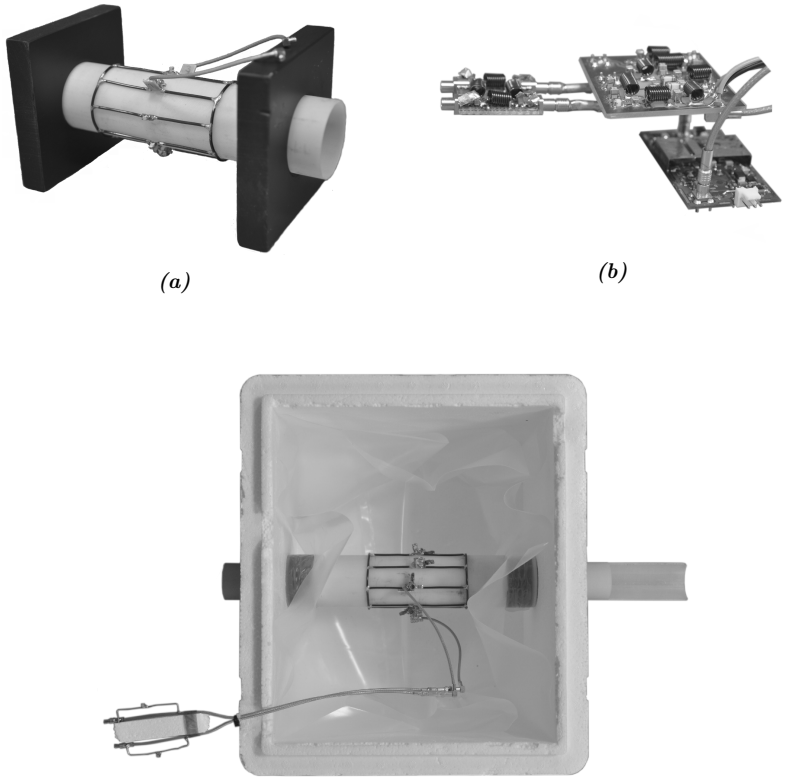

(a) *(b)* *(c)*

Figure H.1: Images of the implemented coils. (a) shows the room temperature birdcage. (b) shows the quadrature hybrid, T/R switch, and preamplifier. (c) shows the cryogenic birdcage and cryostat (excluding the top cover).

Fig. for pictures of the room temperature coil, cryogenic coil, and the RF front end.

The two coils were measured at 32.1 MHz (^{13}C) in a clinical 3T scanner (MR750, GE Healthcare, Waukesha, WI, USA) using a CSI sequence with TR=500 ms and 30 degree flip angle. The sample was a 50 ml tube with 30 mm diameter and length of 120 mm filled with ethylene glycol mixed with 1.7 NaCl g/L (to provide adequate loading).

H.4 Results

Simulated results are seen in Fig. H.2 and H.3. Bench measurements show $Q_{\mathrm{u}}^{(\mathrm{r})} = 362$, $Q_{\mathrm{l}}^{(\mathrm{r})} = 356$, $Q_{\mathrm{u}}^{(\mathrm{c})} = 627$, and $Q_{\mathrm{l}}^{(\mathrm{c})} = 616$. The corresponding SNR gain calculated using

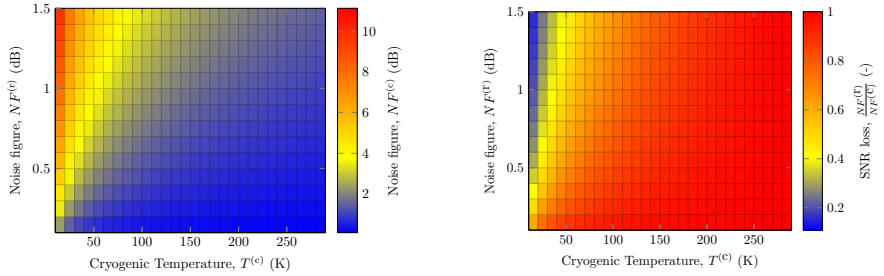

(a) *(b)*

Figure H.2: Calculated dependency on reference temperature and room temperature noise figure of (a) the cryogenic noise figure of the preamplifier and (b) the SNR loss.

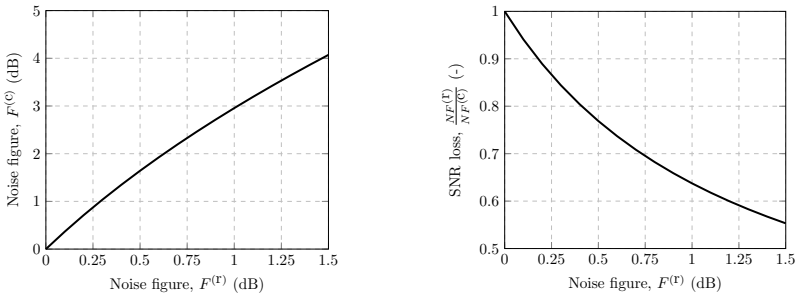

(a) *(b)*

Figure H.3: Calculated cryogenic noise figure (a) and SNR loss (b) as a function of the room temperature noise figure of the preamplifier at 77 K. At 1 dB room temperature noise figure, the cryogenic noise figure is increased to 3 dB resulting in an SNR loss of approximately 35 %.

(H.1) yields 2.5 whereas using (H.5) yields 1.6.

Imaging experiments, seen in Fig. H.4, yielded a room temperature SNR of 55.5 and a cryogenic SNR of 89.7. Hence, the measured SNR gain is 1.62.

H.5 Discussion

The conventional formula for comparing SNR between two coils at different temperatures overestimates the SNR gain, in this case, by approximately 43 % (or 90 % relative to unity) when comparing against the formula presented in this work, which includes the effect of the room temperature preamplifier. The small animal birdcage coils used for this comparison exhibit a poor sample loading of approximately 1.6 %

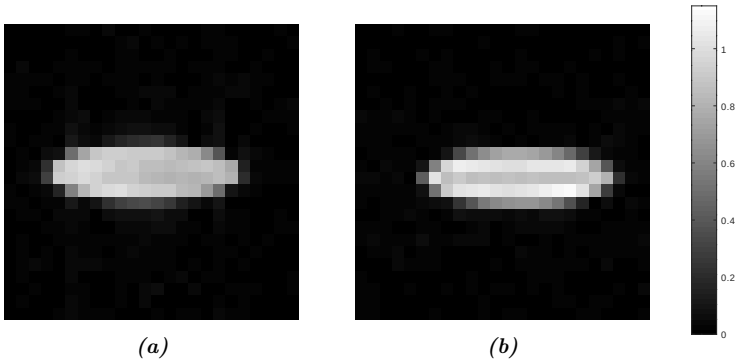

Figure H.4: Scanner measurement showing an image of the cylindrical phantom with (a) the room temperature birdcage and (b) the cryogenic birdcage.

for the room temperature coil and 1.8 % for the cryogenic coil. However, higher sample loading does not mitigate the relative SNR loss caused by the preamplifier.

H.6 Conclusion

When designing cryogenic coils it is vital to include the SNR impairment caused by the preamplifier. Further, the preamplifier should be cooled together with the coil to achieve SNR gains upwards of 40 % better as compared to using a room temperature preamplifier.

References

[1] J. D. Sanchez-heredia, E. Søvsø, S. Hansen, C. Laustsen, V. Zhurbenko, and J. H. Ardenkjær-larsen, "Low-Noise Active Decoupling Circuit and its Application to 13C Cryogenic RF Coils at 3 T," *Tomography*, vol. 3, no. 1, pp. 60–66, 2017.

[2] M. C. Cheng, B. P. Yan, K. H. Lee, Q. Y. Ma, and E. S. Yang, "A high temperature superconductor tape RF receiver coil for a low field magnetic resonance imaging system," *Superconductor Science and Technology*, vol. 18, no. 8, p. 1100, 2005.

[3] J.-C. Ginefri, M. Poirier-Quinot, O. Girard, and L. Darrasse, "Technical aspects: Development, manufacture and installation of a cryo-cooled HTS coil system for high-resolution in-vivo imaging of the mouse at 1.5T," *Methods*, vol. 43, no. 1, pp. 54–67, 2007.

[4] I.-T. Lin, H.-C. Yang, and J.-H. Chen, "A Temperature-Stable Cryo-System for High-Temperature Superconducting MR In-Vivo Imaging," in *PloS one*, 2013.

[5] B. Hu, G. Varma, C. Randell, S. F. Keevil, T. Schaeffter, and P. Glover, "A novel receive-only liquid nitrogen (LN_2)-cooled rf coil for high-resolution in vivo imaging on a 3-tesla whole-body scanner," *IEEE Transactions on Instrumentation and Measurement*, vol. 61, no. 1, pp. 129–139, Jan 2012.

This work describes the optimality principles of preamplifiers for single and array coils, operating at any temperature, for MRI. It is shown, both in theory and practice, that optimal preamplifiers can be implemented resulting in increased SNR. The optimal preamplifiers are utilized in a cryogenic birdcage coil and a 32 channel brain coil showing an SNR increase by up to 20 % and 42 %, respectively. Further, more than 45 dB of preamplifier decoupling is achieved enabling the use of non-overlapping elements in arrays, which potentially lowers the scanning time and thus cost.

DTU Electrical Engineering
Department of Electrical Engineering
Electromagnetic Systems
Technical University of Denmark

Ørsteds Plads
Building 348
DK-2800 Kgs. Lyngby
Denmark
Tel: (+45) 45 25 38 00

www.elektro.dtu.dk